Titre: Title:	Experimental and Numerical Analysis of Impact Damage Progression in Sandwich Structures Designated for Stay Vane Extensions in Hydraulic Turbines
Auteur: Author:	Ghodratollah Morada
Date:	2017
Type:	Mémoire ou thèse / Dissertation or Thesis
Référence: Citation:	Morada, G. (2017). Experimental and Numerical Analysis of Impact Damage Progression in Sandwich Structures Designated for Stay Vane Extensions in Hydraulic Turbines [Thèse de doctorat, École Polytechnique de Montréal]. PolyPublie. https://publications.polymtl.ca/2913/

UNIVERSITÉ DE MONTRÉAL

EXPERIMENTAL AND NUMERICAL ANALYSIS OF IMPACT DAMAGE PROGRESSION IN SANDWICH STRUCTURES DESIGNATED FOR STAY VANE EXTENSIONS IN HYDRAULIC TURBINES

GHODRATOLLAH MORADA

DÉPARTEMENT DE GÉNIE MÉCANIQUE

ÉCOLE POLYTECHNIQUE DE MONTRÉAL

THÈSE PRÉSENTÉE EN VUE DE L'OBTENTION

DU DIPLÔME DE PHILOSOPHIAE DOCTOR

(GÉNIE MÉCANIQUE)

DÉCEMBRE 2017

UNIVERSITÉ DE MONTRÉAL

ÉCOLE POLYTECHNIQUE DE MONTRÉAL

Cette thèse intitulée :

EXPERIMENTAL AND NUMERICAL ANALYSIS OF IMPACT DAMAGE PROGRESSION IN SANDWICH STRUCTURES DESIGNATED FOR STAY VANE EXTENSIONS IN HYDRAULIC TURBINES

présentée par : MORADA Ghodratollah

en vue de l'obtention du diplôme de : Philosophiae Doctor

a été dûment acceptée par le jury d'examen constitué de :

M. SHIRAZI-ADL Aboulfazl, Ph. D., président

M. BOUKHILI Rachid, Doctorat, membre et directeur de recherche

M. VADEAN Aurelian, Doctorat, membre et codirecteur de recherche

M. GOSSELIN Frédérick, Doctorat, membre

M. AKBARZADEH SHAFAROUDI Abdolhamid, Ph. D., membre externe

DEDICATION

To my whole family

ACKNOWLEDGEMENTS

I would like to first thank Pr. Aurelian Vadean and Pr. Rachid Boukhili for their guidance and support during this research project. Your insightful criticism, suggestions and encouragement guided me to complete a rigorous work, while gaining scientific and practical knowledge.

I gratefully acknowledge the contributions of my coworkers on this project, Rim Ouadday, Aymen Marouene and Abderrahmen Kaabi at École Polytechnique de Montreal. The technical advice and support of Josée Laviolette and Isabelle Nowlan are also gratefully acknowledged.

I would like to express my thanks for the financial support by the Consortium de Recherche en Fabrication et Réparation des Roues d'Eau (CREFARRE) and the Natural Sciences and Engineering Research Council of Canada (NSERC). I am also very grateful for Alstom Power and the Hydro Quebec Research Institute (IREQ) for their support. I would also like to thank Michel Sabourin for his technical support.

Finally, I would like to express my gratitude to my family and my friends for being supportive and encouraging throughout the good and bad times for the past years.

RÉSUMÉ

Après des décennies de fonctionnement, une réhabilitation majeure des turbines hydrauliques existantes est nécessaire pour maximiser leur efficacité et leur rendement. Pour atteindre cet objectif, la meilleure solution est de modifier les profils hydrauliques d'avant-directrice en ajoutant une extension en matériaux composites. Malgré leur utilisation croissante, les matériaux composites sont sensibles aux dommages causés par les objets extérieurs. La détection des dommages internes, la prédiction de la propagation de dommages et l'amélioration de la résistance aux dommages restent la principale préoccupation dans le domaine des matériaux composites.

L'objectif principal de cette thèse était d'étudier, à l'aide d'outils expérimentaux et numériques, la résistance aux dommages des panneaux sandwich avec une âme hybride soumise aux impacts à faible vitesse. Le comportement de structures sandwiches soumises aux impacts à faible vitesse a été évalué en termes de force de contact, d'absorption d'énergie, de propagation des dommages et de modes de rupture.

En premier lieu, la réponse au choc de la peau du sandwich fabriquée avec un stratifié non-tissé (NCF) a été étudiée à l'aide d'une tour de chute instrumentée. Un modèle 3D de viscoplastique-dommage a été développé pour prédire la propagation de dommages dans un stratifié NCF. Le modèle numérique a été implémenté dans le logiciel de calcul d'éléments finis LS-DYNA/explicit. Le comportement non-linéaire en cisaillement du modèle proposé a été défini en considérant la dépendance au taux de déformation et la charge d'inversion symétrique. L'efficacité et la précision du modèle ont été vérifiées en comparant les résultats numériques avec ceux obtenus à partir des essais de cisaillement et des essais d'impact à faible vitesse. De plus, les effets de vitesse de déformation sur la résistance aux dommages des stratifiés NCF a été étudié.

En second lieu, des analyses expérimentales et numériques pour structures sandwiches avec une âme en ATH/époxy soumises aux impacts à haute énergie et à faible vitesse ont été réalisées. La raison de cette recherche est que pour une nouvelle solution de réhabilitation de la turbine est fortement requis d'utiliser des matériaux qui peuvent absorber les charges d'impact à haute énergie et préserver un niveau d'intégrité structurale élevé.

Le modèle numérique comprend un modèle viscoplastique pour décrire le comportement de l'âme en ATH/époxy. La capacité du modèle proposé à prédire l'initiation et propagation des dommages a été démontrée en comparant les résultats numériques avec les données expérimentales. En outre, la contribution de chaque constituant d'une structure sandwich dans l'absorption d'énergie a été quantifiée.

En dernier lieu, la réponse des poutres sandwiches avec une âme en ATH/époxy soumis à des sollicitations quasi statiques et dynamiques de flexion trois points a été étudiée. L'objectif était d'explorer les mécanismes de défaillance des poutres sandwiches ainsi que l'interaction entre les modes de rupture. L'effet du taux de déformation sur le comportement de poutres sandwiches a été démontré en réalisant des essais de flexion trois points en sollicitations quasi statiques et dynamiques.

La contribution principale de cette thèse est l'évaluation de la performance de la structure sandwich avec une âme en ATH/époxy en termes de résistance aux dommages induits par impact, d'absorption d'énergie et de conservation de son intégrité structurale. Un modèle numérique robuste a également été développé pour prédire l'amorçage et la propagation de dommages dans la structure sandwich en composite.

ABSTRACT

After decades of operation, a major rehabilitation of existing hydraulic turbines is required to maximize their efficiency and output. To achieve this aim, the best solution is to modify the hydraulic profiles of stay vanes by adding composite extension structures to the original stay vanes. Nowadays, composite materials have found their way into different industrial fields due to their advantage over metals or metal alloys. Despite their increasing use, composite materials are sensitive to impact damage induced by foreign objects. Detecting internal damage, predicting damage progression and improving damage resistance is still the major concern of composite materials.

The main objective of this thesis was to investigate low-velocity impact damage resistance of sandwich panels with a hybrid core using experimental and numerical tools. The impact behavior of sandwich panels was evaluated in terms of contact force, energy absorption, damage propagation and failure modes.

First, the impact response of sandwich face sheets made with non-crimp fabrics (NCF) laminate was studied using an instrumented drop weight impact machine. A 3D viscoplastic-damage model was developed to predict damage growth in NCF laminate. The numerical model was implemented in LS-DYNA/explicit. The nonlinear shear-strain behaviour of numerical model was defined by considering the strain rate dependence and symmetric reversal load. Efficiency and accuracy of the model were verified by comparing the numerical results with the experimental results obtained from shear tests and low-velocity impact tests. In addition, the effects of strain rate on impact resistance of NCF laminate was studied.

Second, experimental and numerical analysis of ATH/epoxy core sandwich panels subjected to low-velocity impact loads were performed. The reason for this investigation is that, for a new solution of turbine rehabilitation is strongly required to choose the composition materials which can absorb higher impact loads and preserve a high margin of structural integrity. The numerical model includes a viscoplastic model for describing the ATH/epoxy core behavior. The capability of the proposed model in the prediction of damage growth was demonstrated by comparing the numerical results with experimental data. Additionally, the contribution of each sandwich component in energy absorption was evaluated.

Finally, quasi-static and low-velocity impact response of sandwich beams with an ATH/epoxy core in three-point bending were investigated. The goal was to explore failure mechanisms of sandwich beams as well as the interaction between the failure modes. The effects of strain rate on the behavior of sandwich beams were shown by performing three-point bending under quasi-static and impact loading.

The main contribution of this thesis is to evaluate the performance of sandwich structure with an ATH/epoxy core in terms of impact damage resistance, energy absorption and retain its structural integrity. A robust numerical model was also developed to predict damage initiation and propagation in composite sandwich structure.

TABLE OF CONTENTS

LIST OF TABLES

.

LIST OF FIGURES

CHAPTER 1 INTRODUCTION

1.1 Background and description

Composite materials have been shown to have very high strengths and stiffness to weight ratios which permit them to be in various industrial applications where the high structural performances are required. For this reason, composite structures have found their ways in the new field such as transports, sports goods, civil engineering and energy productions. In addition, composite materials may be specifically designed to be attached to the existing conventional structures to improve their mechanical properties and structure performances. However, composite structures are sensitive to the impacts of foreign objects. In-service composite structures may experience impact damage during manufacturing or maintenance because of the collision with dropped tools and environmental debris around the structures and consequently, can lead to complex behavior in the structures. The composite structures have various damage modes such as matrix failure, fiber breakage or interface delamination. Certain failure modes are internal damage with little or no external visibility. Furthermore, these damage modes can propagate quickly or gradually due to fatigue loading during service operation and can considerably reduce structural performance. Performing visual inspection of damage is not a clear indicator of internal damage in composite structures and destructive methods are not practical options. Therefore, in order to increase the structural efficiency of composite materials and improve their damage resistance, it is necessary to gain better knowledge about the impact response of composite structures.

1.2 Problem statement and research motivation

Hydraulic power has been a great source of green energy for human activities during the past decades and helps to provide the massive energy required for the industrial development. Hydroelectricity is a renewable source of energy which is an important solution for avoiding the environmental change. Hydroelectricity is generally derived from running water. Indeed, underwater turbines are turned by the pressure of running water.

Today the hydroelectric power plants with more than 40 years old are needed to be rehabilitated in order to give them a new life. This rehabilitation is also required to improve the turbine

performance and to diminish their environmental impacts, in conjunction with solving the problems like cavitation wearing. Most of the turbine hydraulic parts are fabricated from stainless steels or cast irons. The turbine performances are gradually reduced due to changing of hydraulic original profiles which are generally caused by the erosion of turbine steel surface after years of operation, and also on-site reparation. The stay vanes consist of the number of blades that are arranged around turbine in order to steer the water into the turbine shaft. It should be mentioned that the stay vanes are fixed. The stay vanes can have considerable effects on the performance of a hydroelectric plant. Therefore, improving the stay vane profile is an important concern of turbine rehabilitation.

Recently, Alstom Company proposed to modify the profile of stay vane by adding an extension structure to the leading edge of stay vane, as shown in Figure 1.1. It has been demonstrated in the laboratory that this modification helps to gain about 0.7% efficiency with respect to the existing turbine (Bornard et al., 2014). Generally, the stay vane extensions are made of stainless steel and welded on the existing stay vanes. However, Alstom proposed an innovative structure made with composite materials. The proposed structure is a composite sandwich composed of a fiberglass shell filled with the epoxy casting. The fiberglass shell of the extension will be attached to the surface of original stay vanes by the epoxy casting. It is worth noting that there is no need for welding and no risk of stay vane profile deformation due to heat generation by using a composite extension. Furthermore it enhances the impact resistance properties of stay vanes (Bornard et al., 2014).

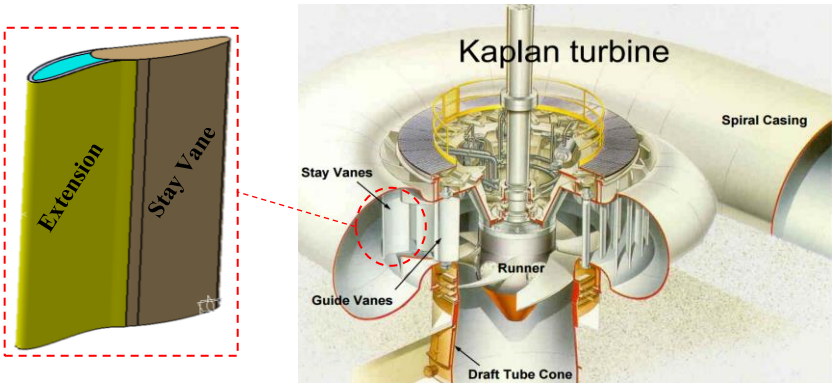

Figure 1.1: Extension structure attached to the stay vane

The preliminary investigation showed that the hydraulic pressure on the extension structure is almost negligible if the stay vane's profile was optimized. Nevertheless, impacts induced by the

debris flow in water can cause serious damage to the extension structure. The biggest debris flow that has been recorded is a rock having dimensions of approximately 15 cm, and the maximum velocity of flow is approximately 6 m/s. Impact-induced damage can significantly degrade the mechanical properties of composite structures. Therefore, it is required to investigate the impact damage resistance of extension structure.

In the earliest stage of this project, several sandwich constructions with different core materials, such as a foam/epoxy core, an ATH/epoxy core and a double core made of ATH/epoxy and extruded polystyrene (XPS) foam, were analyzed under low-velocity impact tests (Ouadday, 2013). After preliminary study, an innovative sandwich construction made of glass/epoxy laminated face sheets and the ATH/epoxy core is selected to fabricate stay vane extension structure.

1.3 General objective

The general objective of this thesis is to develop a novel sandwich composite structure and evaluate its impact resistance, which is used for the design of an extension structure. The extension structure modifies the stay vane's profile and consequently increases the performance of an original hydraulic turbine.

1.4 Specific objectives

The specific objectives of this thesis are:

(1) Modeling damage progression for low-velocity impact simulation

The first objective of this thesis aimed at developing and validating a progressive damage model to assess the damage resistance of the extension shell made of non-crimp fabric (NCF) laminated composite, based on the following main steps:

- The development of a progressive damage model based on the continuum damage mechanics approach;
- The improvement of accuracy of the existing model by incorporating the strain rate dependence and the reversal load in the model;

- The validation of the proposed model by comparing numerical results with the experimental results which were obtained by performing shear tests and low-velocity impact tests on the laminated composites;
- The investigation of damage propagation sequence as the impact energy increases;
- The demonstration of the model's ability to predict accurately failure modes of laminated composites by comparing the numerical results with microscopy observations;
- The investigation of the effect of strain rate on the static and dynamic responses of the laminated composite.

(2) Investigating the impact resistance of sandwich panels with an ATH/epoxy core

The second objective of this thesis is to demonstrate the impact response of the sandwich composite structures made of NCF glass/epoxy laminated face sheet and ATH/epoxy core, based on the following steps:

- The characterization of ATH/epoxy core by performing various mechanical tests;
- The investigation of the impact behavior of composite sandwich structures by conducting low-velocity impact tests;
- The assessment of damage zone using a destructive observation approach;
- The development and validation of a material model for the sandwich core;
- The finite element simulation of sandwich structures to obtain more insight information on the behavior of sandwich structures;
- The comparison of the numerical and experimental results in order to demonstrate the efficiency and accuracy of the model.

(3) Investigating the failure mechanism of sandwich composite beams with an ATH/epoxy core

The third objective of this thesis was to determine the failure modes and the failure sequence of the sandwich composite structures with an ATH/epoxy core, based on the following steps:

- The investigation of the failure mechanism of sandwich structures by performing three-point bending tests and using Digital Image Correlation technique;
- The analysis of the interaction between various failure modes that may occur during three-point bending tests;
- The extension of the progressive damage model to capture various failure modes;
- The assessment of functionality of the progressive damage model to predict the failure mechanisms in the sandwich beams;
- The investigation of the influence of strain rate on the mechanical behavior of sandwich structures under three-point bending tests.

1.5 Proposal outline

The main body of this thesis is separated into three sections. Each section is dedicated to a research article prepared during this project in order to attain the above-mentioned objectives. The following outlines describe each article and its context with regard to the specific objectives.

(1) Article 1: Viscoplastic-damage model for low-velocity impact simulation of non-crimp fabric-reinforced composites

This article presents a viscoplastic-damage model for modeling a non-crimp fabric-reinforced laminate under low-velocity impacts. The model includes a mixed-mode matrix damage initiation and propagation law in combination with a nonlinear shear-strain behavior. An explicit UMAT code is developed and implemented in Ls-dyna/explicit. Furthermore, low-velocity impact tests and shear tests were conducted on the NCF glass/epoxy laminates. The numerical results were then compared to the acquired experimental data. The main contributions of this paper are:

- A viscoplastic-damage model that can accurately predict the mechanical behavior of composite materials under low-velocity impact;
- An improvement in the definition of reversal load of shear- strain behavior, which can be easily implemented;
- The damage resistance of the NCF glass/epoxy laminated composites is demonstrated;

- The effects of strain rate on the damage extension in the NCF glass/epoxy laminates are well established.

This article was submitted to the "International Journal of Solids and Structures", in March 2017. This journal treats all aspects of the science, including fracture, optimum design methods, model analysis, structural topology and numerical techniques.

(2) Article 2: Low-velocity impact resistance of ATH/epoxy core sandwich composite panels: Experimental and numerical analyses

This article is concerned with the performance of sandwich panels with an ATH/epoxy core in terms of mechanical response and damage resistance. Low-velocity impact tests on the novel sandwich panels were conducted at various impact energies. The damage initiation and propagation were monitored as the impact energy increases. In addition, a progressive damage model was developed to predict the damage progression in the sandwich panels. The numerical prediction results were compared to those of the experimental tests for a wide range of impact energies. The main contributions of this paper are:

- It is the first time that the low-velocity impact response of sandwich panels with an ATH/epoxy core are investigated;
- A new material model that simulates the nonlinear behaviour of an ATH/epoxy core;
- A post-impact analysis of specimens which provides more insight information about the failure modes in the face sheet and core;
- The performance of ATH/epoxy core sandwich panels subjected to low-velocity impacts is evaluated in terms of damage resistance;
- The ability of ATH/epoxy core material to absorb the impact energy and reduce the damaged zone is shown.

This article was published in "Journal of Composites Part B", volume 114, pages 418-431 in February 2017. This journal publishes original research on all areas of composites and nano-engineered materials, with emphasis being placed on evaluation and modelling of engineering details and concepts.

(3) Article 3: Failure mechanisms of sandwich beam with an ATH/epoxy core under static and dynamic three-point bending

This article presents an investigation on the failure mechanisms of the sandwich beams with an ATH/epoxy core under three-point bending tests. The three-point bending tests were executed under quasi-static and dynamic loading conditions. Digital image correlation (DIC) technique were used to show the role of various failure modes in the collapse of the sandwich beam. In addition, the 3D progressive damage model was extended to predict the different failure modes of sandwich beams. The performance of numerical model at predicting the failure initiation and propagation was evaluated by comparing the numerical results with the experimental results. The main contributions of this paper are:

- It is the first time that the failure mechanisms of sandwich beams with an ATH/epoxy core are presented in the literature;
- An efficient FEM model for predicting the various failure modes and the sequence of failure events inside the sandwich structures;
- The difference between quasi-static and dynamic three-point bending and the effects of strain rate on the damage progression are well established;
- The performance of sandwich beam under large global deformation was evaluated, as well as its limitation on bearing low-velocity impact loading.

This article was published in "Journal of Composite Structures", volume 176, pages 281-293 in May 2017. This journal publishes articles that contribute to knowledge in the application of composite materials in engineering structures.

CHAPTER 2 LITERATURE REVIEW

2.1 Low-velocity impact

Low-velocity impact occurs when a foreign object impacts the structure, for instance, when a tool drops during manufacturing or maintenance, or when debris on the road impacts the structure. In general, low-velocity impacts are considered to occur at velocity less than 10 m/s, nevertheless Abrate (1991) said that the low-velocity impact happens for impactor velocity less than 100 m/s.

The composite structures are more vulnerable to impact damage when compared to metallic structures. Damage in metallic structures appears at the impacted face, therefore it could be easily detected. In contrary, damage in composite structures generally initiates on the non-impacted face or as internal damage, and it is difficult to diagnostic. Moreover, the ductile nature of metallic structures helps to absorb a large amounts of energy through plastic deformation during an impact event. However, most composite structures have a brittle nature and can only dissipate energy through elastic deformation and damage propagation. The damage resistance of composite structures (the amount of impact-induced damage) is therefore an important issue in the application and development of composite materials. Furthermore, the impact-induced damage is especially dangerous because it significantly decreases the mechanical properties of the structures such as the compressive strength.

2.2 Failure modes of laminated composites

From the design point of view, damage initiation threshold as well as perforation threshold are essential in composite materials. The evolution of the size of impact-induced damage with the initial impact energy must be then studied. The global response of a composite laminate subjected to low-velocity impact, in terms of contact force and corresponding deflection, has been investigated by many researchers. Certain researchers prefer to perform a filtering process to remove the vibration modes of impactor from impact results. However, Davies and Olsson (2004) believe this filtering can hide the important information such as sudden contact load drops corresponding to delamination initiation. The appearance of damage is generally accompanied by oscillations in the force-time curves of impact results. During an impact event, the different failure

modes that can occur in the laminated composites are: the matrix failure, delamination and fiber breakage. Furthermore, numerous investigations allowed the different authors to describe the failure mechanism during a low-velocity impact (Richardson et al., 1996b).

Damage is generally distributed around the impact point in the form of a damaged cone, as shown in Figure 2.1. The damage zone is more extended around the non-impacted face and more restricted around the impact point. Damage in laminated composites is categorized into two parts (Hodgkinson, 2000):

- The intra-laminar damage: the damage appearing inside the ply as matrix cracking, fiber/matrix debonding or fiber failure;
- The inter-laminar damage: the damages appearing at the interface of two successive plies.

In the following sections, different damage modes are presented in order of appearance in the impacted specimens.

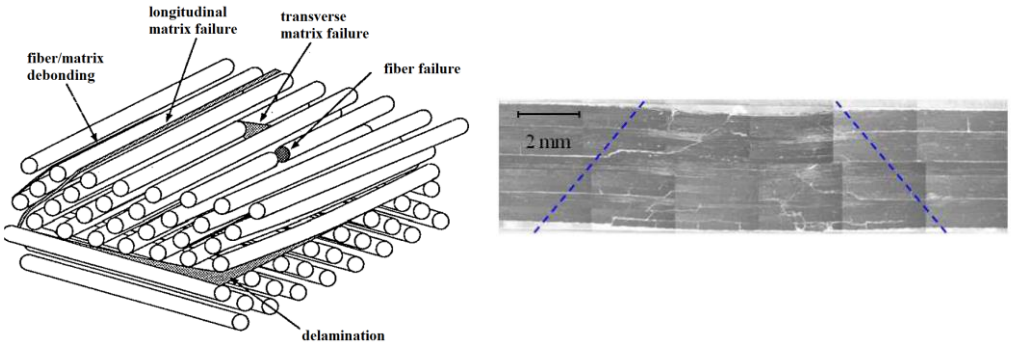

Figure 2.1: Observed damage in unidirectional laminated composite (Berthelot, 1999)

2.2.1 Matrix failure

Matrix failure is the first damage modes induced by a low-velocity impact. This failure mode appears in the form of matrix cracks and fiber/matrix debonding (Richardson et al., 1996b). Matrix damage is oriented towards the fiber directions. Two categories of matrix cracks are distinguished by their nature:

a) Shear cracks: they appear in the upper and middle layers due to high transverse shear stress and are inclined at approximately 45°;

b) Bending cracks: they are formed by high tensile bending stress and generally appear in the bottom layers.

Formation of each type of matrix cracks depends on the geometrical dimensions of the impacted specimens. The bending cracks are more pronounced in the long thin specimens due to large deflection, while the shear cracks are more present among the short thick specimens, which are stiffer and suffer from transverse shear stress under the impactor.

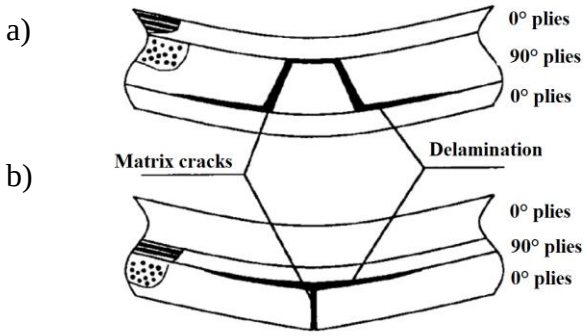

Figure 2.2: Matrix damage scenario: a) shear cracks and b) bending cracks (Berthelot, 1999)

2.2.2 Interface delamination

In the failure mechanism of composite laminates, delamination generally appears after matrix cracks. Indeed, once matrix cracks reach to the interface of plies with different fiber orientation, they are stopped by the change in fiber orientation and propagate among the plies as delamination.

Liu (1988) revealed that delamination is caused by the flexural stiffness mismatch among two adjacent plies. Composite laminates under impact loading tend to bend concave along the fiber direction, while the bend is convex in the transverse direction which induces high shear stress in the ply interface (Richardson et al., 1996a). The larger the difference of fiber orientation of two plies is, the greater the delamination zone will be induced in impacted specimens.

Maio et al. (2013) also explained that delamination is initiated by the high normal out-of-plane stress, which is caused by the presence of matrix crack and the high inter-laminate shear stress at ply interface (accompanied with very low through-thickness strength). The delamination initiated by the shear cracks is unstable, while the delamination initiated by the vertical cracks propagates in a stable manner and is proportional to the applied force (Richardson et al., 1996a). In addition,

delamination in the impacted specimens occurs after a threshold energy, which depends on the specimen geometry as well as the inter-laminar fracture energy. It is commonly approved that the interface delamination extremely depends on the Mode II fracture energy.

In general, delamination appears in the form of peanut shape which its axis is oriented in the fiber direction of the ply under the interface, as shown in Figure 2.3. Even if, delamination is not a catastrophic failure mode, it is considered as a most important mode of failure because it reduces the compressive resistance of composite laminates. That's why a good prediction of delamination zone is very important for accurate simulations.

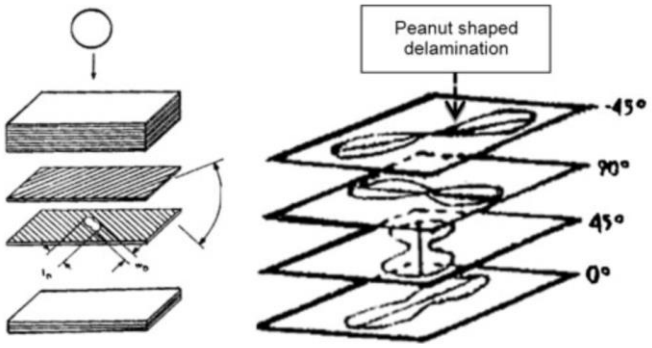

Figure 2.3: Impact-induced delamination in unidirectional laminated composite (Maio et al., 2013)

2.2.3 Fiber failure

Fiber breakage appears later than matrix cracks and delamination in the failure mechanism of laminated composites. They are localized close to the impact axis and they generally occur at high impact energies, under the impact point and on the non-impacted face. Under the impactor, the fibers fail due to high localized stress (shear stress near the contact area) and indentation effects (Richardson et al., 1996a). On the non-impacted face, the high tensile stress due to bending deformation is responsible for the fiber failure. The fiber failure is a catastrophic failure mode of laminated composites and leads to impactor penetration.

2.3 Behavior of sandwich structures under impact loading

Sandwich structures have been frequently used in many engineering fields because of high bending resistance and good strength to weight ratio. A composite sandwich structure is composed of two thin face sheets bonded to a relatively thick core. The face sheets of sandwich withstand almost all

the in-plane loads. While, the core transmits shear stress between two face sheets and also supplies shear rigidity to the structure.

The core material plays the main role in the mechanical properties and damage behavior of sandwich structures. The proper choice of the core material is therefore very essential. Various types of material have been widely used as core material in sandwich structures, such as: a) foam core, b) honeycomb core, c) balsa wood and d) corrugated sheets. An aluminum honeycomb core provides the best stiffness to weight ratio, but it most likely suffers from corrosion damage. Various cellular foams use in the industrial application because of their water resistance, relatively low cost, and feasibility to apply traditional manufacturing methods like hand layup. The foam core can supply a better bonding with face sheets by increasing the support surface. Balsa cores are commonly used in the marine industry. Wang et al. (2016) compared the low-velocity impact response of sandwich structures with five different cores: low-density balsa wood, high-density balsa wood, cork, polypropylene honeycomb and polystyrene foam. They concluded that polystyrene foam is the optimum choice for core material to increase the energy absorption and penetration resistance. Jin et al. (2013) designed a new integrated woven corrugated sandwich structure (Figure 2.4) in order to improve face/core debonding resistance. Their experimental results showed that the anisotropy of the sandwich core results in different failure modes under three-point bending tests. The failure mode in the warp direction is the core shear failure, whereas that in the weft direction under flexural loading is indentation failure.

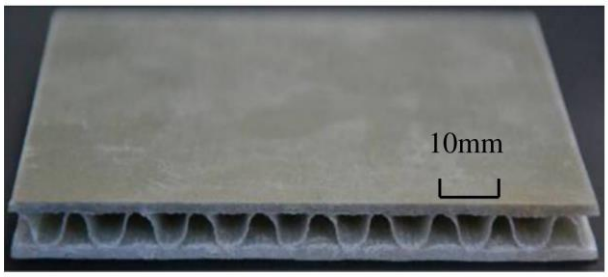

Figure 2.4: Sandwich composite panel with woven face sheets and wave core (Jin et al., 2013)

Yan et al. (2014) compared the three-point bending response of a sandwich beam with aluminum foam-filled corrugated core and that of sandwich with the empty corrugated core. The filling of corrugated core resulted in significantly increasing the bending stiffness and load bearing capacity of sandwich structures. Furthermore, Abdi et al. (2014) studied the effect of the polyester pin

reinforcement in the foam core. They reported a significant improvement in the flexural properties of sandwich structure with the polyester pin reinforcement.

The main concern with conventional core sandwiches is that they cannot resist a high impact energy without suffering from a large damage area. A novel core material with higher density is needed to resist a high impact energy. Torre and Kenny (2000b) developed a new sandwich composite panel to increase the damage resistance. The sandwich panel was made of glass/polyester skins and a core composed of an internally corrugated laminate filled with a phenolic foam, as shown in Figure 2.5. The impact response of this sandwich was compared with the impact response of a phenolic foam-core sandwich panel. The corrugated sandwich panel demonstrated a better performance in terms of the energy dissipation and damage resistance compared to the convention sandwich panel.

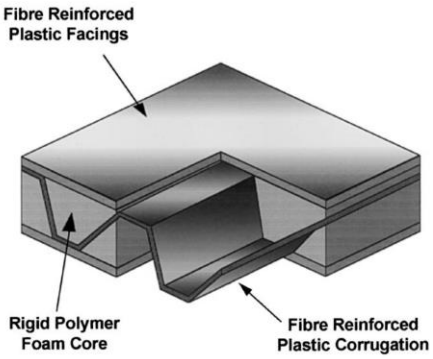

Figure 2.5: Sandwich composite panel with a corrugated laminated core filled by a phenolic foam (Torre et al., 2000b)

Ji et al. (2013) also developed a novel sandwich panel with a hybrid core composed of metallic millitubes and polymer matrix. They compared the impact behavior of three sandwich panels with different core materials, as shown in Figure 2.6. The compressive strength, flexural strength and low-velocity impact response of sandwich panel with horizontal millitubes were significantly improved. The results also showed that the energy absorption capacity of the sandwich was enhanced due to the plastic deformation of the aluminum millitubes. Furthermore, the first few rows of millitubes act as a cushioning layer to protect the face/core interface and no interface debonding was found in the sandwich with horizontal millitubes.

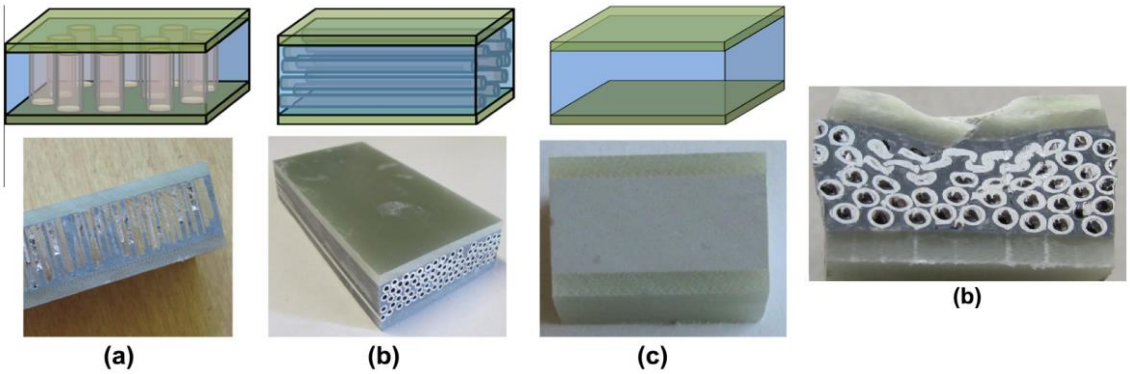

Figure 2.6: Sandwich panels with different cores: a) hybrid core with vertical millitubes, b) hybrid core with horizontal millitubes and c) conventional syntactic foam (Ji et al., 2013)

2.3.1 Failure modes of sandwich structure

The investigation on the behavior of sandwich structures under low-velocity impact events requires distinguishing different failure modes of sandwich structures and their effects on the sandwich stiffness. Once damage occurs in a sandwich structure, the stiffness and load bearing capacity of sandwich decrease considerably until the final failure. Four main modes of failure in composite sandwich structures have been classified as (Steeves et al., 2004): 1) the core shear failure, 2) interface debonding between the face sheet and the core, 3) wrinkling of the face sheet, 4) indentation due to core crushing, as displayed in Figure 2.7.

The occurrence of these failure modes depends on the material properties of sandwich components, the interface between the face sheet and core.

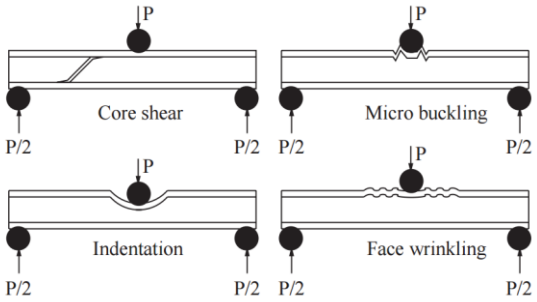

Figure 2.7:Sandwich failure modes (Steeves et al., 2004)

When the impact energy increases, damage initiates and propagates in the sandwich components. The initial impact energy is dissipated by damage mechanisms in the face sheet and core. The mode

of energy dissipation depends on the geometry, materials and boundary conditions of the sandwich panel. Cantwell et al. (1994) revealed that the shear failure of face sheet is the main source of energy dissipation in sandwich panels used in marine structures. Mines et al. (1998b) investigated the impact response of two sandwich panels with the Coremat core and honeycomb core. They concluded that the core crushing is the dominant mode of energy absorption.

One of the main disadvantages of the conventional core sandwich is the dissimilarity of the face sheets and core material. With respect to this concern, Vaidya et al. (2008) studied the low-velocity impact response of sandwich panels with a hollow core and a polyurethane foam filled core. The failure mode of un-foamed sandwich was the buckling of the core plies and rupture of top face sheet, while that of the foamed sandwich was foam crushing, as observed in Figure 2.8.

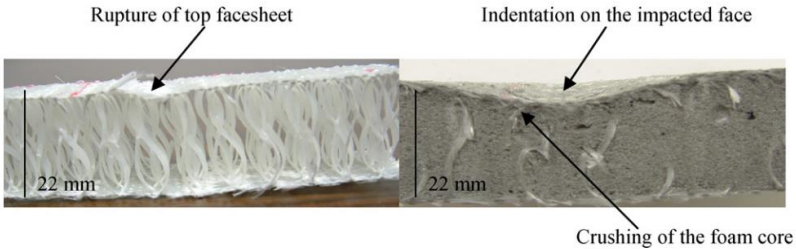

Figure 2.8: Failure modes of un-foamed and foamed core sandwich panels (Vaidya et al., 2008)

The perforation resistance of sandwich panels with different core materials (made with a cross-linked PVC, a linear PVC and PET), placed between glass fiber-reinforced skins, was investigated by Hassan and Cantwell (2012). The experimental results revealed that the perforation resistance was strongly dependent on the foam shear strength and the Mode II of foam material fracture. They pointed out that simple shear tests can be used to verify the perforation behaviour of foam materials. Zhou et al. (2013) proposed a sandwich panel with a hybrid core composed of three foam with different densities bonded together (linear PVC, cross-linked PVC and PEI foams) to improve the perforation resistance.

Othman and Barton (2008) studied the failure mechanisms of honeycomb sandwich panels under quasi-static and impact loading. It was found that the peak force and total energy absorption under impact loading are significantly higher than the quasi-static loading. Schuble et al. (2005) demonstrated that the quasi-static and impact response of sandwich panels made with carbon/epoxy

face sheets and PVC foam core is nearly similar. However, they emphasised that the static deformation and strain levels are more severe, and the damage processes initiated earlier.

Furthermore, three-point bending tests have been used by many researchers to study the failure mechanisms of sandwich beams and trace the failure maps. For instance, Crupi et al. (2012) analyzed the static and dynamic three-point bending responses of aluminum honeycomb sandwiches. They reported that the bending response of sandwich beams is dependent on the support spans. The collapse mode of sandwich beams with short span support is the core shear failure mode (Mode II), while the sandwich beams with long span support collapsed by Mode I.

The effect of face/core bonding on the impact response of glass/polyester PVC foam core sandwich panels by performing flexural impact tests was investigated by Imielinska et al. (2008). They concluded that the type of bonding does not influence the delamination threshold load. Veedu and Carlsson (2005) also studied the effects of the face/core debonding on the buckling and failure behaviour of foam-core sandwich columns. The results showed that the long interface debonding and low core density considerably reduce the buckling force.

Daniel et al. (2012) investigated the impact and post-impact response of sandwich panels made of unidirectional glass/vinylester skins with various core materials (PVC foam and balsa wood). The experimental results revealed that even a minor visible damage can considerably reduce the residual mechanical properties. Damage tolerance of NCF composite sandwich with crosslinked PVC foam core was analysed by Edgren et al. (2008). The compressive after impact tests were carried out on the specimens with visible impact damage (penetrated face sheet) and barely visible impact damage (BVID). The obtained experimental results revealed that the penetrated specimen and BVID damage specimen collapsed at the same compressive force. Furthermore, they used two approaches to predict the compressive strength of damaged specimens: 1) a single equivalent notch and 2) an equivalent open hole. A single equivalent notch represents better the kink-band forming (narrow bands with micro buckled fibers, see Figure 2.9) during compression tests which controls the compressive strength. However, the authors recommend an equivalent open hole with a diameter equal to the damaged area to estimate the compressive failure, as it is difficult to determine a critical notch length.

The effect of oblique impact on the response of composite sandwich plates with a Nomex honeycomb core was also investigated by Ivanez et al. (2015). The maximum contact force, damaged area and energy absorption tend to decrease with increasing the impact angle.

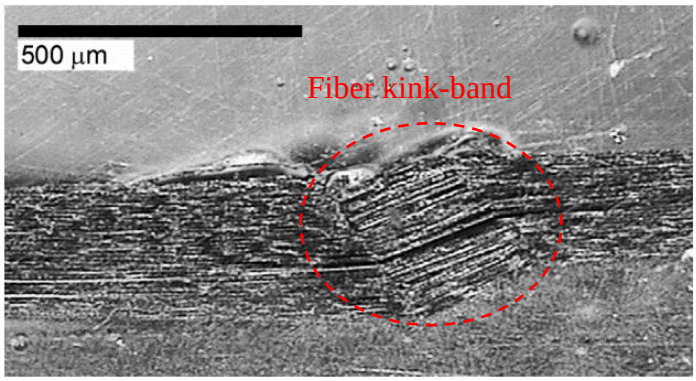

Figure 2.9: Kink-band found in an NCF composite loaded in compression (Edgren et al., 2008)

2.4 Modeling of damage and fracture of laminated composites

In the literature, several analytical solutions for specific impact cases have been proposed to model a complex impact event. These solutions are limited to simple impact cases in which the complicated phenomena such as transverse shear deformation and rotary inertia were not considered. Furthermore, the geometry of impactor was neither considered in modeling, and a single point contact between the impactor and plate was assumed. These models allow to understand the effects of mass and plate geometries on the impact response. Such limitations can be overcome by using numerical models. The most common numerical method for impact simulation is the finite element method. Various finite element software packages have been applied to simulate an impact event such as ABAQUS/explicit, LS-DYNA, etc. The software permit users to implement a new material model in the software via a user-defined subroutine (UMAT). The material modeling is important to simulate the impact damage propagation, energy absorption and stiffness degradation.

Various approaches can be found in the literature to simulate the damage evolution in laminated composites and they can be categorized into four types: 1) failure criteria, 2) fracture mechanics, 3) plasticity and 4) damage mechanics approaches.

The failure criteria based on the material strengths can determine the loading conditions under which failure initiates, however it does not reduce the material stiffness. In this approach, once damage initiates, Young's modulus in the failure direction is set to zero. The failure criteria approach can predict neither the position nor the size of damage zone. That is why the fracture mechanics approach can be more attractive. In the fracture mechanics approach, the strain energy at the crack front (for a known crack length) is first calculated, and then compared with the critical strain energy release rate in order to increase the crack length. The approach has been used to simulate the delamination growth and the prediction of residual compressive strength. However, it is worth noting that the application of fracture mechanics approach requires a prior knowledge of the crack growth path. Plasticity approach is suitable for composite laminates which exhibit ductile response such as Graphite/Peek, Boron/Aluminum and other thermoplastic composites and it can be merged with the failure criteria approach for estimating damage growth. The continuum damage mechanics approach has been used by numerous researchers in the past decades. The approach has been applied successfully to simulate an impact event. Moreover, the continuum damage mechanics (CDM) can be combined with the failure criteria approach for predicting the damage initiation and with the fracture mechanics approach for simulating the damage propagation.

Recently, Bouvet et al. (2012) developed a 3D model based on discrete damage mechanics to simulate the various impact damage modes and interaction between them during low-velocity impact. In this model, the laminate is discretized into volumetric elements joined together by the interface elements, as shown in Figure 2.10. Matrix cracks are inevitably vertical in this model for avoiding the creation of complex mesh in the impact zone. Consequently, the model is limited to thick composites where the ply thickness can be negligible respect to the laminate thickness. Application of this type of damage mechanics is still rare.

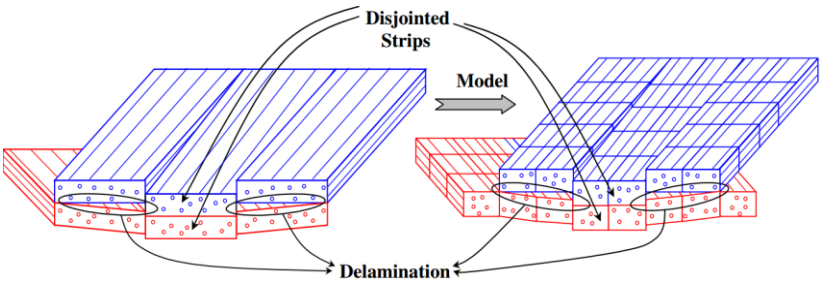

Figure 2.10: Discrete damage mechanics (Bouvet et al., 2012)

2.5 Continuum damage mechanics of composite materials

Continuum damage mechanics was originally proposed by Kachanov and Rabotnov (1958). They proposed the concept of representing damage accumulation during creep of metals by using a scalar damage parameter. The effects of randomly dispersed micro-defects (void) were considered on the macro parameters of structure (mechanical properties). The CDM approach was later used for laminated composites by Talreja (1985).

The definition of internal damage parameters used in a CDM model is very important. The damage parameters must be capable of representing the effects of micro-defect, as well as making the model applicable to engineering problems. Kachanov and Rabotnov (1958) proposed the area density definition of damage parameters. However, it is difficult to measure the effective area directly from the crack distribution after cross-sectioning.

To give details of common damage definition in the composite materials, a volume element at macro-scale is considered, as shown Figure 2.11. In this figure, S is the cross-section area of volume element V_m, before damage occurs. After the formation of micro-cracks and void growth with an area of S_d, the effective area becomes $\bar{S} = S - S_d$.

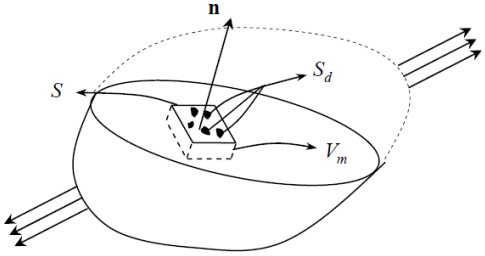

Figure 2.11: A volume element with micro-cracks

The internal damage parameter d can be defined by quantifying the relative micro-cracks area in the cross-section of volume element as follows:

$$d = \frac{S_d}{S} = \frac{S - \bar{S}}{S} \tag{2-1}$$

It is worth noting that the damage parameter value varies between 0 and 1. When the damage parameter d is equal to zero, it indicates the undamaged state of the material, and once d is equal to one, it indicates the final failure state of material.

The appearance of micro-cracks in the cross-section reduces the resisting area and the stress redistributes over the undamaged area. Therefore, the relationship between effective stress in an undamaged material state and damaged state can be written as follows:

$$\bar{\sigma} = \sigma \frac{S}{\bar{S}} = \frac{\sigma}{1-d} \tag{2-2}$$

This is the concept of Kachanov-Rabotnov damage theory, which was proposed for one dimension bar and it formed the foundation for the development of CDM. In general, the development of CDM model includes two parts: failure initiation criteria and failure propagation. These two parts are discussed in the following sections.

Initially, damage models based on CDM were used for 2D problems in which only in-plane stress effects were assumed. Damage models for woven laminated composites have been developed by Iannucci et al. (2001) to simulate matrix cracks and fiber breakage in the warp and weft directions. Iannucci and Ankersen (2006) proposed an energy-based damage model which can be applied to both woven and unidirectional composites. Lately, Pinho et al. (2006) developed a full 3D damage model which includes a set of three-dimensional failure criteria. Donadon et al. (2008) also implemented a 3D progressive failure model in the explicit Ls-dyna software, considering the different inter-laminar damage modes which can occur in laminated composites. The low-velocity impact response of foam-based sandwich composite was also simulated by using a 3D damage model and interfacial cohesive elements (Feng et al., 2013).

2.5.1 Failure initiation criteria

As mentioned previously, laminated composite materials have different failure modes such as matrix crack, fiber breakage and fiber-matrix debonding. Various failure criteria have been used to precisely predict the initiation of failure in composite materials. In the literature, four forms of failure criteria have been developed: 1) limit theories in which the maximum stress and maximum strain was used as criteria, 2) polynomial theories in which a polynomial expression of stress components was used to define a failure envelope (Tsai-Wu failure criterion (1971)), 3) strain energy theories in which material failure is defined by using a nonlinear energy based criterion (Tsai-Hill criterion (1965)), 4) direct mode theories in which the initiation of each failure mode is defined by a discrete equations (Hashin failure criterion (1980)). Hashin failure criterion has been

frequently used because the theory is capable to predict damage onset for each failure modes separately. Hashin failure criteria are described as follows:

Fiber tension failure ($\sigma_{11} \geq 0$)

$$F_{ft} = \left(\frac{\sigma_{11}}{X^t}\right)^2 + \alpha\left(\frac{\sigma_{12}}{S^l}\right) \geq 1 \tag{2-3}$$

Fiber compression failure ($\sigma_{11} \leq 0$)

$$F_{fc} = \left(\frac{\sigma_{11}}{X^c}\right)^2 \geq 1 \tag{2-4}$$

Matrix tension failure criterion ($\sigma_{22} \geq 0$)

$$F_{mt} = \left(\frac{\sigma_{22}}{Y^t}\right)^2 + \left(\frac{\sigma_{12}}{S^l}\right)^2 \geq 1 \tag{2-5}$$

Matrix compression failure criterion ($\sigma_{22} \leq 0$)

$$F_{mc} = \left(\frac{\sigma_{22}}{2X^t}\right)^2 + \left[\left(\frac{Y^c}{2S^t}\right)^2 - 1\right] + \left(\frac{\sigma_{12}}{S^l}\right)^2 \geq 1 \tag{2-6}$$

where X^t and X^c represent the tension and compression strengths in the longitudinal (fiber) directions; Y^t and Y^c describe the tension and compression in the transverse direction; and S^l and S^t are the longitudinal and transverse shear strengths.

In the literature, there are a lot of attempts to improve Hashin criteria. The fiber failure criteria of Hashin has been accepted anonymously, while several modifications have been proposed for the matrix failure criteria. The most well-known modification was done by Puck and Shurmann (1998). Puck and Shurmann modified Hashin failure criteria to accurately predict inter-laminar fracture failure in laminated composites. Firstly, they suggested that the failure criteria must be defined based on the stress components acting on the potential fracture plane and its corresponding strengths. Therefore, the nominal strengths that are measured from mechanical tests cannot be used in the failure criteria. Secondly, they assumed that the transverse compressive stress on the potential fracture plane does not contribute to initiating the failure, and the failure initiation is mainly caused by the two shear stress components as illustrated in Figure 2.12. Actually, the compressive stress increases the shear resistance, proportional to the friction between two fracture surfaces.

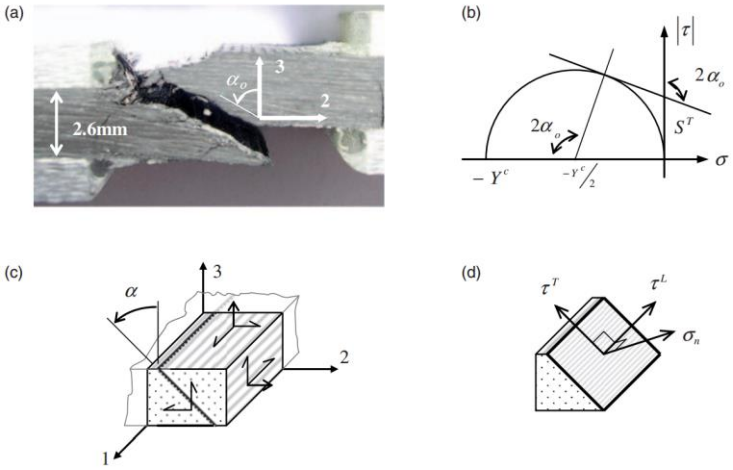

Figure 2.12: Stress components acting on the potential fracture plane (Pinho et al., 2012)

In order to apply these assumptions, a failure criterion based on the Mohr-Coulomb theory was developed by the authors as follows:

$$F_{mc} = \left(\frac{\sigma_{nt}}{S_{23} + \mu_{nt}\sigma_{nn}}\right)^2 + \left(\frac{\sigma_{nl}}{S_{12} + \mu_{nl}\sigma_{nn}}\right)^2 \geq 1 \qquad (2\text{-}7)$$

where σ_{nn}, σ_{nt}, σ_{nl} are the normal stress and transverse and longitudinal shear stresses on the fracture plane, respectively. S_{23} and S_{12} represent the corresponding shear strength on the fracture plane. The constant μ_{nt} and μ_{nl} describe the fraction of fracture surfaces.

Recently, Catalanotti et al. (2013) proposed new three-dimensional failure criteria for unidirectional composite laminates. They argued that Puck's failure criteria do not predict precisely the failure of plies embedded in multidirectional laminates. They revealed that it is required to use the in-situ strengths whose values increase, once a ply implants in multidirectional laminates. Therefore, the transverse tensile and shear strengths, as well as the compressive transverse strength should be computed based on the ply thickness.

Furthermore, they showed that the accuracy of Puck's tensile criterion depends on relations amongst the material strengths. For example, the criterion predicts correctly the failure initiation under pure transverse tension only if $Y^T \leq \sqrt{2}S_{23}$. Y^T and S_{23} are the transverse tensile strength and the transverse shear strength respectively. Therefore, the failure criteria were modified to take into account the influence of in-situ condition as follows:

$$F_{\mathrm{mt}} = \left(\frac{\sigma_{\mathrm{nn}}}{S_{\mathrm{t}}^{is}}\right)^2 + \left(\frac{\tau_{\mathrm{nl}}}{S_{\mathrm{l}}^{is}}\right)^2 + \left(\frac{\tau_{\mathrm{nt}}}{S_{\mathrm{t}}^{is}}\right)^2 + \lambda\left(\frac{\sigma_{\mathrm{nn}}}{S_{\mathrm{t}}^{is}}\right)^2\left(\frac{\tau_{\mathrm{nl}}}{S_{\mathrm{l}}^{is}}\right)^2 + \kappa\left(\frac{\sigma_{\mathrm{nn}}}{S_{\mathrm{t}}^{is}}\right)^2 \geq 1 \qquad (2\text{-}8)$$

where κ and λ are computed by $\kappa = \left(S_l^{in^2} - Y_t^{is}\right)/S_t^{is}\,Y_t^{is}$ and $\lambda = 2\mu_{nl}S_t^{is}/S_l^{is} - \kappa$. In addition, Y_t^{is}, S_t^{is} and S_l^{is} are the in-situ matrix tensile strength and shear strength in the transverse and longitudinal directions, respectively.

2.5.2 Failure propagation

When damage initiates in laminated composites (the failure indices attains one), the constitutive law must be modified to simulate the propagation of cracks/damage in the composite materials. The damage propagation of various failure modes can be treated in different ways. In general, the damage propagation is modelled using a strain-softening process. This approach originally was proposed for cohesive elements in the work of Camanho et al. (2002). The strain-softening process starts from point A (in Figure 2.13) and follows line A-C to reach the completely damaged state. As mentioned previously, an internal damage variable is used to define the evolution of damage propagation.

Moreover, stiffness reduction must be performed in a manner that the energy dissipated (by the numerical model) per unit area of crack growth should be equal to the fracture energy of the material for a specific failure mode. The area under the bilinear curve represents the energy dissipated during the damage evolution. The damage models based on continuum damage mechanics are often constructed in the framework of the thermodynamics in which the positivity of dissipation is interpreted as the damage can only grow (damage growth is an irreversible process).

Once a partially damaged state *B* happens, the line *B-O* will be followed under the unloading conditions. The unloading behavior of the material is always elastic linear as shown in Figure 2.13.

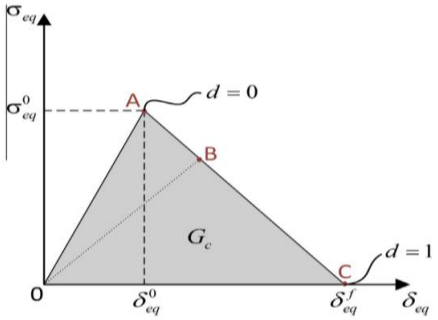

Figure 2.13: Bilinear response of intra-laminar damage model (Topac et al., 2016)

Pinho et al. (2012) introduced two physically-based scenarios for matrix failure propagation regarding the fracture angle of multidirectional laminated composites. The fracture angle is the maximum angle between the fracture surface and the normal plane. When the fracture angle is equal to zero, the creation of the first crack triggers the creation of further cracks, until it reaches a saturation point at which delamination occurs (see Figure 2.14a). Once the fracture angle is not equal to zero, a wedge effect initiates delamination after the creation of the first crack, as shown in Figure 2.14b.

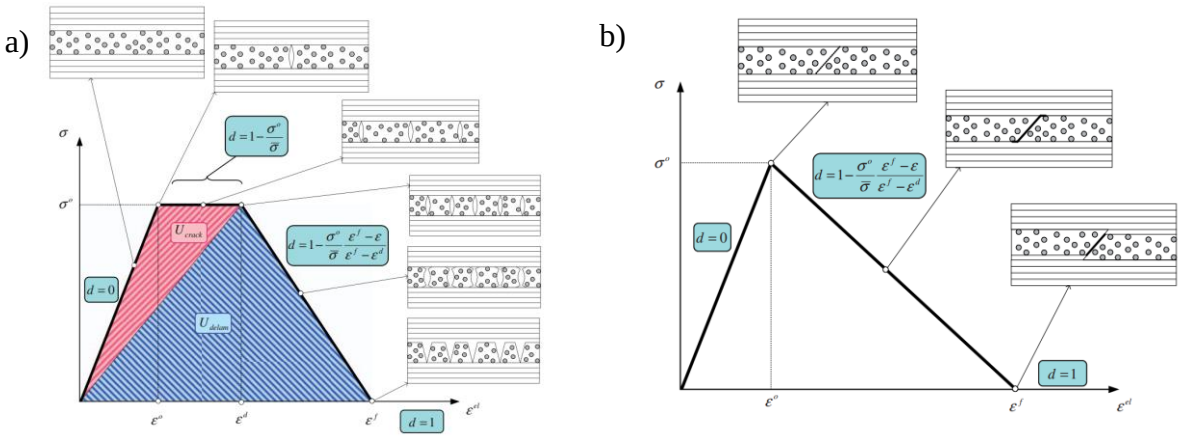

Figure 2.14: a) cracks propagation for an angle equal to 0 and b) cracks propagation for an angle other than 0 (Pinho et al., 2012)

The expressions of damage evolution in the CDM is maybe the most erratic part of the model development. The evolution equations depend on the damage behavior of the material. Williams and Vaziri (2001) used three damage growth parameters based on a Weibull distribution of strength:

$$d = 1 - exp\left[-\frac{1}{m\,e}\left(\frac{E\,\varepsilon_f}{X}\right)^m\right] \tag{2-9}$$

where E, ε_f and X represent the elastic modulus, failure strain and material strength respectively, e is the base of natural logarithm and m describes the shape of damage propagation curve. A quadratic expression was also used by some researchers to define the damage evolution parameter (Donadon et al., 2009; Zhou et al., 2015):

$$d = 1 - \frac{\varepsilon_0}{\varepsilon}[1 + \kappa^2(2\kappa - 3)] \tag{2-10}$$
$$\kappa = \frac{\varepsilon - \varepsilon_0}{\varepsilon_f - \varepsilon_0}$$

In general, a linear expression has been used for damage evolution in the CMD as follows:

$$d = \frac{\varepsilon_f}{\varepsilon_f - \varepsilon_0}\left(1 - \frac{\varepsilon_f}{\varepsilon}\right) \tag{2-11}$$

where ε_o correspond to the failure initiation strain and ε_f correspond to the maximum strain.

2.5.2.1 Smeared cracking formulation

One of the main problems in continuum damage mechanics is strain localization caused by degradation of element material properties, and the mesh dependency of FEM solution. This problem leads to decrease of calculated energy absorption with the reduction in the element size. Generally, a smeared formulation is applied to overcome the problem of strain localization. The main idea of the smeared cracking is to create a relation between the volumetric energy (energy dissipated per unit volume (Pinho et al., 2006)) and the fracture energy of material. As consequence of this method, the constitutive law of material must include a parameter related to the element dimensions in order to attain a constant fracture energy independent of the element dimensions. To demonstrate the method, the entire plate shown in Figure 2.15 is modeled as one element. The failure energy of the element can be calculated from:

$$U = L_1 L_2 L_3 \times \frac{\sigma_o \varepsilon_f}{2} \tag{2-12}$$

According to fracture mechanics principles, this energy must be equal to an energy per unit area multiplied by the dimensions of fracture area $A=L_1 \times L_3$ as follows:

$$U = G_f \times L_1 L_3 \tag{2-13}$$

Therefore, the strain at failure can be described as function of the energy per unit of area, the tensile strength and the geometric dimension, which is defined as characteristic length:

$$\varepsilon_f = \frac{2G_f}{\sigma_o L_2} \tag{2-14}$$

The two parameters of G_f and σ_o are material constants, but L_2 depends on the mesh refinement. Thus, an element length parameter enters into the material constitutive law. It must be mentioned that there is an upper limit for the characteristic length value. The elastic energy of element at the failure initiation must not be higher than the energy released during damage propagation, it means:

$$l^* \leq \frac{2EG_f}{\sigma_o^2} \tag{2-15}$$

where l^* is the characteristic length and E is Young's modulus. Pinho et al. (2006) used a relatively simple approach to approximate the characteristic length, but their approach restricted to the brick elements. Donadon et al. (2008) developed an objectivity algorithm to calculate the characteristic length from the shape function of element and performed a mesh sensitivity study using non-structured meshes. Chiu et al. (2015) introduced a more general algorithm to compute the characteristic length. They claimed that Donadon algorithm cannot represent the fracture plane generated in a non-zero degree ply.

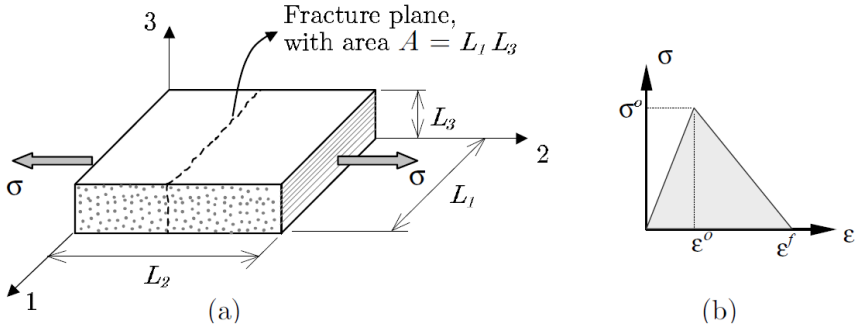

Figure 2.15: a) A unidirectional composite under transverse tension and b) material behvaior with failure (Pinho et al., 2006)

2.6 Interlaminate failure simulation

Delamination is a crucial damage mode in thick laminated composites and has been seen frequently in low-velocity impact tests. To simulate the delamination initiation and propagation, two

approaches have been generally used in the literature: Virtual Crack Closure Method (VCCM) and Cohesive Zone Model (CZM).

Cohesive elements are used to explicitly represent displacement discontinuities occurred with the crack formation. These elements create a relation between displacement discontinuity of a crack and tractions acting across the crack. A traction-separation law based on continuum damage mechanics includes a linear elastic behavior up to damage initiation and then follows by damage propagation. Ply interfaces in actual applications are subjected to multi-axial loading which originates a mixed-mode delamination. Therefore, the failure initiation of cohesive elements is generally a mixed-mode quadratic stress/strain based criterion including a normal and two shear modes, as illustrated in Figure 2.16. This signifies that damage can initiate at stress levels less than the maximum stress for a pure normal or shear mode. Once the quadratic stress criterion is equal to one, the delamination damage initiates.

$$\left(\frac{\langle \tau_n^{max} \rangle}{T_n^{max}}\right)^2 + \left(\frac{\tau_s^{max}}{T_s^{max}}\right)^2 + \left(\frac{\tau_t^{max}}{T_t^{max}}\right)^2 \geq 1 \qquad (2\text{-}16)$$

where $\tau_i^{max}, T_i^{max}\ at\ i = n, s, t$ are the interfacial stress and strength, respectively, corresponding to the initiation of separation for a pure mode.

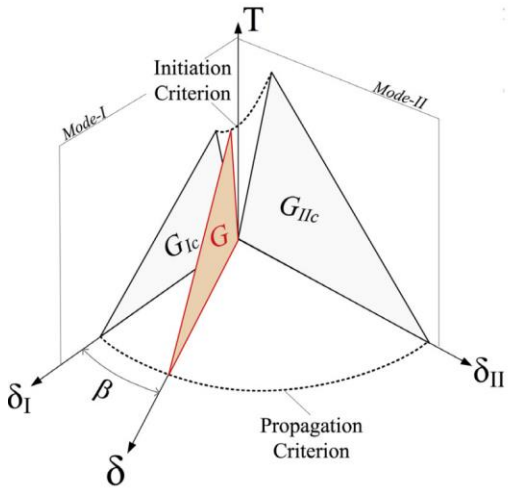

Figure 2.16: Constitutive law of cohesive zone model (Topac et al., 2016)

The initial slope of the traction-separation curve is an important variable for simulating interface delamination. The low value of stiffness can make the laminate too compliant. While the high value of stiffness can make spurious oscillations of the tractions in the cohesive element and leads to

numerical difficulties. Turon et al. (2007) proposed following expressions to estimate the initial stiffness values:

$$K_I \approx \left(\frac{50E_3}{t}\right) \ and \ \ K_{II} \approx \left(\frac{50G_{12}}{t}\right) \tag{2-17}$$

where E_3 is Young's modulus in the thickness direction, t is the maximum of ply thicknesses above or below the cohesive element.

Once intra-laminar damage initiates, the traction is reduced linearly with increasing separation until it becomes zero at the critical separation. The area under the traction-separation curve for each pure mode represents the fracture toughness. Fracture toughness of Mode I is obtained from DCB (double cantilever beam) tests and fracture toughness of Mode II is measured from ENF (end notch flexure) tests. Fracture toughness of Mode III is considered to be equal to the fracture toughness of Mode II. The critical separation can be calculated by knowing the fracture toughness and interfacial strength (T) as follows:

$$\delta_{c,i} = \frac{2G_{ic}}{T} \ , \qquad i = I, II, III \tag{2-18}$$

Certain researchers used a quadratic evolution damage criteria to control damage propagation. The power index described the failure surface and is normally equal to 1 or 2. Since there are no appropriate mixed-mode tests that involve mode III, a reliable mixed-mode propagation criterion for delamination propagation cannot be found (Camanho et al., 2002).

$$\left(\frac{G_I}{G_{Ic}}\right)^{\alpha} + \left(\frac{G_{II}}{G_{IIc}}\right)^{\alpha} + \left(\frac{G_{III}}{G_{IIIc}}\right)^{\alpha} \geq 1 \ , \qquad \alpha = 1 \ or \ 2 \tag{2-19}$$

Delamination also can be propagated by using a mixed-mode equation proposed by Benzeggagh and Kenane (B-K propagation criterion) (1996):

$$G_c = G_{Ic} + (G_{IIc} - G_{Ic}) \left(\frac{G_{II} + G_{III}}{G_I + G_{II} + G_{III}}\right)^{\eta} \tag{2-20}$$

where $G_i, i = I, II, III$ is the energy absorbed by the pure mode traction T_i during the separation δ_i , and η is the mixed-mode interaction constant determined from experimental tests.

2.7 Simulation of impact on sandwich structures

The impact response of sandwich composites has been the focus of a few number of investigations compared to monolithic laminates. The simulation of the impact response of sandwich panels is more complex than that of monolithic laminates because the response of laminated face sheet is significantly affected by the core material properties.

In order to decrease the computational effort and time of numerical models, shell elements considering only in-plan damage modes have been used to simulate damage propagation in the face sheet. Besant et al. (2001) used, for instance, 8-node shell elements for the face sheet and solid elements for the core to simulate the impact behavior of sandwich panels with an aluminum honeycomb core. The in-plane damage of the laminated face sheet was simulated using the Chang-Chang failure models. Shell elements in combination with the Chang-Chang damage model were also used in other studies (Klaus et al., 2012) to simulate in-plane fiber and matrix damage occurring in the plies of the impacted sandwich panels. Klaus et al. (2012) modeled the delamination between plies by using a tiebreak contact formulation to connect the shell elements representing each individual ply.

A refined multilayered skin model developed by Icardi and Ferrero (2009) was used to simulate impact-induced damage in carbon fabric/Nomex honeycomb sandwich. The onset of inter-laminar damage and delamination in laminated skins was modeled using stress-based failure criteria, and post-failure degradation of the material properties was performed by a ply-discount approach.

Solid elements were used in a limited research to model damage propagation in laminated face sheets of sandwich with foam core. The Hou failure criteria for fiber failure, matrix failure and delamination were used by Ivanez et al. (2010) to simulate the impact-induced damage in the glass/polyester face sheet of foam-based sandwich beams. When damage is detected in an element, the stresses are reduced to near-zero to reproduce the material stiffness degradation.

Fang and Aymerich (2014) used an explicit 3D finite element model to predict the damage onset and growth in foam-based sandwich composites under low-velocity impact. The model can simulate the intra-laminar and the inter-laminar damage (using cohesive laws) in the laminated face sheet. The nonlinear response of the foam core was modeled using a crushable foam core.

2.8 Material selection for composite stay vane extension

2.8.1 Face sheets material

Extensive use of composite materials in the aerospace and energy production industries is accompanied with the development of the new textile reinforcements to meet industrial requirements such as reducing manufacturing costs and easy-manufacturing process. One promising textile reinforcement which can satisfy these requirements is non-crimp fabrics (NCF). Compared to conventional reinforcements, NCF reinforcement offers relatively good mechanical properties, high deposition rate and low manufacturing costs. In the NCF textile, two or three layers of oriented fiber are stacked and stitched together. The thickness of this fabric layer is normally twice that of a conventional layer which facilitates a faster hand lay-up procedure.

In the recent past, many experimental studies have been performed on non-crimp fabrics and on the differences among their behavior and that of composites made with unidirectional and woven fabrics. For instance, the tensile strength of NCF laminate was found to be as the same as UD prepreg. However, its tensile stiffness decreases by 5% compared to UD prepreg. According to Edgren et al. (2008), the fatigue life of NCF laminate is similar to the fatigue life of UD prepreg. In addition, NCF laminates have been proven to demonstrate higher out-of-plane fracture resistance and impact damage tolerance compared to UD prepreg (Tsai et al., 2005). All these advantages make the NCF reinforcement a good choice for manufacturing the sandwich panels via vacuum infusion process.

2.8.2 Core material

The behavior of sandwich composite structures is significantly affected by the core material properties. The main functions of the sandwich core are to transfer load between the two face sheets, to support the transverse shear load and to improve the impact resistance.

In this application, it is required to choose a core material which can bear a relatively high impact energy and also increase the damage resistance of sandwich structure. A review of related literature shows that there are a few sandwich constructions which can withstand high impact energies in the range of 60 J -100 J, without suffering from large damage area. For example, a hybrid core-based sandwich panel made with horizontal metallic millitubes and polymer matrix (see Figure 2.6), has

good load bearing capacity according to the study presented in Ref. (Ji et al., 2013). The response of sandwich panel under low-velocity impact at 190 J is shown in Figure 2.17. The experimental results show that a significant amount of impact energy was dissipated through damage and plastic deformation in the polymer and the aluminum millitubes. However, the disadvantage of this structure is the large permeant deformation in the face sheet and core due to the irreversible deformation in the millitubes. Furthermore, the on-site fabrication of the sandwich seems to be difficult due to the presence of the aluminum millitubes.

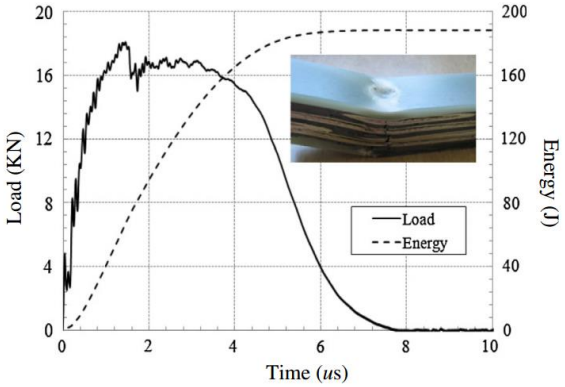

Figure 2.17: Low-velocity impact response of sandwich panel at 190 J (Ji et al., 2013)

In the earliest stage of this project, several sandwich constructions with different core materials, such as a foam/epoxy core, an ATH/epoxy core and a double core made of ATH/epoxy and extruded polystyrene (XPS) foam, were analyzed under low-velocity impact tests. After preliminary study (Ouadday, 2013), an innovative sandwich construction made of glass/epoxy laminated face sheets and the ATH/epoxy core is selected to fabricate stay vane extension structure. In the literature, there is no information about the impact behaviour and resistance of this sandwich panel, which is the main objective of this research.

CHAPTER 3 ARTICLE 1: VISCOPLASTIC-DAMAGE MODEL FOR LOW-VELOCITY IMPACT SIMULATION OF NON-CRIMP FABRIC-REINFORCED COMPOSITES

G. Morada, R. Ouadday, A. Vadean, R. Boukhili. Submitted to the International Journal of Solids and Structures on March 30, 2017.

3.1 Abstract

This paper is concerned with the development and validation of a viscoplastic-damage model to predict the damage initiation and propagation in Non-Crimp Fabric (NCF) reinforced composites subjected to low-velocity impact. The composite damage model based upon the continuum damage mechanics includes a mixed-mode matrix damage propagation model for intra-laminar damage prediction and an enhanced nonlinear shear-strain behavior law. The novel approach considers strain rate effects and a symmetric reversal loading in the shear-strain behavior. The interface cohesive elements was used to simulate inter-laminar damage. Low-velocity impact tests at varying energy levels were also performed on NCF glass/epoxy composites $[\{90°/0°/90°\}]_{3s}$ to demonstrate the impact resistance of this promising reinforcement architecture. Experimental results were compared to numerical predictions, and a good correlation was obtained. The proposed model is able to capture well the permanent deformation and shear stiffness reduction in cyclic shear tests. It was found that increased strain rate is accompanied by increased shear modulus and strength. The effects of strain rate on the damage resistance of glass laminates were also demonstrated by performing quasi-static tests.

3.2 Introduction

Amongst the available textile reinforcements, non-crimp fabrics (NCF) have received particular consideration from composite manufacturers because of their distinct advantages. NCF is a multiaxial reinforcement in which two or more unidirectional plies are stacked in different orientations and stitched together using through-thickness stitching, knitting or a chemical binder (Drapier et al., 1999; Edgren et al., 2005). In the NCF textile architecture, the fiber waviness associated with woven fabrics is avoided (Edgren et al., 2008). This allows for better use of the

elastic and strength properties of the fiber (Truong et al., 2005). In addition, NCF exhibits enhanced impact damage tolerance and fatigue resistance as compared with pre-impregnated fabrics (Edgren et al., 2008; Vallons et al., 2010).

In light of the benefits mentioned above, NCF represents an attractive structural material for several specific engineering applications, such as the rear pressure bulkhead of the Airbus A380 and wind turbine blades. Nevertheless, such structures are exposed to impacts during their lifetimes — a potential source of damage to composite structures. Unlike impacts at high velocities which often result in detectable damage (e.g. complete penetration), low-velocity impacts can generate extensive internal damage without visible evidence. These include matrix cracking, delamination, and fiber breaking. Among them, invisible delamination can cause significant reduction in local material strengths (Abrate, 2005). For this reason, the interface delamination requires improvement using a new NCF laminate architecture. Besides, there is a strong need for robust numerical tools capable of predicting damage growth and the interaction between the damage mechanisms within the composite material (Soutis et al., 1996). Extensive work has been done in modelling the behavior of NCF under quasi-static loadings (e.g. (Edgren et al., 2006; Joffe et al., 2005)). However, to the best of our knowledge, few numerical studies in the literature have been developed to predict the behavior of NCF laminates under impact loads (Greve et al., 2006; Satyanarayana et al., 2014).

In the last few decades, numerous composite damage models based upon the continuum damage mechanics (CDM) approach have been developed to predict the mechanical behavior of different composite laminates under various loading conditions. The CDM approach accounts for the effects of damage on the evolution of the material stiffness by means of scalar damage variables (internal state variables). These intra-laminar models are usually used in combination with cohesive elements to simulate the impact-induced delamination. Donadon et al. (2008) and Faggiani and Falzon (2010) improved a continuum damage model by taking into account the non-linear matrix shear behavior and irreversible shear deformations. The drawback of their models is the need to perform cyclic shear tests in order to define the nonlinear shear behavior and permanent shear strain. Furthermore, according to Donadon et al. (2008), the shear behavior and failure modes of composite materials are strain rate dependent which are not considered in these models. Joki et al. (2015) also mentioned the need for a viscoelastic model to reproduce precisely the nonlinear shear behavior of NCF laminated composite. Therefore, improving existing damage models requires the

formulation of a more effective and easily implemented model in which material strain rate sensitivity is considered.

Furthermore, it should be pointed out that the CDM approach leads to strain localization problem, which itself results in spurious mesh-size-dependence. In order to alleviate the localization problem, all of the CDM-based damage models adopted the well-known crack band model (Bažant et al., 1983). Consequently, a characteristic element length was introduced into the damage governing equations to adjust the fracture energies during the damage propagation stage (Donadon et al., 2008).

The main purpose of this paper is to develop and validate a full 3D composite viscoplastic-damage model to predict the damage mechanisms in NCF composite laminates subjected to impact loads. Indeed, the composite damage model proposed by Donadon et al. (2008) is improved by using a viscoplastic model to define inelastic shear strain. A nonlinear shear behavior initiates with the creation of micro-cracks in laminated composites. The model also includes a mixed-mode matrix damage initiation and propagation law which reduces the number of damage parameters to just two. The proposed model was written in a user defined material (UMAT) subroutine and implemented in the LS-DYNA 3D explicit finite element code in conjunction with cohesive finite elements. The capacity of the model to predict the plastic deformation with consideration of material strain rate dependence is firstly validated by performing shear tests under various strain rates. Then, the effectiveness of the proposed model was verified by comparing the numerical predictions with experimental data obtained from drop-weight impact tests and from micrographs for various impact energies ranging from below to above the barely visible impact damage (from 5 J to 53 J).

3.3 Development of the constitutive model

3.3.1 Continuum damage mechanics

The intra-laminar constitutive law was described as a homogeneous orthotropic material in combination with a physically-based continuum damage mechanics theory as well as the matrix dominated nonlinear behavior. According to experimental results, a nonlinear and irreversible shear behavior was frequently reported in composite laminates (Donadon et al., 2008). The nonlinear behavior of composite material was described herein by using an inelastic shear strain

γ_{ij}^{in}. The inelastic strains in the other directions ε_{ii}^{in} were assumed insignificant. Therefore, the elastic Hooke's law for linear orthotropic materials was modified to consider the nonlinear shear behavior as follows:

$$\begin{bmatrix}\sigma_{11}\\ \sigma_{22}\\ \sigma_{33}\end{bmatrix}=\frac{1}{\Omega}\begin{bmatrix}E_{11}(1-v_{23}v_{32}) & E_{22}(v_{12}-v_{32}v_{13}) & E_{33}(v_{13}-v_{12}v_{23})\\ E_{11}(v_{21}-v_{31}v_{23}) & E_{22}(1-v_{13}v_{31}) & E_{33}(v_{23}-v_{21}v_{13})\\ E_{11}(v_{31}-v_{21}v_{31}) & E_{22}(v_{32}-v_{12}v_{31}) & E_{33}(1-v_{12}v_{21})\end{bmatrix}\begin{bmatrix}\varepsilon_{11}\\ \varepsilon_{22}\\ \varepsilon_{33}\end{bmatrix} \quad (3\text{-}1)$$

$$\Omega = 1 - v_{12}v_{21} - v_{23}v_{32} - v_{31}v_{13} - 2v_{21}v_{32}v_{13}$$

The nonlinear shear stress-strain part of the constitutive model was assigned as:

$$\tau_{ij} = G_{ij}\left(\gamma_{ij} - \gamma_{ij}^{in}\right), \qquad i\ and\ j = 1,2,3 \quad (3\text{-}2)$$

The inelastic part of the strain tensor γ_{ij}^{in} was estimated using a viscoplastic model which is described in the next section.

Recent research has revealed that the damage propagation in the polymeric composite structure appears in the form of strain-softening of the material. The strain-softening behavior can be taken into account via continuum damage mechanics theory. Thereby, the strain-softening in each ply of laminate was described using two internal damage variables d_f and d_m corresponding to fiber damage and matrix damage respectively. Once fiber damage initiates, the undamaged longitudinal stress σ_{11} is degraded by the damage variable d_f, as shown in following equation. After matrix damage onset, the stress components are first rotated into the potential fracture plane ($\sigma_{123} \xrightarrow{\theta} \sigma_{ntl}$, θ is the angle of fracture plane). Then, the rotated stress components are reduced by the damage variable d_m ($\sigma_{ntl} \xrightarrow{dm} \sigma_{ntl}^{d}$) and finally transformed back into the original plane ($\sigma_{ntl}^{d} \xrightarrow{\theta} \bar{\sigma}_{123}^{d}$).

$$\sigma^{d} = \begin{Bmatrix}\sigma_{11}(1-d_f)\\ \bar{\sigma}_{22}^{d}\\ \bar{\sigma}_{33}^{d}\\ \bar{\tau}_{12}^{d}\\ \bar{\tau}_{23}^{d}\\ \bar{\tau}_{31}^{d}\end{Bmatrix}, (\sigma_{123} \xrightarrow{\theta} \sigma_{ntl} \xrightarrow{dm} \sigma_{ntl}^{d} \xrightarrow{\theta} \bar{\sigma}_{123}^{d}) \quad (3\text{-}3)$$

3.3.2 Viscoplastic model

Polymer matrix composites demonstrate a nonlinear plastic and strain-rate dependent response, particularly for matrix-dominated mechanical properties such as shear-strain behavior. This behavior is mainly caused by the viscoplastic nature of resins. In this model, the plastic deformation is only considered in shear strain components. The Bodner-Partom model (2001) was applied to define a viscoplastic relationship. According to this model, the accumulated inelastic shear stain at the time $t+\Delta t$ can be expressed as:

$$\gamma_{ij}^{in}|_{t+\Delta t} = \gamma_{ij}^{in}|_t + \Delta t \dot{\lambda} \tau_{ij} \tag{3-4}$$

where $\dot{\lambda}$ is the factor of proportionality which can be defined as:

$$\dot{\lambda} = \frac{D_0}{2\sqrt{J}} exp\left[-\frac{1}{2}\left(\frac{Z}{\sigma_e}\right)^{2n}\right] \tag{3-5}$$

where D_0 and n are material constants. The value of n controls rate dependence of the material. In this model, the effect of the hydrostatic stresses is neglected for simplification. The effective stress σ_e is expressed as follows:

$$\sigma_e = \sqrt{3J} \tag{3-6}$$

where J is the second invariant of the deviatoric stress tensor. The evolution of the internal stress variable Z can be expressed as:

$$\dot{Z} = q(Z_1 - Z)\dot{e}_e^I \tag{3-7}$$

where q is related to the hardening rate and Z_1 represents the maximum value of Z. The initial value of Z is defined by the material constant Z_0. The initial value of Z (Z_0) affects the onset of nonlinearity, with a greater values of Z_0 resulting in a stiffer material. The maximum value of Z (Z_1) controls the maximum stress. Finally, the effective deviatoric inelastic strain rate (the term $\dot{e}_e^I$ in Eq. (3-6)) is defined as follows:

$$\dot{e}_e^I = \sqrt{4/3(\dot{\gamma}_{12}^2 + \dot{\gamma}_{23}^2 + \dot{\gamma}_{13}^2)} \tag{3-8}$$

The parameters n, Z_0, Z_1 and q can be obtained from shear tests. The procedure to select the values of these parameters is well explained in the work of Goldberg et al. (1999). The parameter D_0 is assumed to 10^4 times the maximum applied strain rate which means that it is approximately equal to 10^6 s^{-1}. The values of all the parameters are presented in Table 3.2.

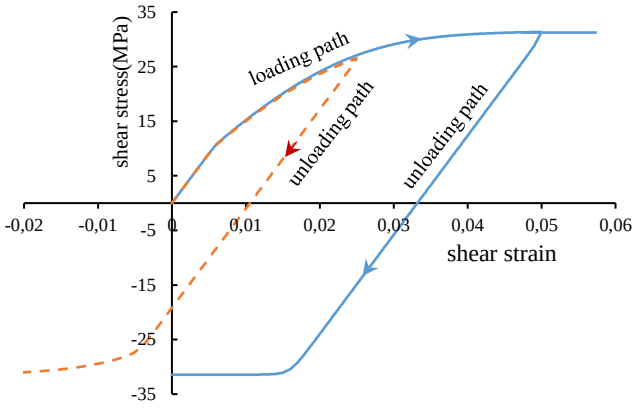

Figure 3.1: Non-linear shear-strain behavior with loading and unloading paths

The non-linear shear-strain behavior with loading and unloading paths is presented in Figure 3.1. A symmetric shear-strain response on load reversal was obtained automatically in this damage model without further computational effort. This reversal loading was not considered in other existing models, except the models proposed by Egan (2014) and Chiu (2015) which required additional implementation effort to define the load reversal. It is worthwhile to mention that this approach does not require performing cyclic tensile tests in order to describe the stress-strain behavior, unlike the model proposed by Donadon (2008), Faggiani (2010) and Feng (2013).

3.3.3 Strain-rate dependence of shear modulus and strength

One advantage of the numerical model implemented in this work is that the strain rate sensitivity of the shear modulus and strength of the E-glass fiber-reinforced composites has been considered. The composite laminate response in the fiber direction mostly is influenced by the fiber material properties. The plastic deformation and strain-rate dependency in fiber direction are assumed insignificant. It has been reported that glass fiber reinforced plastic laminates are rate sensitive under dynamic loading. The rate dependency of the modulus can be expressed as follows:

$$G_{ij} = G_{ij}^{0}\left(1 + C \times ln\frac{\dot{\varepsilon}}{\dot{\varepsilon}_0}\right) \tag{3-9}$$

$$S_{12} = S_{12}^{0}\left(1 + C \times ln\frac{\dot{\varepsilon}}{\dot{\varepsilon}_0}\right)$$

where *C* represents the strain rate sensitivity, and $\dot{\varepsilon}_0$ and $\dot{\varepsilon}$ are the reference and applied effective strain rate respectively.

3.4 Intra-laminar damage model

3.4.1 Fiber failure modes

Two strain-based failure criteria were used to detect fiber damage initiation under tensile and compressive loading:

$$F_{11}^{T} = \left(\frac{\varepsilon_{11}}{\varepsilon_{11}^{ot}}\right)^2 - 1 \geq 0 \tag{3-10}$$

$$F_{11}^{C} = \left(\frac{\varepsilon_{11}}{\varepsilon_{11}^{oc}}\right)^2 - 1 \geq 0$$

where ε_{11}^{ot} and ε_{11}^{oc} are the damage initiation strain in tension and compression. Once the damage initiates, the material begins gradually losing its stiffness until failure, as shown in Figure 3.2. The damage variables for tensile and compressive fiber failure are described by the following equations:

$$d_{11}^{t} = \frac{\varepsilon_{11}^{ft}}{\varepsilon_{11}^{ft} - \varepsilon_{11}^{ot}}\left(1 - \frac{\varepsilon_{11}^{ot}}{\varepsilon_{11}}\right)^2 \tag{3-11}$$

$$d_{11}^{c} = \frac{\varepsilon_{11}^{fc}}{\varepsilon_{11}^{fc} - \varepsilon_{11}^{oc}}\left(1 - \frac{\varepsilon_{11}^{oc}}{\varepsilon_{11}}\right)^2$$

where ε_{11}^{ft} and ε_{11}^{fc} are the maximum strains at failure which were calculated from the critical energy release rates (G_{11}^{t} and G_{11}^{c}), maximum longitudinal stresses (X^t, X^c) and characteristic length l^*:

$$\varepsilon_{11}^{ft} = \frac{2G_{11}^{t}}{X^{t}\, l^{*}} \; ; \quad \varepsilon_{11}^{fc} = \frac{2G_{11}^{c}}{X^{c}\, l^{*}} \tag{3-12}$$

One coupled tension-compression damage variable d_{1f} was utilized to simulate fiber degradation in the longitudinal direction which is defined as follows:

$$d_f = d_{11}^{c} + d_{11}^{t} - d_{11}^{t} d_{11}^{c} \tag{3-13}$$

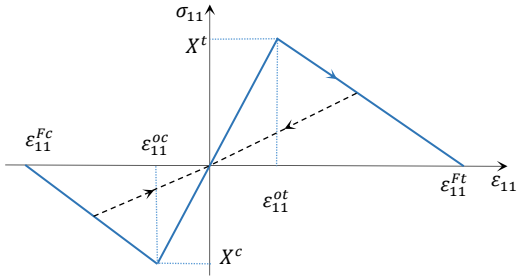

Figure 3.2: Intra-laminar damage model behavior for fiber failure

3.4.2 Matrix failure modes

Matrix damage initiation: Failure criteria proposed by Catalanotti et al. (2013) was used to detect matrix cracking and Puck failure criteria (1998) was used to identify matrix crushing as follows:

$$F_{22}^{T} = \left(\frac{\sigma_{\mathrm{nn}}}{S_{\mathrm{t}}^{is}}\right)^2 + \left(\frac{\tau_{\mathrm{nl}}}{S_{l}^{is}}\right)^2 + \left(\frac{\tau_{\mathrm{nt}}}{S_{\mathrm{t}}^{is}}\right)^2 + \lambda\left(\frac{\sigma_{\mathrm{nn}}}{S_{\mathrm{t}}^{is}}\right)^2\left(\frac{\tau_{\mathrm{nl}}}{S_{l}^{is}}\right)^2 + \kappa\left(\frac{\sigma_{\mathrm{nn}}}{S_{\mathrm{t}}^{is}}\right)^2 - 1 \geq 0 \tag{3-14}$$

$$F_{22}^{C} = \left(\frac{\tau_{\mathrm{nl}}}{S_{l}^{is} - \mu_{\mathrm{nt}}\sigma_{\mathrm{nn}}}\right)^2 + \left(\frac{\tau_{\mathrm{nl}}}{S_{\mathrm{t}}^{is} - \mu_{\mathrm{nl}}\sigma_{\mathrm{nn}}}\right)^2 - 1 \geq 0$$

where κ and λ are computed by $\kappa = \left(S_{l}^{in^2} - Y_{t}^{is}\right)/S_{t}^{is}\, Y_{t}^{is}$ and $\lambda = 2\mu_{nl} S_{t}^{is}/S_{l}^{is} - \kappa$. In addition, Y_{t}^{is}, S_{t}^{is} and S_{l}^{is} are the in-situ matrix tensile strength and shear strength in the transverse and longitudinal directions, respectively. Based on Mohr-Coulomb theory, the friction coefficients are defined as $\mu_{nt} = -1/\tan(2\theta_f)$ and $\mu_{nl} = \mu_{nt}\, S_{l}^{is}/S_{\mathrm{t}}^{is}$, where $S_{\mathrm{t}}^{is} = Y_{\mathrm{c}}^{is}/2\tan(\theta_f)$ and Y_{c}^{is} are the in-situ matrix compressive strengths. In our case, the maximum ply thickness in the simulation is

about 0.29 mm; thus, the in-situ strength values were calculated by using the thin ply equation given by Pinho et al. (2012).

The angle of the fracture plane θ_f is approximately 53° for a unidirectional laminate under pure compressive loading. The two criteria depend on the stresses in the potential fracture plane which can be calculated using the standard transformation matrix $T(\theta)$:

$$\sigma_{nlt} = [T(\theta)]\sigma_{123}[T(\theta)]^T \tag{3-15}$$

Figure 3.3 shows the potential fracture plane which is parallel with the longitudinal axis and makes an angle of θ with the vertical axis. The fracture plane orientation was found by an iterative procedure for each element.

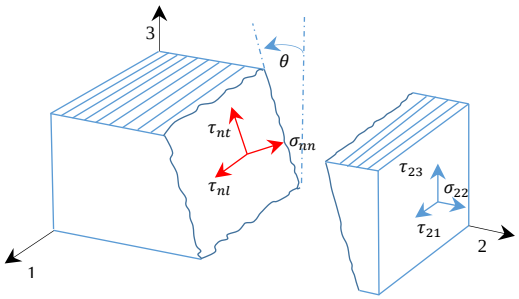

Figure 3.3: Fracture plane in compression loading

Matrix damage propagation: Once the matrix failure initiates under combined loading, the stress σ_r and corresponding strain ε_r on the potential fracture plane should be recorded.

$$\sigma_r = \sqrt{\langle\sigma_{nn}\rangle^2 + (\tau_{nt})^2 + (\tau_{nl})^2} \tag{3-16}$$

$$\varepsilon_r = \sqrt{\langle\varepsilon_{nn}\rangle^2 + (\gamma_{nt})^2 + (\gamma_{nl})^2}$$

$$\varepsilon^0_{\mathrm{r,in}} = \sqrt{(\gamma^{in}_{nt})^2 + (\gamma^{in}_{nl})^2}$$

In Eq. (3-15), $\varepsilon^0_{\mathrm{r,in}}$ is the inelastic component of strain at the moment of initiation and $\langle\,\rangle$ is the Macaulay bracket. The total strain energy G_r before damage onset; must be recorded. The total strain energy was defined as a quadratic combination of the volumetric strain energies corresponding with each stress acting on the potential fracture plane.

$$G_r = G_{nn}\left(\frac{\langle\sigma_{nn}\rangle}{\sigma_r}\right)^2 + G_{nt}\left(\frac{\tau_{nt}}{\sigma_r}\right)^2 + G_{nl}\left(\frac{\tau_{nl}}{\sigma_r}\right)^2 \tag{3-17}$$

The volumetric strain energy of each stress component can be estimated using:

$$G_i = \int_0^{\varepsilon_r} \sigma_i d\varepsilon_i \qquad i = nn, nt, nl \tag{3-18}$$

Then, the matrix damage parameter d_m is defined as function of strain:

$$d_m = \frac{\varepsilon_{\mathrm{r}}^f - \varepsilon_{\mathrm{r,in}}^0}{\varepsilon_{\mathrm{r}}^f - \varepsilon_{\mathrm{r}}^o}\left(\frac{\varepsilon_{\mathrm{r}}^0 - \varepsilon_r}{\varepsilon_r - \varepsilon_{\mathrm{r,in}}^0}\right) \tag{3-19}$$

where $\varepsilon_{\mathrm{r}}^f$ represents the final failure strain which is calculated from the critical strain energy release rate and characteristic length as follows:

$$\varepsilon_r^f - \varepsilon_r = \frac{2G_m}{\sigma_r l_m} - \frac{2G_r}{\sigma_r} \tag{3-20}$$

The fracture energy of the matrix under combined stresses can be estimated by the following equation:

$$G_m = G_{IC}\left(\frac{\langle\sigma_{nn}\rangle}{\sigma_r}\right)^2 + G_{IIc}\left(\frac{\tau_{nt}}{\sigma_r}\right)^2 + G_{IIC}\left(\frac{\tau_{nl}}{\sigma_r}\right)^2 \tag{3-21}$$

where G_{IC} and G_{IIC} are the critical strain energy release rates for modes I and II, respectively. Finally, the shear stresses and tensile stress on the fracture plane are updated by the following relations, and then, the updated stresses are transformed back into the original plane.

$$\sigma_{nl} = (1 - d_m)\sigma_{nl} \tag{3-22}$$

$$\sigma_{nt} = (1 - d_m)\sigma_{nt}$$

$$\sigma_{nn} = \sigma_{nn} - d_m\langle\,\sigma_{nn}\rangle$$

Details of the computation of the characteristic element lengths l_f and l_m can be found in Refs. (Donadon et al., 2008; Falzon et al., 2011). The main procedure of the inter-laminar damage implementation is shown in Figure 3.4.

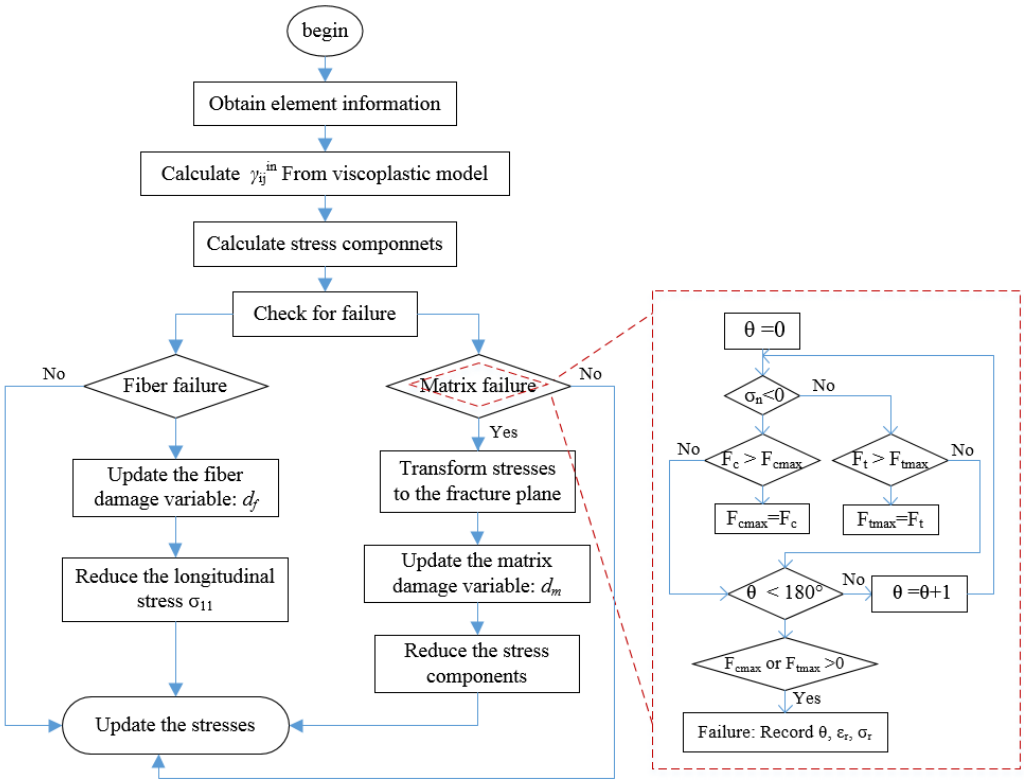

Figure 3.4: Flowchart of the process within UMAT subroutine

3.5 Inter-laminar damage model

Cohesive elements are generally used for simulating the delamination between two successive plies having different fiber orientations, defined by a linear traction-separation model. This model assumes elastic behavior until damage is initiated according to a stress-based quadratic interaction criterion. This is followed by decohesion of the two plies with damage propagation. Damage initiation was described by a quadratic stress-based criterion:

$$\left(\frac{\sigma_1}{N}\right)^2 + \left(\frac{\tau_2}{S}\right)^2 + \left(\frac{\tau_3}{S}\right)^2 = 1 \qquad (3\text{-}23)$$

where σ_1, τ_2, τ_3 are the interface tangential and normal stresses and N, S are the peak traction in the normal and tangential directions. The propagation of delamination was modelled with the Benzeggagh-Kenane law (1996) for mixed-mode loading. The ultimate mixed-mode displacement δ^F is:

$$\delta^F = \frac{1+\beta^2}{A_{TSLC}(N+\beta^2 S)}\left[G_{IC} + (G_{IIC} - G_{IC})\left(\frac{\beta^2 S}{N+\beta^2 S}\right)^{\eta}\right] \quad (3\text{-}24)$$

where β is the mixed mode ratio, η is the exponent of the mixed mode criterion, A_{TSLC} is the area under the load-displacement curve and G_{IC}, G_{IIC} are the inter-laminar fracture toughness in mode I, II.

3.6 Experimental tests

3.6.1 Materials and manufacturing

Glass fiber-reinforced epoxy laminates were manufactured using the vacuum assisted resin infusion (VARI) process. The epoxy resin system used in this study was Araldite® LY 8601 (base resin)/Aradur® 8602 (hardener) provided by Huntsman Advanced Materials Americas LLC (with a weight ratio resin/hardener of 100:25). This two-component epoxy resin has a low viscosity which makes it suitable for infusion processes. For reinforcement, a ({90°/0°/90°}) non-crimp E-glass fabrics (NCF) with a 744 g/m² areal density, provided by JB Martin under the reference TG-22-N was used. This particular fabric comprises two smaller 90° layers of 275 g/m² glass roving sandwich a heavier 0° layer of 1100 tex layer linked together using a polyester yarn (see Figure 3.5). The NCF glass fabrics were stacked with a $[\{90°/0°/90°\}]_{3s}$ lamination sequence to achieve a thickness of 3.66 mm. After resin infusion, the composite laminates were cured for more than 24h at ambient temperature. The fiber volume fraction was then measured according to ASTM D3171 (2011) and was found to be 52%.

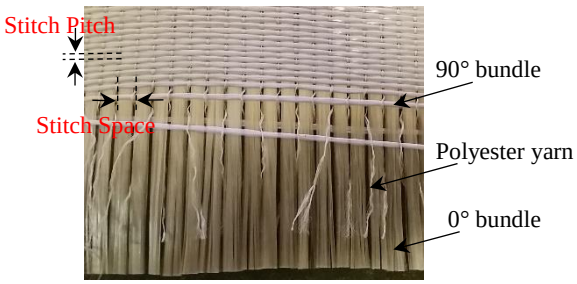

Figure 3.5: Internal architecture of the NCF reinforcement

3.6.2 Impact tests

Low-velocity drop-weight impact tests were carried out using a drop-weight tower (Instron Inc., Dynatup GRC 8250). Rectangular specimens (150 mm × 100 mm × 3.66 mm) were placed on a steel fixture according to the ASTM D7136 (2005) specifications and were clamped with four rubber-tipped clamps (leaving an opening area of 125 mm × 75 mm). A 5.5 kg mass impactor with a 16 mm diameter hemispherical nose shape was used to impact specimens at various energy levels from 5 J to 53 J by varying only the drop height. To prevent the specimens from multiple impacts during experiment, a pneumatic self-rebounding was used. Three specimens were tested for each impact energy level. Impact parameters (e.g. contact load, absorbed energy, displacement, and velocity) were continuously recorded for each specimen using a load cell and a velocity sensor.

Quasi-static tests were also executed on an instrumented MTS test machine at different rates of displacement. Almost exact replication of the impact test set-up was provided by using the same clamping boundary condition, and by using the same impactor to apply the static load.

3.6.3 Finite element model

The proposed damage model was written in a user defined material (UMAT) subroutine written in FORTRAN and implemented in the commercial 3D explicit finite element code, LS-DYNA. To reduce the computational time, only one-quarter of the specimen was built for simulation (see Figure 3.6).

The $[\{90°/0°/90°\}]_{3s}$ composite laminate and the interfaces of plies with different fiber-orientation angles were modelled using solid and cohesive elements, respectively. It is worth noting here that each fabric layer {90°/0°/90°} was modelled as three unidirectional plies with fiber oriented at 90°,

0°, and 90°, respectively (see Figure 3.6). The thickness of each ply was calculated using the balancing coefficient, *k*, defined as:

$$k = \frac{A_c}{A_c + A_t} \tag{3-25}$$

where A_c and A_t represent the fibers surface per unit width in the warp and weft directions, respectively (their values can be obtained from the material data sheet).

Both impactor and plate support were modelled using rigid elements, whereas the rubber-tipped clamp (which is used to restraint the specimen) was modelled as a cylinder-shaped rigid body of 8 mm diameter. A load of approximately 10 N (Lopes et al., 2016) was also applied on the rigid clamp. To account for the influence of dynamic contact force during the impact event, a surface-to-surface type contact element was used to simulate the contact of the impactor and the rigid clamp with the impact surface, as well as the contact between the support fixture and the specimen surface opposite to impact.

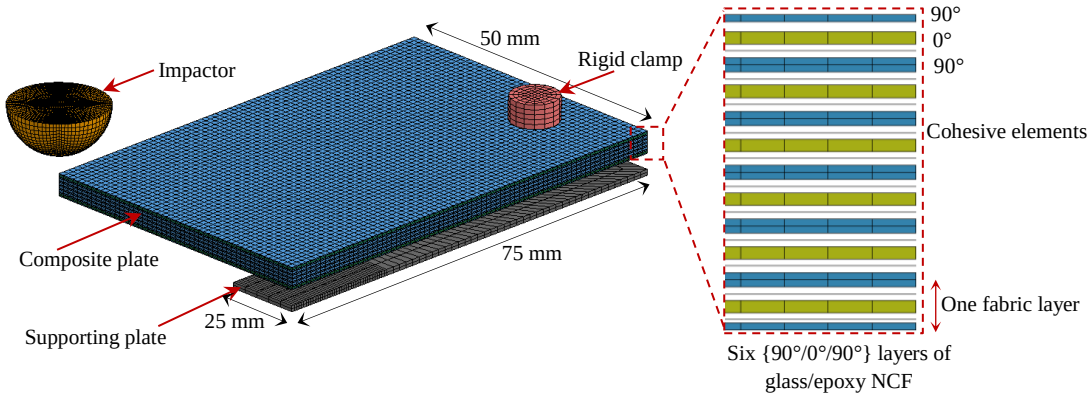

Figure 3.6: Finite element model for impact analyses

3.6.4 Material properties

The elastic and strength properties were obtained for the NCF glass/epoxy laminate, form a series of experimental tests conducted by our group. Tensile tests were carried out on $[\{90°/0°/90°\}]_{3s}$ specimens according to ASTM D3039M in both weft and warp directions. The tested specimens had 250 mm long, 25 mm wide and 3.66 mm thick with 150 mm gauge length. Compressive tests

were conducted on $[\{90°/0°/90°\}]_{3s}$ specimens of 81×12.7×3.66 mm^3 in accordance with the modified ASTM D695 standard, and with a gauge length of 4.8 mm. The fiber fracture energies (G_{ft} and G_{fc}) are gathered from experimental measurements provided by Roy et al. (2001). There was no available experimental data for the Mode I and Mode II fracture energies, for our specific NCF laminate. The experimental results for UD glass/epoxy composite were found to be G_{IC}=300 J/m^2 and G_{IIC}=500 J/m^2 (Andersons et al., 2010). The fracture energies for graphite/epoxy laminate obtained from double cantilever beam tests and end notched flexure tests are G_{IC}=520 J/m^2 and G_{IIC}=970 J/m^2, respectively (Aymerich et al., 2008). Preliminary numerical analysis showed that the fracture energies of G_{IC}=800 J/m^2 and G_{IIC}=1200 J/m^2 were the best fit to experimental results which were approximately the values obtained by Compston et al. (1998) for a tough epoxy resin. The initial stiffness values of the cohesive interface were estimated as k_N=50E_{33}/t and k_S=50G_{12}/t (Turon et al., 2007), whereas the cohesive strengths S and N were assumed to be matrix dominated properties, and thus N=Y_t and S=S_{12}. The mechanical properties of NCF laminate are summarized in Table 3.1.

Table 3.1: Material properties of an E-glass fiber/epoxy NCF laminate

Property	Values
Elastic properties	E_{11} = 34.4 GPa; E_{22} = E_{33} = 6.98 GPa; ν_{12} = ν_{13} = 0.28; ν_{23} =0.5 ;
Strength	X_t = 1100 MPa; X_c = 780 MPa; Y_t = 45 MPa; Y_c = 120 MPa ;
Intra-laminar fracture toughness	G_{ft} = G_{fc} =35000 J/m²; G_{Ic} = 800 J/m²; G_{IIc} = G_{IIIc} = 1200 J/m² ;
Interface properties	k_N = 120 GPa/mm; k_s = 48 GPa/mm; N = 45 MPa; S = 30 MPa; η = 1.4.

A comparison between the predicted and measured uniaxial tensile and compression tests along the warp and weft directions are presented in Figure 3.7.

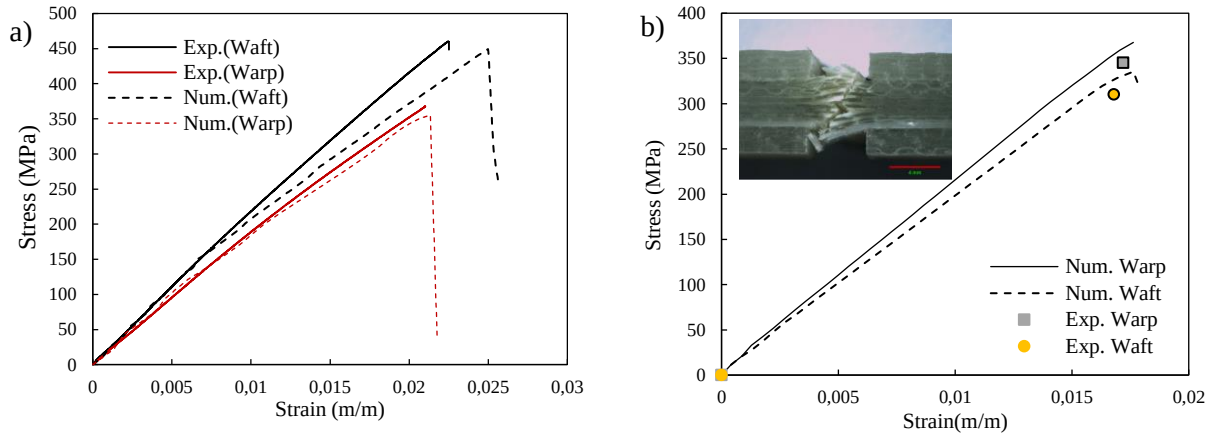

Figure 3.7: a) Tensile stress-strain response and b) compression stress-strain response of NCF laminates

The material constants of n, Z_0, Z_1 and q used in viscoplastic model were calculated from the procedure described by Goldberg et al. (1999). The values of all the parameters are listed in Table 3.2.

Table 3.2: Material constants of the viscoplastic model

Modulus(GPa)	Poisson's ratio	C	n	Z_0 (MPa)	Z_1(MPa)	q	$D_0(s^{-1})$	$\dot{\varepsilon}_0(s^{-1})$
3.8	0.28	0.195	0.93	126.9	603.8	279.26	10^6	10^{-3}

3.7 Results and discussion

3.7.1 In-plane shear test simulations

Cyclic tensile tests were performed in accordance with ASTM D3518 to verify the ability of the proposed numerical model to predict the permanent shear strain and also monitor the shear modulus degradation in a loading and unloading scenario. Three $[\{-45/+45/-45\}]_{3s}$ specimens were cut to a size of 250 mm × 25 mm × 3.66 mm and subjected to a cyclic tensile load. For the first cycle, each specimen was loaded up to a maximum tensile load of 2 kN and then completely unloaded. Thereafter, for each of the subsequent cycles, the maximum tensile load was increased by 1 kN with respect to the previous cycle. The strain rate was 2 mm/min during the loading, un-loading, and reloading stages.

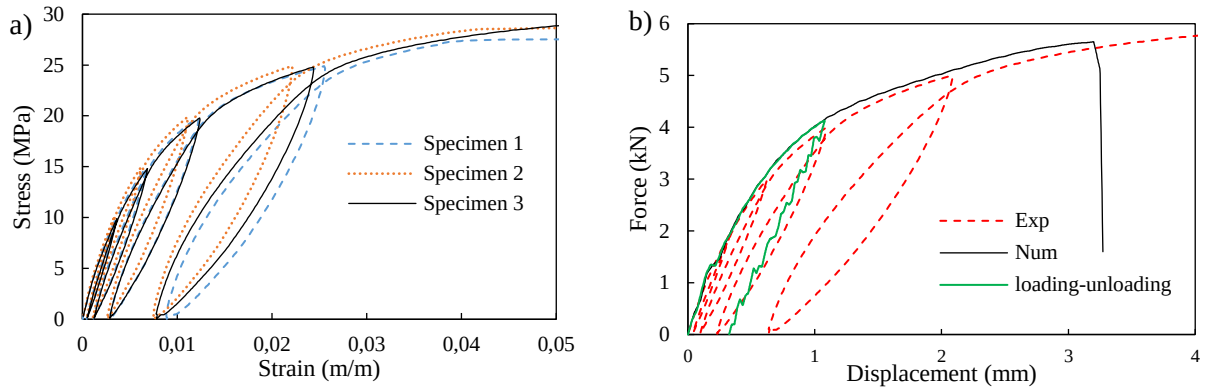

Figure 3.8: a) Nonlinear shear-strain curves obtained from experimental results, b) Tensile loading and unloading curves

The tensile stress-strain data recorded from the testing machine were transformed to assess the shear stress-strain curve according to the approach described in Ref. (Mallick, 2007), and the results are shown in Figure 3.8a. As expected, the results obtained indicate highly nonlinear behavior and considerable permanent shear strain after unloading, which results from several inelastic damage processes, including plastification and intra- matrix micro-cracking. A comparison between the experimental results and prediction of the tensile force-displacement curve is plotted in Figure 3.8b. The numerical results demonstrate that the viscoplastic model is able to accurately predict the nonlinear loading and linear unloading of shear specimens.

The experimental and numerical results of the relative shear stiffness degradation versus shear strain are shown in Figure 3.9. The obtained experimental data show that the relative shear stiffness degradation linearly reduces at low shear strains and then deviates from linearity at high shear strains. As shown, the viscoplastic model can accurately predict the shear stiffness degradation and plastic deformation observed in the experimental tests.

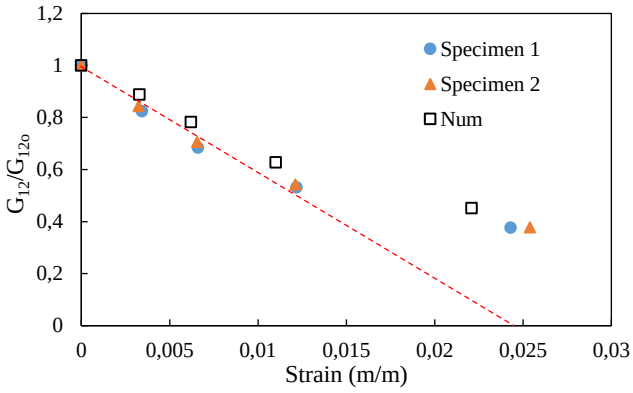

Figure 3.9: Relative shear stiffness degradation verse shear strain

The failed region of the shear specimens is shown in Figure 3.10, together with the failed region obtained from the numerical simulations. In this figure, the occurrence of necking before the final failure, as observed in the experimental tests, is well predicted numerically. This further confirms the appropriateness of the proposed model.

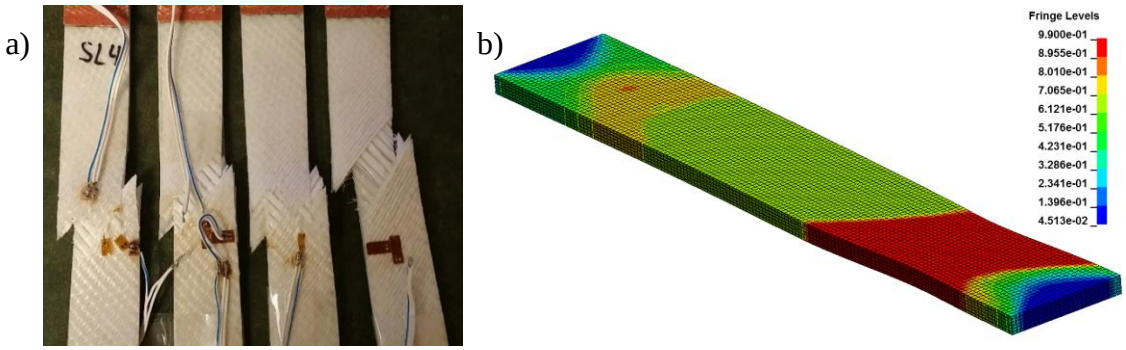

Figure 3.10: In-plane shear failure a) experimental and b) numerical results

Tensile tests were performed on $[\{-45/+45/-45\}]_{3s}$ specimens at 2, 100 and 500 mm/min crosshead displacement rates to assess the effect of strain rate on the shear behavior. As evidenced from Figure 3.11, increasing the strain rate yields increase shear modulus and strength. There is a debate in the literature regarding the effects of strain rate on the in-plane shear behavior. Hsiao et al.(1999) reported that the in-plane shear modulus and shear strength increase with increasing strain rate. However, Papadakis et al. (2004) revealed that the shear modulus decreased with increasing strain

rate, whereas shear strength increased. The viscoplastic model accurately reflected the effects of the strain rate on the in-plane shear stress.

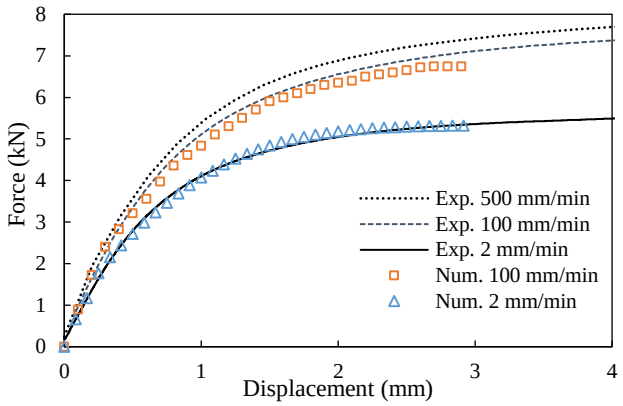

Figure 3.11: Tensile force versus displacement curves of $[\{-45/+45/-45\}]_{3s}$ under various strain rates

3.7.2 Impact simulation

3.7.2.1 Force-time and energy-time histories

The predicted impact force-time and energy-time are compared with the experimental results in Figure 3.12 and Figure 3.13 for four impact energy levels to assess the accuracy of the proposed material damage model to predict the impact resistance of the NCF laminates. These figures illustrate that the numerical results obtained with the viscoplastic-damage model correspond reasonably well with the experiments. The maximum relative errors between the predicted and experimental values of maximum contact load and absorbed energy are 5% and 10%, respectively.

At a lower impact energy level of 10 J, the contact force was slightly overestimated compared with the experimental data (see Figure 3.12a). The energy-time history indicates that the energy absorption was underestimated, which could be attributed to the less plastic deformation and damage prediction compared to the experiments. Furthermore, the numerical results indicate a slight decrease in the slope of the force-time curve at a load level approximately 2.4 kN. This decrease reflects a reduction in the laminate stiffness that is commonly associated with the occurrence of internal damage (e.g. matrix cracking and delamination). However, internal damage was not accompanied by a load drop in the force-time histories. The predicted force-time and

energy-time histories show better agreement with the experimental data for an impact energy of 20 J (see Figure 3.12b).

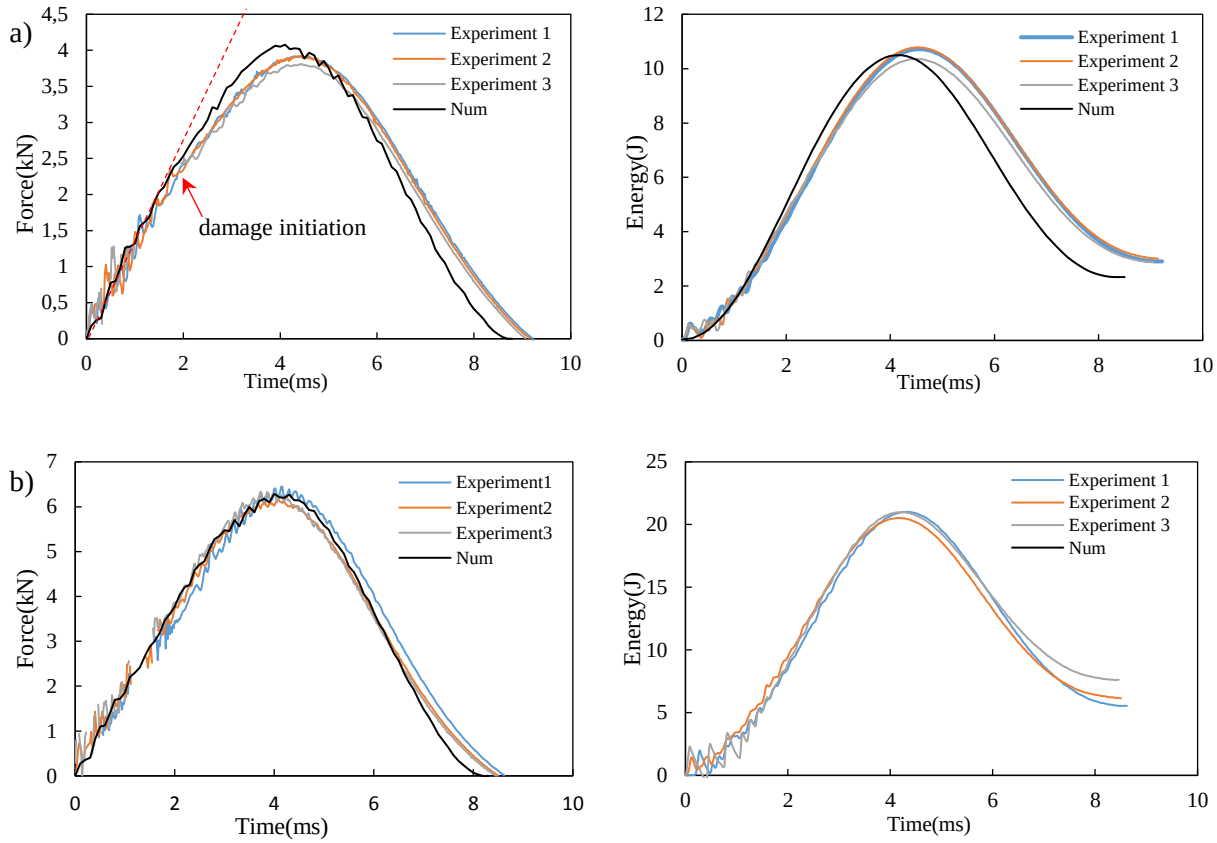

Figure 3.12: Impact response at impact energies of a) 10 J and b) 20 J

The predicted force-time curve corresponds well with the experimental curve up to the maximum contact force for an impact energy of 30 J; however, there exists a slight difference during the unloading stage, as shown in Figure 3.13a. For the experimental data, there is a slight drop in the contact force graph for all specimens after reaching the peak force. This load drop could be due to damage to fibers under tension, which is mainly caused by fiber pull-out. In-plane shear strain is the main cause of fiber pull-out in the bottom 0° ply (Wei et al., 2013). However, no evidence of fiber rupture was observed in the experiments for impact energy levels below 35 J. This phenomenon was not captured by the numerical damage model.

For an impact energy of 45 J, the contact force increases gradually up to a maximum force value and suddenly drops, accompanied by force oscillations. The contact force then slowly decreases during the unloading path. The load drop in the force-time curve was caused by the fiber rupture

due to high tension stresses. The numerical results reflected this feature well; nevertheless, the peak contact force was slightly overestimated by the numerical model compared with the experimental data. Interestingly, the energy absorption an under impact energy of 45 J is nearly two times greater than that with an impact energy of 30 J.

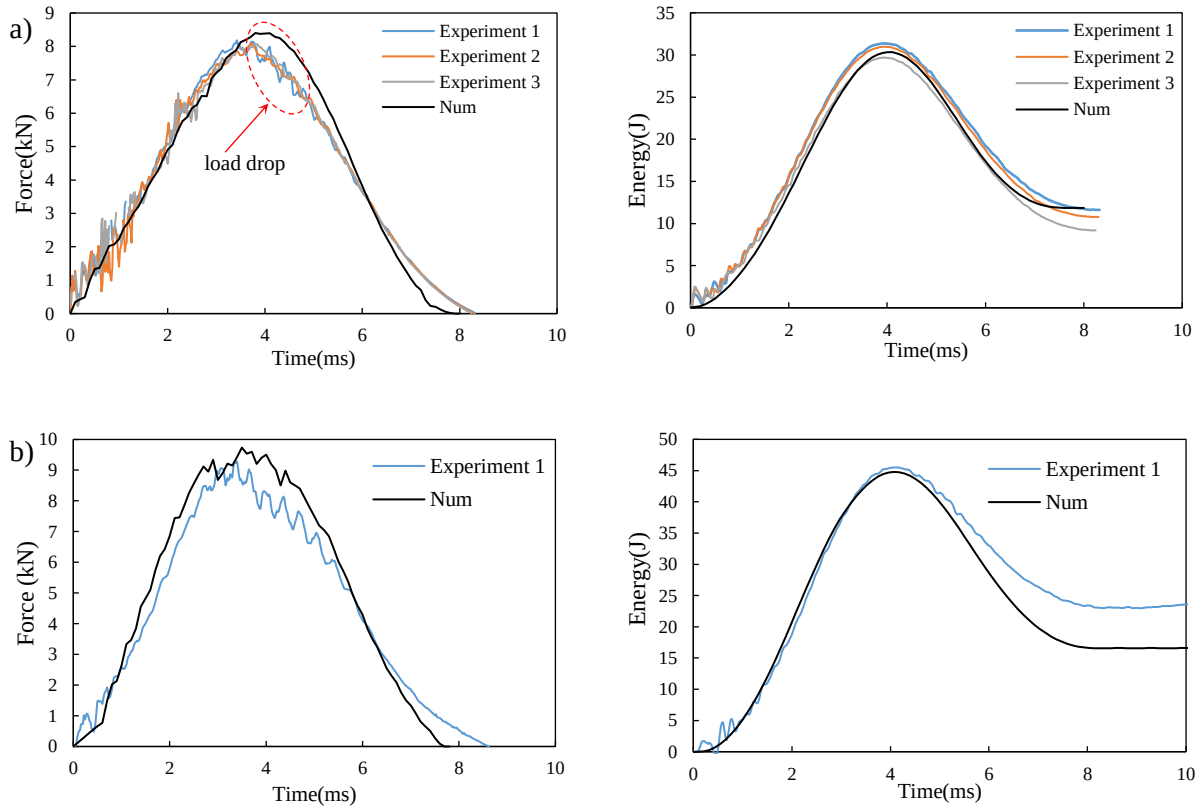

Figure 3.13: Impact response at impact energies of a) 30 J and b) 45 J

The maximum contact force and maximum absorbed energy as a function of impact energy are presented in Figure 3.14. Increasing the impact energy is accompanied by an increase in the maximum contact force up to approximately 9.5 kN, after which it remains nearly constant. As shown in the figure, the contact force did not increase as the impact energy increased from 45 J to 52 J, indicating the appearance of critical damage in NCF laminates. According to this figure, the critical damage appears for impact energies greater than approximately 35 J. Moreover, the appearance of critical damage associated with a jump in energy absorption trend, as shown in Figure 3.14.

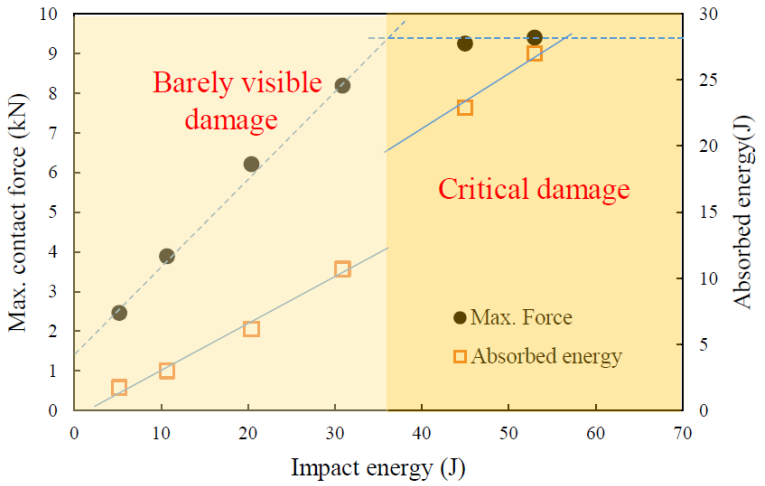

Figure 3.14: Maximum contact force versus initial impact energy

3.7.2.2 Impact-induced damage

A comparison between the predicted and measured impact damage area at various impact energies is shown in Figure 3.15. The damage area is defined here as the total projected damage area, which includes both the matrix cracks and delamination in all plies and interfaces, respectively. The comparison of the experimental data and simulation indicates rather good correlation in terms of damage pattern and size. Moreover, the impact-induced damage area for the impact energy of barely visible damage (impact energies below 35 J) is nearly circular in shape. However, the peanut shape of the damage area is more pronounced for impact energies greater than 35 J with critical damage, as shown in Figure 3.15. This phenomenon was successfully captured by the proposed impact damage model.

To obtain more information regarding the internal damage mechanisms induced during the impact events, specimens were sectioned at the impact point and then examined under an optical microscope with a ProgRes C14 digital camera. The optical micrographs obtained for specimens subjected to an impact energy of 30 J are shown in Figure 3.16. Detailed analysis of the damage zone shows that the matrix shear cracks in the upper plies are the first damage mode that appeared in the NCF laminates. The shear cracks are more frequent in impacted specimens than the bending cracks due to the high- thickness of the laminate. Once the shear cracks reach the interface, they propagate through the ply interfaces as delamination.

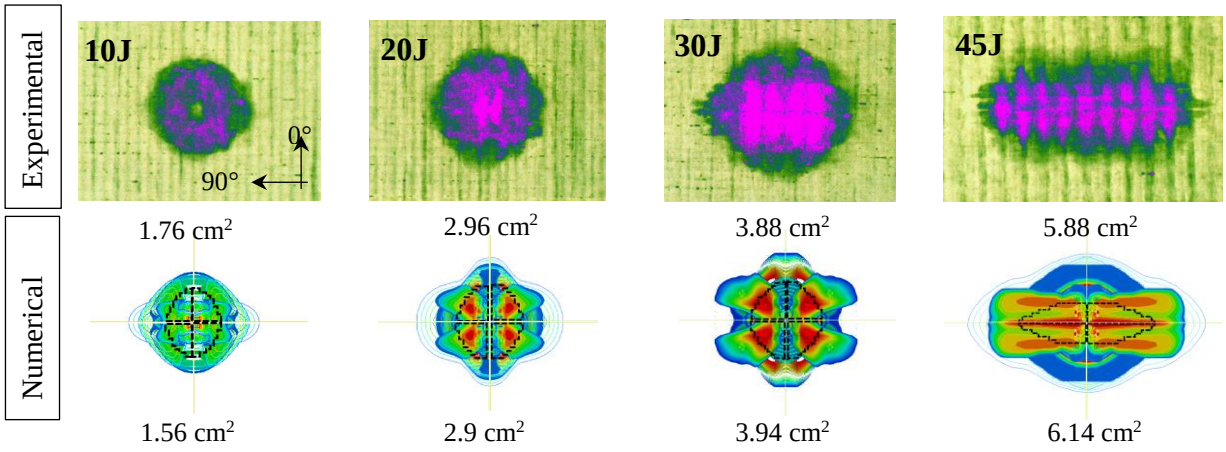

Figure 3.15: Impact damage area at various impact energies (the dashed line represents the delamination area)

Figure 3.16 illustrates that the delamination passes through the interface of two plies with different fiber-orientation angles. As noted above, each fabric layer of NCF laminate is composed of three plies {90°/0°/90°} and two adjacent layers have the same fiber-orientation angle of 90°. Thus, delamination did not form in the rich-resin area between adjacent layers. This finding supports the hypothesis that the bending stiffness mismatch is the main cause of delamination.

Moreover, the three components of the fabric layer are stitched together by polyester yarn. Nesting the plies with polyester yarn, which is specific to this NCF architecture, improves the inter-laminar fracture energy is. In fact, nesting the plies prevents them from opening and sliding, and consequently slows down the propagation of inter-laminar damage. Tan et al. (2012) investigated the effects of through-thickness stitching on the reduction of the impact-induced delamination area. They revealed that the delamination area could be reduced approximately 40% once the stitch fiber volume fraction V_{ft} reaches 0.4%. The stitch volume fraction can be evaluated using

$$V_{ft} = \frac{2S_{Area}}{S_P \times S_S} \times 100\% \tag{3-26}$$

where S_{Area} represents the stitch thread cross-sectional area and S_P and S_S are the stitch pitch and stitch space, respectively. The stitch volume fraction of NCF laminates is approximately 0.55%.

The effects of stitching was simulated by using higher values of fracture energies (G_{IC} and G_{IIC}) in the definition of cohesive elements.

Analysis of the experimental results also indicates that the delamination growth did not cause a load drop in the force-time curves. This feature could be attributed to the stable delamination growth during impact loading. Several researchers have reported that unstable delamination growth appears as an abrupt load drop in the force-time curve (Davies et al., 1995; Sankar et al., 1993).

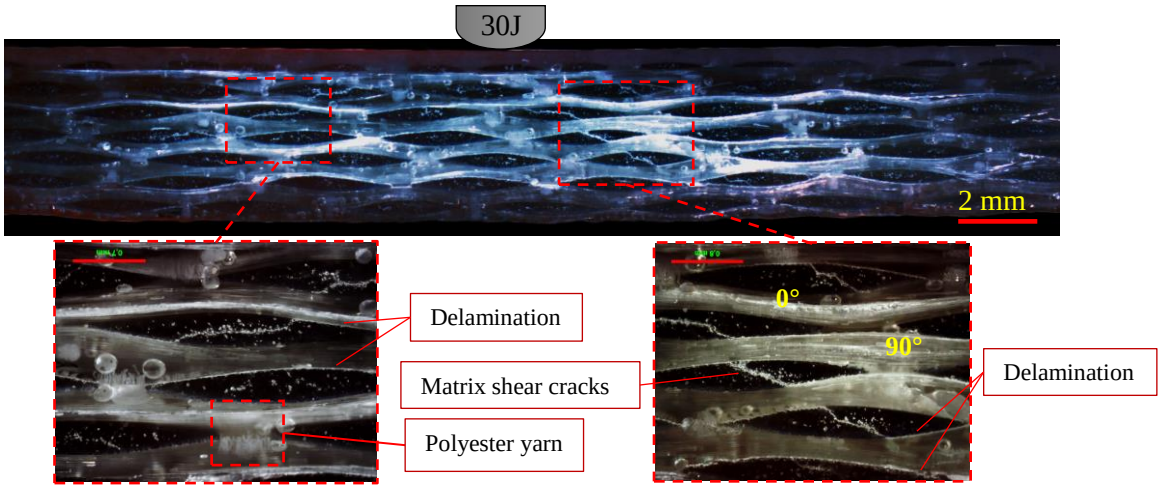

Figure 3.16: Interface delamination obtained by optical microscopy

Detailed observations of the specimens impacted at 45 J showed that the major fiber ruptures occur in the three bottom 0° plies, whereas the 90° plies seems to remain nearly intact, as shown in Figure 3.17. The numerical results indicate that the tensile stresses in the 0° plies due to the plate bending are slightly higher than those in the 90° plies. Moreover, the fiber bundles of 0° are 4 times larger than those of 90°, which seems to promote the fiber rupture in the 0° plies. The large fiber bundle size is generally weaker than the small fiber bundle size because of the formation of more intra-bundle voids in large fiber bundles (Wang et al., 2009). The numerical results well captured this fiber failure.

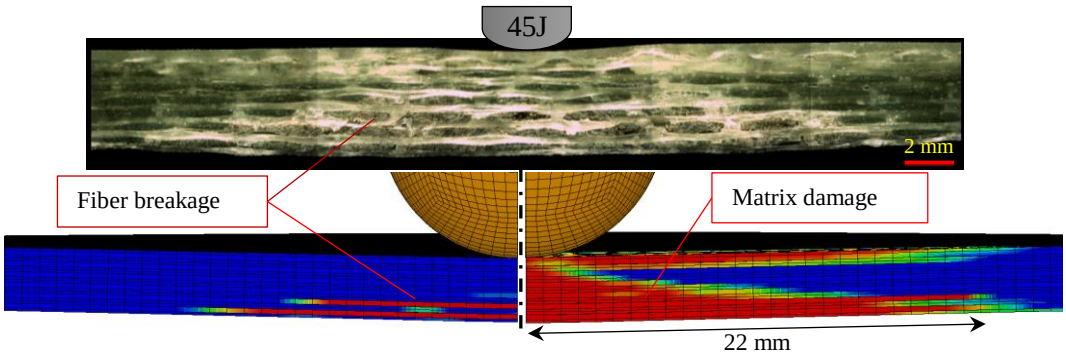

Figure 3.17: Cross-sectional view of the damage zone at an impact energy of 45 J

3.7.2.3 Effects of strain rate

The effects of strain rate on the mechanical behavior of glass laminates are demonstrated by comparing the impact and quasi-static loadings. The force-displacement curves of laminates under quasi-static loading rates of 2 and 100 mm/min are shown in Figure 3.18 along with curves obtained at impact energies of 30, 45 and 73 J. The experimental results show that the contact force linearly increases with increasing the impactor displacement up to a large deformation of 5 mm, under both quasi-static and impact loadings. In the linear section, the mechanical behavior of NCF laminates is not significantly affected by strain rate and the laminate stiffnesses are similar in both loading cases. After the linear section, the stiffness behavior under impact loading progressively increases due to the membrane effects which are engaged by large displacement in laminates. The increasing stiffness consequently leads to decrease in the impactor displacement and damage propagation. Contrary to the impact loading, the stiffness of laminate under quasi-static loading exhibits a significantly decreased resistance at higher displacement. It seems that applying constant displacement rate causes more damage progression, and the membrane effects on the stiffness are hence not manifest in this case. Furthermore, the experimental results indicate that increasing the strain rate has no discernable influences on the impact response of laminates even under large displacement. However, the large-displacement response of glass laminate and damage propagation are considerably affected by strain rate under quasi-static loading. The analysis of experimental data shows that increasing the strain rate is accompanied by the increasing recorded values of maximum sustained load. The obtained numerical results are also illustrated in Figure

3.18. The strain rate effects on the response of NCF laminates under quasi-static loading are reasonably predicted by the numerical model.

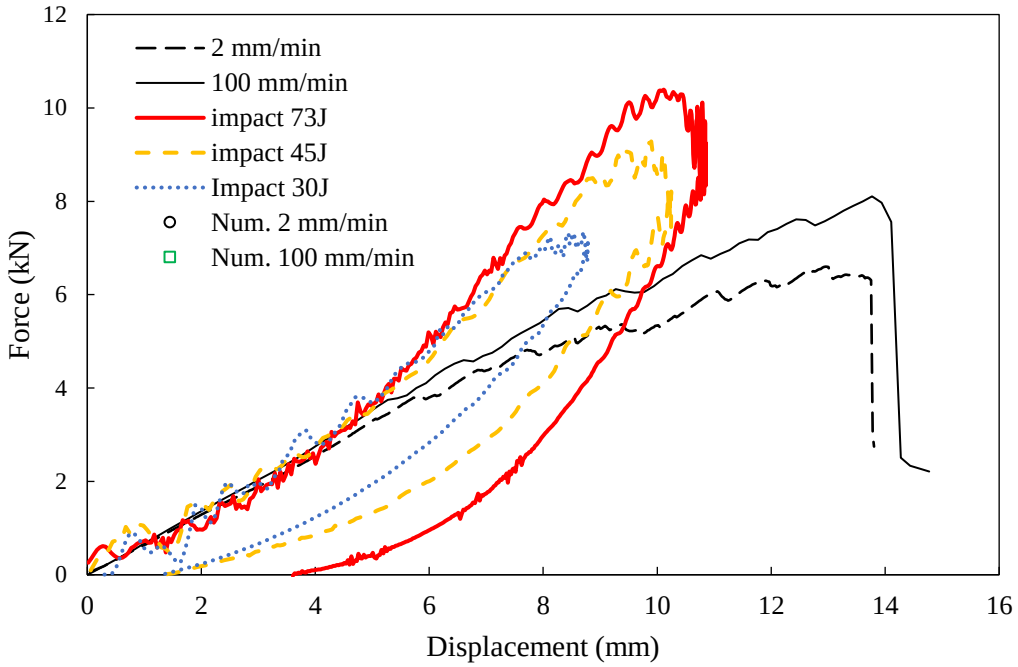

Figure 3.18: Force-displacement curves under quasi-static and dynamic loadings

3.8 Conclusions

Because of limitations shown by existing composite damage models, the shear-strain behavior of laminated composites has been modified by using a viscoplastic model in order to improve the prediction of plastic deformation, and shear stiffness degradation as well as to diminish computational efforts in comparison with existing models. A symmetric reversal loading was also considered in the model without any additional implementation efforts. This was attained without the need to perform cyclic shear tests like many available damage models, which give the present model significant simplicity and efficiency. The proposed material damage model was used for simulating low-velocity impact response of non-crimp fabric glass reinforced epoxy matrix-based composites with the sequence $[\{90°/0°/90°\}]_{3s}$. Impact tests were carried out under various impact energies ranging from 5 to 73 J using an instrumented drop-weight machine. The numerical results were in good agreement with experimental results.

It has been noted that the barely visible damage occurs in the laminated specimens for impact energies below 35 J. For impact energies above 35 J, the fiber breakage (critical damage) first appears in the bottom 0° plies which have larger fiber bundles in comparison with 90° plies. Microscopic analysis of delamination mechanisms in NCF laminated composite reveals that delamination does not propagate in the resin-rich area between fabric layers and it grows inside of fabric layers. It was also concluded that stitching the plies together with polyester yard promotes stable delamination growth and reduces the impact-induced delamination area.

Form the experimental results it is inferred that the large-displacement response of glass laminate under quasi-static tests is strain rate dependent, and the damage resistance of laminate is increased by increasing strain rate. However, the strain rate effects on the impact response are not significant based on the experimental and numerical finding. The numerical results also show that by considering the strain rate in nonlinear shear behavior, it is possible to reasonably predict the strain rate effects on the mechanical behavior of glass laminates.

Despite these promising results, further efforts are required to improve the effectiveness of the proposed material model in the simulation of the impact response of the NCF laminates. In fact, it would be interesting to include plastic deformation in the transverse direction to precisely predict the mechanical behavior of glass laminates.

CHAPTER 4 ARTICLE 2: LOW-VELOCITY IMPACT RESISTANCE OF ATH/EPOXY CORE SANDWICH COMPOSITE PANELS: EXPERIMENTAL AND NUMERICAL ANALYSES

G. Morada, R. Ouadday, A. Vadean, R. Boukhili (2017). Journal of Composites Part B: Engineering, 114, pp. 418-431.

4.1 Abstract

In this study, a new composite sandwich was investigated as a solution for the rehabilitation of existing hydraulic turbine. The innovative sandwich construction with an ATH/epoxy core (i.e. epoxy resin filled with alumina tri-hydrate (ATH) particles) and non-crimp glass fabric fiber-reinforced epoxy face sheets was subjected to low-velocity impact at various energy levels. A 3D progressive damage model was developed to predict the damage characteristics in the face sheets in combination with a viscoplastic-damage model to simulate the nonlinear response of the core. The obtained numerical results were compared with the test data to assess the effectiveness of the proposed model. Good correlation with respect to the contact force and energy-time relationships, permanent deformation, and impact-induced damage was achieved. The performance of the sandwich panel with an ATH/epoxy core was evaluated in term of impact damage resistance and energy dissipation capacity. Microscopic observations were performed to determine the damage and failure modes in the impact zone. The important role of the core material for enhancing the face-sheet damage tolerance was also identified. The various energy dissipation components were also quantified during an impact loading, and the energy dissipated in the sandwich core was approximately 50% of the initial impact energy.

4.2 Introduction

Composite sandwich structures are finding increasing utilization in many engineering applications such as aerospace, automotive, building, and water turbine industries, due to the benefits they can provide compared to other structural materials (Chai et al., 2011a). According to study of Bornard et al. (2014), rehabilitation of hydraulic turbine after years of operation could be performed by using an extension structure made of composite materials. The extension structure is attached to

existing stay vanes in hydraulic turbine. This innovative solution can enhance the turbine capacity, energy production and also facilitate on-site manufacturing. However, the river flow may contain a large amount of waterborne debris in such applications. The impact of this waterborne debris is known as the major source of damage for the composite hydraulic turbine blades. The impact resistance of composite structures is an important topic in engineering communities.

The impact resistance of a composite sandwich depends on the mechanical and geometrical properties of its constituents, such as the face sheet material, core material, and adhesive interface properties. The core material properties are the main parameters to be considered for improving the impact resistance of composite sandwich panels (Wang et al., 2016). The main function of the sandwich core is to absorb the impact energy and provide an overall bending resistance. Ivanez et al. (2010) reported that the compressive behavior of the core significantly affects the failure mode of foam core sandwich beams. Mines et al. (1998a) also revealed that the core density strongly affects the failure progression. They identified core crushing as the major failure mechanism of polymer composite sandwiches under impact events. Furthermore, absorbing impact energy via the plastic deformations of the core can improve the damage tolerance of the sandwich structures (Evans et al., 2010). Torre and Kenny (2000a) attempted to enhance the crush resistance in civil engineering structures using an innovative sandwich construction made of glass/phenolic composite skins and a rigid polymer foam core with fiber reinforced plastic. A wide variety of lightweight materials can be used as the core in sandwich construction, such as synthetic foam, honeycomb, balsa wood, and corrugated cores (Chai et al., 2011a; Wang et al., 2016). However, lightweight cores do not have sufficient resistance to withstand high- impact loads.

In light of the aforementioned considerations and the existence of some limitations on experimental tests (such as time-consuming manufacturing process and not providing critical information of stress/strain and energy partitions dissipated in the face sheets and core (Chai et al., 2011b), there is a strong need to develop a numerical model that can be used to predict the structural impact response and the damage process and locations under impact conditions. Several numerical approaches have been proposed in the literature to predict the response of sandwich structures under impact loads (Aktay et al., 2005; Feng et al., 2013; Foo et al., 2008; Zhou et al., 2012). Several researchers (Aktay et al., 2005; Foo et al., 2008; Zhou et al., 2012) have used 2D shell elements to model the face sheets to reduce the computational time. Among them, Zhou et al. (2012) studied the perforation resistance of foam-based sandwich panels using 2D elements for the

face sheets; however, these elements are not accurate for failure analysis because the stress distribution in the face sheets is a 3D problem. Feng et al. (2013) used a progressive damage model to simulate the damage scenarios in foam-based sandwich composites subjected to impact loads. In their proposed model, a 3D damage model was used to track the intra-laminar damages in face sheets along with cohesive elements to simulate interface delamination.

The mechanical response of a sandwich composites made with a high-density core (ATH/epoxy: epoxy resin filled with alumina trihydrate particles) and non-Crimp Fabric (NCF) glass/epoxy face sheets (see Figure 4.1) was investigated under low-velocity impact. To the best of the authors' knowledge, no published studies have considered this sandwich construction. The present study consists of the development of an explicit finite element model for detailed analysis of internal damage mechanisms in the sandwich panels. An intra-laminar damage model was implemented in LS-DYNA/Explicit code to simulate the damage initiation and development within the face sheets. The model includes an enhanced non-linear shear model and a mixed-matrix damage initiation and propagation law. Furthermore, a specific viscoplastic-damage model is developed to simulate the behavior of the ATH/epoxy core. The numerical results were compared with the experimental data in terms of the global structural response and internal damage characteristic. Once validated, the numerical model was used to assess the contribution of each component of the sandwich structure to its energy absorption capacity.

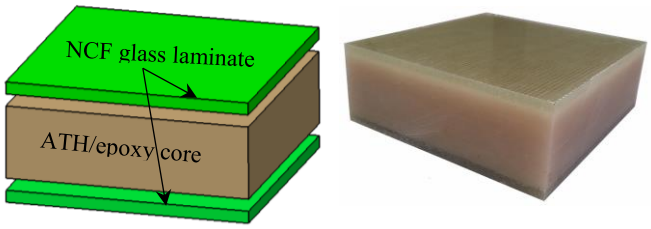

Figure 4.1: a) Schematic of the sandwich panel, b) panel test sample

4.3 Experimental tests

In this investigation, NCF glass- reinforced composite laminates are used as face sheets for sandwich panels. Compared to conventional reinforcements, NCF laminates offer relatively good mechanical properties, high deposition rate and low manufacturing costs. The thickness of this

fabric layer is normally twice that of a conventional layer, which facilitates a faster hand lay-up procedure. NCF laminates have been also proven to demonstrate higher out-of-plane fracture resistance and impact damage tolerance compare to UD prepreg (Tsai et al., 2005). The composite face sheets were composed of six layers of E-glass/epoxy reinforcement $[\{90°/0°/90°\}]_{3s}$. Each NCF fabric layer consists of three unidirectional plies of {90°/0°/90°} stitched together using polyester yarn. Individual fabric layers have a fiber volume fraction of 0.52 and a nominal thickness of 0.61 mm, giving a face sheet thickness of approximately 3.66 mm. The epoxy resin used in the sandwich manufacturing was Araldite® LY 8601 mixed with a hardener of Aradur® 8602 (mix weight ratio of 100:25) provided by Huntsman Advanced Materials Americas LLC. In order to fabricate the sandwich panels, the composite face sheets were first manufactured using the vacuum infusion (VI) process. Then, the sandwich core was prepared by mixing the epoxy resin with 60 wt% of ATH particles. The amount of ATH was gradually added to the epoxy resin and mixed for about 15 min at room temperature to achieve a uniform dispersion of ATH fillers throughout the epoxy resin. The polymerization mixture was poured into a wood mould in which the face sheets were earlier positioned at both of its ends, as shown in Figure 4.2a. The nominal thickness of the sandwich core is 27 mm. After the casting process was completed, the curing of the plastic core (ATH/epoxy) was achieved at room temperature for 24 h. Following the curing process, the sandwich panels were cut into specimens with dimensions of 100 mm × 100 mm.

4.3.1 Low-velocity impact tests

Impact tests were performed using a drop weight machine following the guideline given in the ASTM standard D3763 (2006). The low-velocity impact tests were executed on two types of specimens: 1) ATH/epoxy specimens and 2) sandwich specimens with an ATH/epoxy core. The impactor had a mass of 22 kg and a diameter of 25.4 mm. During the impact test, the specimen was constrained between two parallel rigid supports with a 75- mm- diameter hole in the center (see Figure 4.2b). Sufficient clamping pressure was applied to prevent the specimen from slipping during the experiments. At least three specimens were used to perform impact tests at various impact energies.

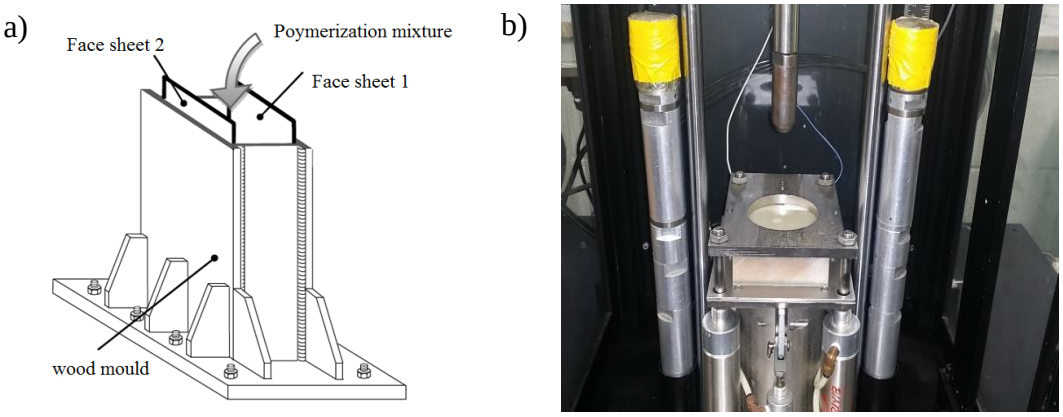

Figure 4.2: a) Wood mould for fabrication, b) Specimen fixture apparatus

After the impact, the type of damage in the face sheet and core was identified via destructive inspection. The impacted specimen was cut through the center of the impacted zone. Then, it was polished to such a degree that the damage zone could be evaluated using an optical microscope.

4.3.2 Compression test on ATH/epoxy

Rigid fillers, such as ATH, are mixed with epoxy resin to improve a particular property and lower the manufacturing cost (Phipps et al., 1995). The presence of ATH particles in the epoxy resin also decreases the cure exotherm of epoxy and increases its viscosity. In this study, ATH particles were added to the epoxy resin at 60% wt. in order to control the heat generated by the exothermic reactions, otherwise the entire sandwich structure may collapse during the curing process. This amount of ATH was selected based on a preliminary experimental study (not reported herein), which was conducted earlier to identify the optimum ATH amount that can be used to minimize the heat generated during the epoxy curing reaction. Also, the use of the same epoxy for the core and face sheets favors a good adhesion between the face sheets and core.

Flatwise compression and three-point flexural tests were performed in order to characterize the ATH/epoxy material. Flatwise compression tests were conducted under displacement control condition with loading-unloading hysteresis cycles at room temperature. Square cross-section specimens with dimensions of 51 × 51 mm^2 and a thickness of 25.4 mm were prepared according to the ASTM D1621-10 standard procedure (2010). Testing was carried out on the MTS testing machine with a displacement rate of 2.5 mm/min. The uniform distributed load was applied on

specimens by two flat and parallel plates. The force-displacement curves of ATH/epoxy under uniaxial compressive loading and unloading are shown in Figure 4.3a. The obtained results show that the response of ATH/epoxy under uniaxial compressive loading is nonlinear, with a significant irreversible plastic deformation under unloading.

Three-point bending tests were carried out on ATH/epoxy specimens according to ASTM D790. The specimens had dimensions of 100×12.7×5 mm^3 and the loading span was set to be 60 mm. The flexural response of ATH/epoxy and neat epoxy are shown in Figure 4.3b. The results reveal that the flexural response of ATH/epoxy is linear up to brittle failure, while the neat epoxy exhibits a nonlinear response with a large failure strain.

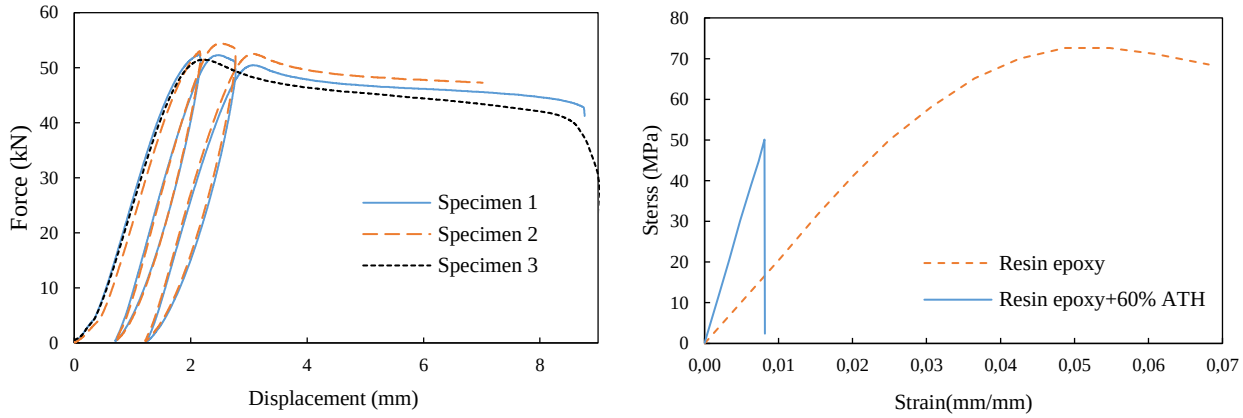

Figure 4.3: a) Force-displacement curves of ATH/epoxy under compressive loading and unloading and b) Flexural behavior of ATH/epoxy and neat epoxy

4.4 Finite element model

A 3D finite element model was implemented in LS-DYNA/Explicit code to predict the mechanical behavior of the entire sandwich panels and the damage characteristics for the core and face-sheets during impact loading. Two finite element models were used in this numerical study to simulate the impact response of the ATH/epoxy specimen and the sandwich panel specimen, as illustrated in Figure 4.4. Only one quarter of the sandwich panel with symmetric boundary conditions was modeled to decrease the computational time.

Both the face sheets and plastic core were modeled using eight-node solid elements with reduced integration and hourglass control. Delamination between adjacent plies with different fiber

orientations and face/core interface debonding were modeled with zero-thickness cohesive elements. The impactor and support plate were defined as rigid bodies. A surface-to-surface type of contact element was defined between the upper face sheet and impactor surface. A friction coefficient of 0.3 (Faggiani et al., 2010) was defined between the impactor and face sheet, and ply-to-ply interface contact. Because no damage was observed in the bottom face sheet in the experimental testing, the face sheet damage model was defined for only the upper face sheet. The ATH/epoxy core behavior was simulated using the core material model described in the following section.

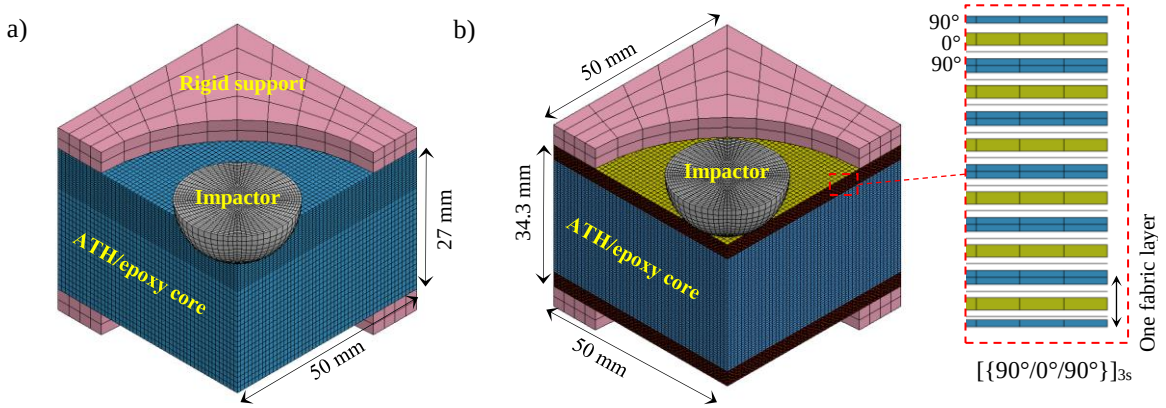

Figure 4.4: Finite element model for impact analyses: a) ATH/epoxy specimen b) sandwich specimen

4.4.1 Modeling of ATH/epoxy

4.4.1.1 Viscoplastic-damage model for the ATH/epoxy

ATH/epoxy polymer exhibits nonlinear stress-strain behavior during loading and produces substantial irreversible deformation upon unloading. The nonlinear behavior of the polymer and the strain rate dependence were assumed to be caused by inelastic strain, which is present for all stress components. A viscoplastic-damage model was developed to describe the behavior of ATH/epoxy under compression and tensile loading. The stress-strain relationship used to define the polymer behavior in compression is shown in Figure 4.5a. The compression response is characterized as linearly elastic up to the yield point σ_{cy}. Beyond the yield point, the polymer shows a plastic response until the ultimate stress σ_{cu}, followed by strain softening. Finally, the polymer

exhibits residual stress. If the polymer experiences unloading, which generally occurs during impact tests, the response will obey the linear-elastic unloading path. Once the stress becomes zero at the end of unloading, a residual irreversible strain will remain in the polymer.

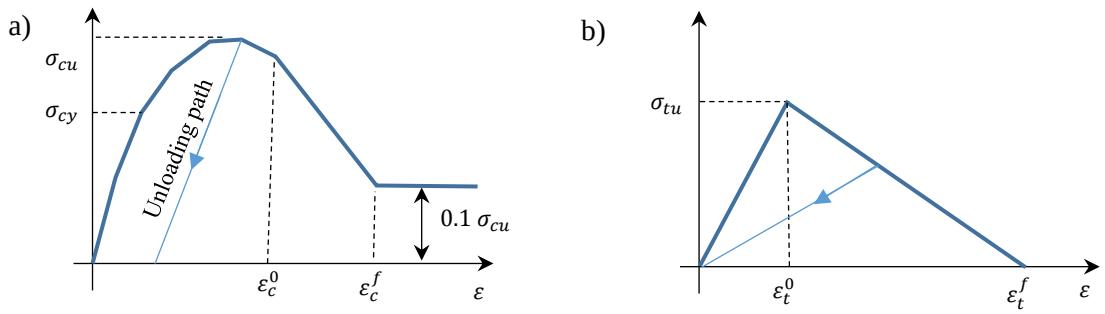

Figure 4.5: Stress-strain response of the ATH/epoxy core a) compression b) tension

The tension behavior is defined as linearly elastic until the failure stress σ_{tu} and is followed by stiffness degradation due to the presence of micro-cracks, which results in strain localization in the polymer (Figure 4.5b). The following constitutive law was used to define the behavior of ATH/epoxy.

$$\sigma_{ij} = [C_c]\left(\{\varepsilon_{ij}\} - \{\varepsilon_{ij}^I\}\right) \tag{4-1}$$

$$[C_c] = \begin{bmatrix} C_{11}^c & C_{12}^c & C_{12}^c & & & \\ & C_{11}^c & C_{12}^c & & 0 & \\ & & C_{11}^c & & & \\ & & & C_{44}^c & & \\ & Symm. & & & C_{44}^c & \\ & & & & & C_{44}^c \end{bmatrix}$$

where $C_{11}^c = \frac{E_c(1-\nu_c)}{(1+\nu_c)(1-2\nu_c)}$, $C_{12}^c = \frac{E_c\nu_c}{(1+\nu_c)(1-2\nu_c)}$ and $C_{44}^c = \frac{E_c}{2(1+\nu_c)}$. E_c and ν_c are Young's modulus and Poisson's ratio of the polymer, respectively. ε_{ij}^I is the plastic strain and is estimated in the following section. After the onset of damage, the elastic modulus is replaced by an effective modulus E_{eff} as:

$$E_{eff} = (1 - d_c)E_c \tag{4-2}$$

where d_c is a damage variable that takes a value between zero and one.

4.4.1.2 Polymer plasticity

Goldberg et al. (1999) proposed a viscoplastic model to describe the response of pure polymers. In our case, the Goldberg model was adopted to estimate the plastic strain in the ATH/epoxy. The onset of plastic deformation was defined by using the Bodner-Partom model (2001). According to the Bodner-Partom model, the inelastic strain rate tensor ($\dot{\varepsilon}_{ij}^{I}$) is proportional to the components of the deviatoric stress (S_{ij}):

$$\dot{\varepsilon}_{ij}^{I} = D_0 exp\left[-\frac{1}{2}\left(\frac{Z}{\sigma_e}\right)^{2n}\right]\frac{S_{ij}}{\sqrt{J}} \tag{4-3}$$

where D_0 and n are material constants. The rate-dependent plasticity decreases with increases in the value of n. The effective stress σ_e can be defined as

$$\sigma_e = \sqrt{3J} \tag{4-4}$$

where J denotes the second invariant of the deviatoric stress tensor. The following equation defines the evolution rate of the internal stress variable Z:

$$\dot{Z} = q(Z_1 - Z)\dot{e}_e^I \tag{4-5}$$

where q is related to the hardening rate and Z_1 represents the maximum value of Z. The initial value of Z is defined by the material constant Z_0. The initial value of Z (Z_0) affects the onset of nonlinearity, with greater value of Z_0 resulting in a stiffer material. The maximum value of Z (Z_1) controls the maximum stress. Finally, the effective deviatoric inelastic strain rate (the term $\dot{e}_e^I$ in Eq. (4-4)) is defined as follows:

$$\dot{e}_e^I = \sqrt{2/3\dot{e}_{ij}^I\dot{e}_{ij}^I} \tag{4-6}$$

$$\dot{e}_{ij}^I = \dot{\varepsilon}_{ij}^I - \frac{\dot{\varepsilon}_{kk}^I}{3}\delta_{ij}$$

The material constants n, Z_0, Z_1 and q can be obtained from a shear test. The procedure to select these parameters is thoroughly explained in the work of Goldberg et al. (1999). The parameter D_0

was assumed to be 10^4 times the maximum applied strain rate which means that it is approximately equal to 10^6 s^{-1}.

4.4.2 Face sheet damage model

4.4.2.1 Material constitutive model and nonlinear shear response

Composite materials commonly exhibit non-linear behavior due to plastic deformation and damage propagation in the matrix (Donadon et al., 2008). The intra-laminar constitutive behavior was described using the continuum damage mechanics in combination with plasticity theory to account for damage propagation and plastic deformation in laminated composites. According to experimental results, plastic deformation is more pronounced in the shear behavior. Thus, the elastic Hooke's law for linear orthotropic materials was reformulated to account for the matrix nonlinear shear response:

$$\begin{bmatrix}\sigma_{11}\\ \sigma_{22}\\ \sigma_{33}\end{bmatrix} = \frac{1}{\Omega}\begin{bmatrix} E_{11}(1-v_{23}v_{32}) & E_{22}(v_{12}-v_{32}v_{13}) & E_{33}(v_{13}-v_{12}v_{23}) \\ E_{11}(v_{21}-v_{31}v_{23}) & E_{22}(1-v_{13}v_{31}) & E_{33}(v_{23}-v_{21}v_{13}) \\ E_{11}(v_{31}-v_{21}v_{31}) & E_{22}(v_{32}-v_{12}v_{31}) & E_{33}(1-v_{12}v_{21}) \end{bmatrix}\begin{bmatrix}\varepsilon_{11}\\ \varepsilon_{22}\\ \varepsilon_{33}\end{bmatrix} \quad (4\text{-}7)$$

$$\Omega = 1 - v_{12}v_{21} - v_{23}v_{32} - v_{31}v_{13} - 2v_{21}v_{32}v_{13}$$

The nonlinear shear stress-strain part of the constitutive model was assigned as:

$$\tau_{ij} = G_{ij}\left(\gamma_{ij} - \gamma_{ij}^{in}\right)\left(1 - \alpha\gamma_{ij}\right) \ , \qquad i \ and \ j = 1,2,3 \quad (4\text{-}8)$$

where γ_{ij} is the total shear strain and can be decomposed into elastic γ_{ij}^{e} and inelastic γ_{ij}^{in} components:

$$\gamma_{ij} = \gamma_{ij}^{e} + \gamma_{ij}^{in} \quad (4\text{-}9)$$

Before damage initiation, inelastic component of the strain can be obtained by:

$$\gamma_{ij}^{in} = \gamma_{ij} - \frac{\tau_{ij}}{G_{ij}^{0}} - \frac{\tau_{ij}}{G_{ij}^{0}(1-\alpha\gamma_{ij})} \quad (4\text{-}10)$$

where G_{ij}^{0} is the initial shear modulus and α is a material constant expressing the gradual shear modulus, which can be determined experimentally (see Figure 4.6). A polynomial cubic stress-strain was used to explain the nonlinear behavior in shearing (Eq.(4-10)):

$$\tau_{ij}(\gamma_{ij}) = c_1\gamma_{ij} - sgn(\gamma_{ij})c_2\gamma_{ij}^2 + c_3\gamma_{ij}^3 \qquad (4\text{-}11)$$

where c_1, c_2 and c_3 are the coefficients obtained by curve fitting the experimental shear-strain behavior.

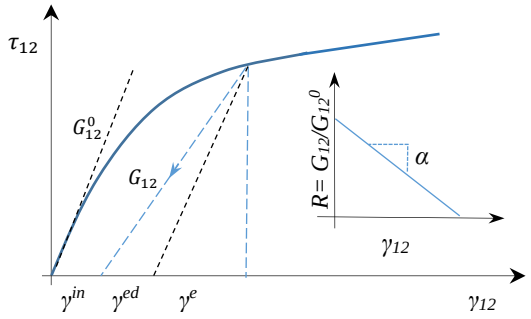

Figure 4.6: Shear-strain response implemented in the intra-laminar damage model

Damage initiation and propagation in the constitutive material were considered via continuum damage mechanic theory. The intra-laminar damage evolution was defined using two internal damage variables d_f and d_m corresponding to fiber damage and matrix damage respectively. Once fiber damage initiates, the undamaged longitudinal stress σ_{11} is degraded by the damage variable d_f, as shown in following equation. After matrix damage onset, the stress components are first rotated into the potential fracture plane ($\sigma_{123} \xrightarrow{\theta} \sigma_{ntl}$, θ is the angle of fracture plane). Then, the rotated stress components are reduced by the damage variable d_m ($\sigma_{ntl} \xrightarrow{dm} \sigma_{ntl}^{d}$) and finally transformed back into the original plane ($\sigma_{ntl}^{d} \xrightarrow{\theta} \bar{\sigma}_{123}^{d}$).

$$\sigma^d = \begin{Bmatrix} \sigma_{11}(1-d_f) \\ \bar{\sigma}_{22}^d \\ \bar{\sigma}_{33}^d \\ \bar{\tau}_{12}^d \\ \bar{\tau}_{23}^d \\ \bar{\tau}_{31}^d \end{Bmatrix}, (\sigma_{123} \xrightarrow{\theta} \sigma_{ntl} \xrightarrow{dm} \sigma_{ntl}^d \xrightarrow{\theta} \bar{\sigma}_{123}^d) \tag{4-12}$$

4.4.2.2 Fiber failure modes

Two strain-based failure criteria were used to detect fiber damage initiation under tensile and compressive loading:

$$F_{11}^T = \left(\frac{\varepsilon_{11}}{\varepsilon_{11}^{ot}}\right)^2 - 1 \geq 0 \tag{4-13}$$

$$F_{11}^C = \left(\frac{\varepsilon_{11}}{\varepsilon_{11}^{oc}}\right)^2 - 1 \geq 0$$

where ε_{11}^{ot} and ε_{11}^{oc} are the damage initiation strain in tension and compression respectively. After the damage initiates, the material starts to gradually lose its stiffness up to final failure, as shown in Figure 4.7. The damage variables for tensile and compressive fiber failure are defined via the following equations:

$$d_{11}^t = \frac{\varepsilon_{11}^{ft}}{\varepsilon_{11}^{ft} - \varepsilon_{11}^{ot}}\left(1 - \frac{\varepsilon_{11}^{ot}}{\varepsilon_{11}}\right)^2 \tag{4-14}$$

$$d_{11}^c = \frac{\varepsilon_{11}^{fc}}{\varepsilon_{11}^{fc} - \varepsilon_{11}^{oc}}\left(1 - \frac{\varepsilon_{11}^{oc}}{\varepsilon_{11}}\right)^2$$

where ε_{11}^{ft} and ε_{11}^{fc} are the maximum strains at failure, which were calculated from the critical energy release rate (G_{11}^t and G_{11}^c), maximum longitudinal stress (X^t, X^c) and characteristic length l_f:

$$\varepsilon_{11}^{ft} = \frac{2G_{11}^t}{X^t\, l_f}\ ;\ \ \varepsilon_{11}^{fc} = \frac{2G_{11}^c}{X^c\, l_f} \tag{4-15}$$

In this model, one coupled tension-compression damage variable d_f was used to simulate fiber degradation in the longitudinal direction, which was defined as follows:

$$d_f = d_{11}^c + d_{11}^t - d_{11}^t d_{11}^c \tag{4-16}$$

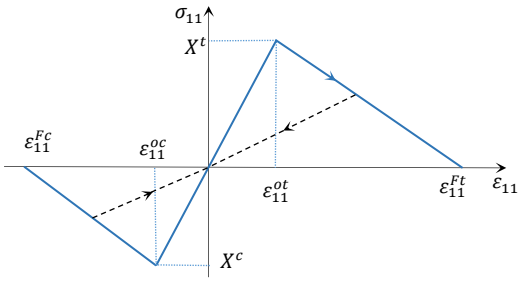

Figure 4.7: Intra-laminar damage model behavior for fiber failure

4.4.2.3 Matrix failure modes

Matrix damage initiation: The failure criteria proposed by Catalanotti et al. (2013) were used to detect matrix cracking. Accordingly, Puck failure criteria (1998) were employed to identify the matrix crushing as follows:

$$F_{22}^C = \left(\frac{\tau_{\mathrm{nl}}}{S_{\mathrm{l}}^{is} - \mu_{\mathrm{nt}}\sigma_{\mathrm{nn}}}\right)^2 + \left(\frac{\tau_{\mathrm{nt}}}{S_{\mathrm{t}}^{is} - \mu_{\mathrm{nl}}\sigma_{\mathrm{nn}}}\right)^2 - 1 \geq 0 \tag{4-17}$$

$$F_{22}^T = \left(\frac{\sigma_{\mathrm{nn}}}{S_{\mathrm{t}}^{is}}\right)^2 + \left(\frac{\tau_{\mathrm{nl}}}{S_{\mathrm{l}}^{is}}\right)^2 + \left(\frac{\tau_{\mathrm{nt}}}{S_{\mathrm{t}}^{is}}\right)^2 + \lambda\left(\frac{\sigma_{\mathrm{nn}}}{S_{\mathrm{t}}^{is}}\right)^2\left(\frac{\tau_{\mathrm{nl}}}{S_{\mathrm{l}}^{is}}\right)^2 + \kappa\left(\frac{\sigma_{\mathrm{nn}}}{S_{\mathrm{t}}^{is}}\right)^2 - 1 \geq 0$$

where κ and λ were calculated using $\kappa = \left(S_l^{in^2} - Y_t^{is}\right)/S_t^{is}\,Y_t^{is}$ and $\lambda = 2\mu_{nl}S_t^{is}/S_l^{is} - \kappa$. Additionally, Y_t^{is}, S_t^{is} and S_l^{is} are in- situ matrix tensile strength and shear strength in the transverse and longitudinal directions, respectively. Based on Mohr-Coulomb theory, the friction coefficients are defined as $\mu_{nt} = -1/\tan(2\theta_f)$ and $\mu_{nl} = \mu_{nt}\,S_l^{is}/S_{\mathrm{t}}^{is}$, where $S_{\mathrm{t}}^{is} = Y_{\mathrm{c}}^{is}/2\tan(\theta_f)$ and Y_{c}^{is} are the in- situ matrix compressive strengths. In our case, the maximum ply thickness in the simulation

is approximately 0.29 mm; thus, the in- situ strength values were calculated using the thin ply equation given by Pinho et al. (2012).

The angle of the fracture plane θ_f is approximately 53° for a unidirectional laminate under pure compressive loading. The two criteria depend on the stresses in the potential fracture plane which can be calculated using the standard transformation matrix $T(\theta)$:

$$\sigma_{nlt} = [T(\theta)]\sigma_{123}[T(\theta)]^T \tag{4-18}$$

The potential fracture plane is shown in Figure 4.8, which is parallel with the longitudinal axis and makes an angle of θ with the vertical axis. The orientation of the fracture plane was found via an iterative procedure for each element.

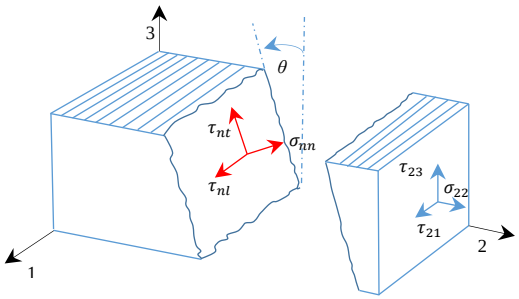

Figure 4.8: Potential fracture plane under compression loading

Matrix damage propagation: When the matrix failure onsets under combined stress, the equivalent stress σ_r and relevant strain ε_r on the potential fracture plane should be recorded.

$$\sigma_r = \sqrt{\langle\sigma_{nn}\rangle^2 + (\tau_{nt})^2 + (\tau_{nl})^2} \tag{4-19}$$

$$\varepsilon_r = \sqrt{\langle\varepsilon_{nn}\rangle^2 + (\gamma_{nt})^2 + (\gamma_{nl})^2}$$

$$\varepsilon^0_{\mathrm{r,in}} = \sqrt{(\gamma^{in}_{nt})^2 + (\gamma^{in}_{nl})^2}$$

In Eq. (4-18), $\varepsilon^0_{\mathrm{r,in}}$ is the inelastic component of strain at the moment of initiation, and $\langle\,\rangle$ is the Macaulay bracket. Furthermore, the total strain energy G_r before damage onset, must be recorded. The total strain energy was defined as a quadratic combination of the volumetric strain energies related to each stress component acting on the fracture plane.

$$G_r = G_{nn}\left(\frac{\langle\sigma_{nn}\rangle}{\sigma_r}\right)^2 + G_{nt}\left(\frac{\tau_{nt}}{\sigma_r}\right)^2 + G_{nl}\left(\frac{\tau_{nl}}{\sigma_r}\right)^2 \tag{4-20}$$

The volumetric strain energy of each stress component can be estimated using

$$G_i = \int_0^{\varepsilon_r} \sigma_i d\varepsilon_i \qquad i = nn\,, nt\,, nl \tag{4-21}$$

Then, the unified matrix damage variable d_m , which is used to soften the stress components acting on the fracture plane, is given by

$$d_m = \frac{\varepsilon_{\mathrm{r}}^f - \varepsilon_{\mathrm{r,in}}^0}{\varepsilon_{\mathrm{r}}^f - \varepsilon_{\mathrm{r}}^o}\left(\frac{\varepsilon_{\mathrm{r}}^0 - \varepsilon_r}{\varepsilon_r - \varepsilon_{\mathrm{r,in}}^0}\right) \tag{4-22}$$

where $\varepsilon_{\mathrm{r}}^f$ represents the final failure strain, which is calculated from the critical strain energy release rate and characteristic length as follows:

$$\varepsilon_r^f - \varepsilon_r = \frac{2G_m}{\sigma_r l_m} - \frac{2G_r}{\sigma_r} \tag{4-23}$$

The fracture energy for mixed-mode matrix failure under combined stresses can be computed by the following expression:

$$G_m = G_{IC}\left(\frac{\langle\sigma_{nn}\rangle}{\sigma_r}\right)^2 + G_{IIc}\left(\frac{\tau_{nt}}{\sigma_r}\right)^2 + G_{IIC}\left(\frac{\tau_{nl}}{\sigma_r}\right)^2 \tag{4-24}$$

where G_{IC} and G_{IIC} are the critical strain energy release rates for modes I and II, respectively. Finally, the shear stresses and tensile stress on the fracture plane are updated by the following relations, and then, the updated stresses are transformed back into the original plane.

$$\sigma_{nl} = (1 - d_m)\sigma_{nl} \tag{4-25}$$

$$\sigma_{nt} = (1 - d_m)\sigma_{nt}$$

$$\sigma_{nn} = \sigma_{nn} - d_m\langle\,\sigma_{nn}\rangle$$

Details on the computation of the characteristic element lengths l_f and l_m can be found in (Donadon et al., 2008; Falzon et al., 2011).

4.4.3 Material properties for the model

The elastic and strength properties were obtained for the NCF glass/epoxy laminate, form a series of experimental tests (tensile, compressive and shear tests) conducted by our group. Tensile tests were carried out on $[\{90°/0°/90°\}]_{3s}$ and $[\{-45°/+45°/-45°\}]_{3s}$ specimens according to ASTM D3039M (2003), while compressive tests were performed on $[\{90°/0°/90°\}]_{3s}$ specimens following the modified ASTM D695 standard with a gauge length of 4.8 mm. The mechanical properties of the face sheet are summarized in Table 4.1. The fiber fracture energies (G_{ft} and G_{fc}) were gathered from experimental measurements provided by Roy et al. (2001). The critical strain energy release rates (G_{IC} and G_{IIC}) evaluated for a unidirectional E-glass/epoxy (Compston et al., 1998) were used as input data to the model due to lack of experimental data for NCF laminated composite. The initial stiffness values of the cohesive interface were estimated as $k_N=50E_{33}/t$ and $k_S=50G_{12}/t$ (2007), whereas the cohesive strengths S and N were assumed to be matrix dominated properties, and thus $N=Y_t$ and $S=S_{12}$. The selected material properties were verified through comparing numerical results of the tensile, compressive and shear tests with the experiments.

Table 4.1: Material properties of an E-glass fiber/epoxy NCF laminate

Property	Values
Elastic properties	E_{11} = 34.4 GPa; E_{22} = E_{33} = 6.98 GPa; ν_{12} = ν_{13} = 0.28; ν_{23} =0.5 ;
Strength	X_t = 1100 MPa; X_c = 780 MPa; Y_t = 45 MPa; Y_c = 120 MPa;
Fracture toughness	G_{ft} = G_{fc} =35000 J/m²; G_{Ic} = 800 J/m²; G_{IIc} = G_{IIIc} = 1200 J/m² ;
Interface properties	k_N = 120 GPa/mm; k_s = 48 GPa/mm; N = 30 MPa; S = 45 MPa; η = 1.4;

The elastic properties of ATH/epoxy were obtained from flatwise compression tests. The material constants of n, Z_0, Z_1 and q were calculated using the procedure described by Goldberg et al. (2005). The values of all the parameters defining the constitutive behavior of the core are presented in Table 4.2.

Table 4.2: Material constants of ATH/epoxy resin

Modulus(GPa)	Poisson's ratio	n	Z_0 (MPa)	Z_1(MPa)	q	$D_0(s^{-1})$
6.13	0.3	0.93	396	753.82	279.26	10^6

4.4.4 Mesh sensitivity analysis

The in-plane size of elements in the impact zone was determined on the basis of a mesh sensitivity analysis. One element was employed in the through-thickness direction to represent each discrete ply of the face sheet and the thickness of core elements was fixed to be 0.5 mm. Three in-plane element sizes of 1.5×1.5, 1×1 and 0.5×0.5 mm^2 were examined. Impact simulations for the mesh convergence were executed with 40 J of impact energy. The force-time and energy-time curves are shown in Figure 4.9 for the three element sizes. The results show that the force and energy curves were sufficiently converged when applying element size less than approx. 1 mm. The in-plane size of element was chosen to be 1mm×1mm for reducing the computational time.

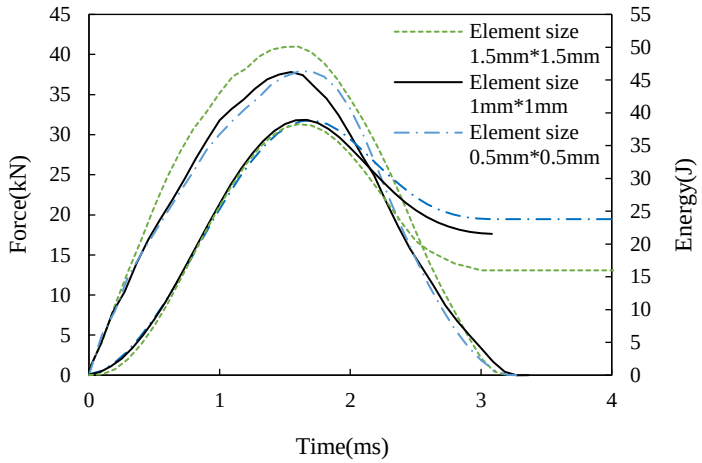

Figure 4.9: Force-time and energy-time curves in terms of the in-plane size of elements

4.5 Results and discussion

4.5.1 Impact response of ATH/epoxy specimens

4.5.1.1 Experimental results

The contact force-time and energy-time curves of ATH/epoxy specimens subjected to various impact energies up to 50 J are shown in Figure 4.10a and b. The overall trends of the curves are similar for all impact energies. Detailed analysis of each force-time curve shows that the contact force increases gradually up to the peak force in the loading path and then, decreases more rapidly in the rebounding path.

Analysis of the obtained test results shows that the peak impact force increases linearly with increasing impact energy, whereas the contact duration remains nearly constant. Increasing the impact energy is also accompanied by a linear increase in the energy absorption. Moreover, a considerable amount of the initial impact energy, approximately 70%, was dissipated by the ATH/epoxy during an impact event.

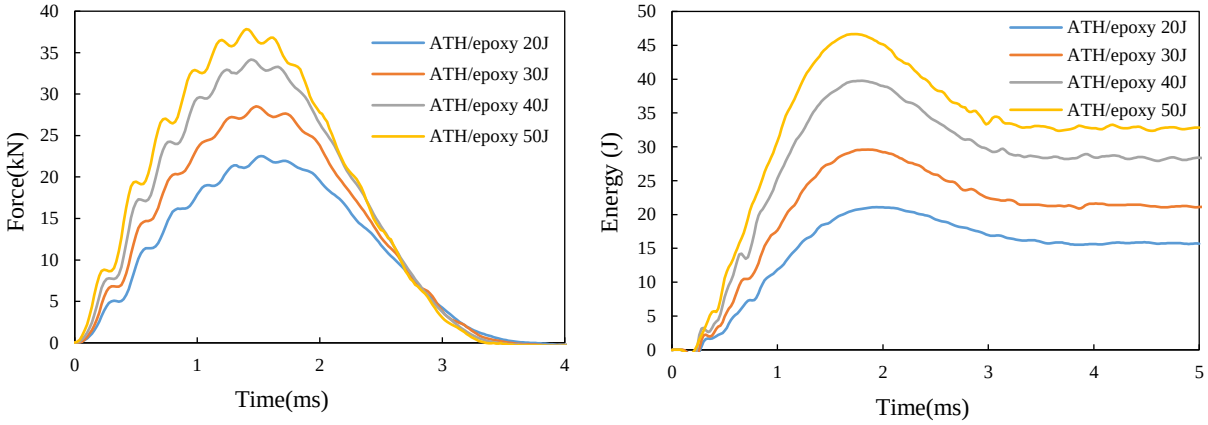

Figure 4.10: Impact response of ATH/epoxy specimens at various impact energies

The damage extension of ATH/epoxy specimens under various impact energies is illustrated in Figure 4.11. The light area represents the damage zone in impacted specimens. As can be observed, the damage area is approximately circular in shape and increases slightly with an increase in the impact energy.

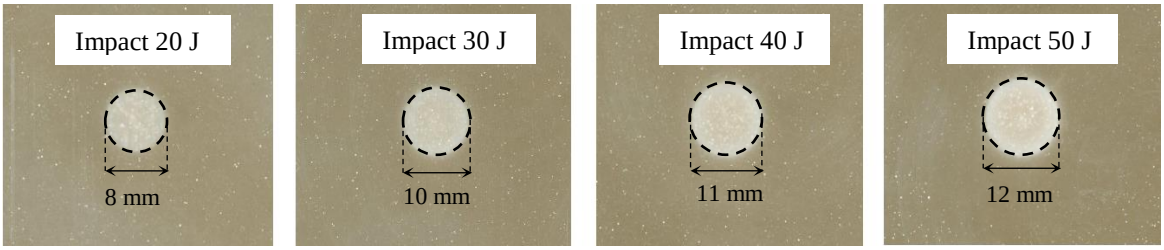

Figure 4.11: Visual impact damage on the top face of ATH/epoxy specimens

4.5.1.2 Numerical results

The viscoplastic-damage model was applied to simulate the impact response of the ATH/epoxy specimen under an impact energy of 40 J. The goal was to validate the proposed model for the

AHT/epoxy behavior. The numerical force-time and energy-time curves are plotted in Figure 4.12a and b with curves obtained from the experimental tests. In general, close correlation is achieved between the FE simulation and experimental data. The maximum predicted contact force is approximately 34.8 kN, which is slightly higher than the actual impact load (33.9 kN).

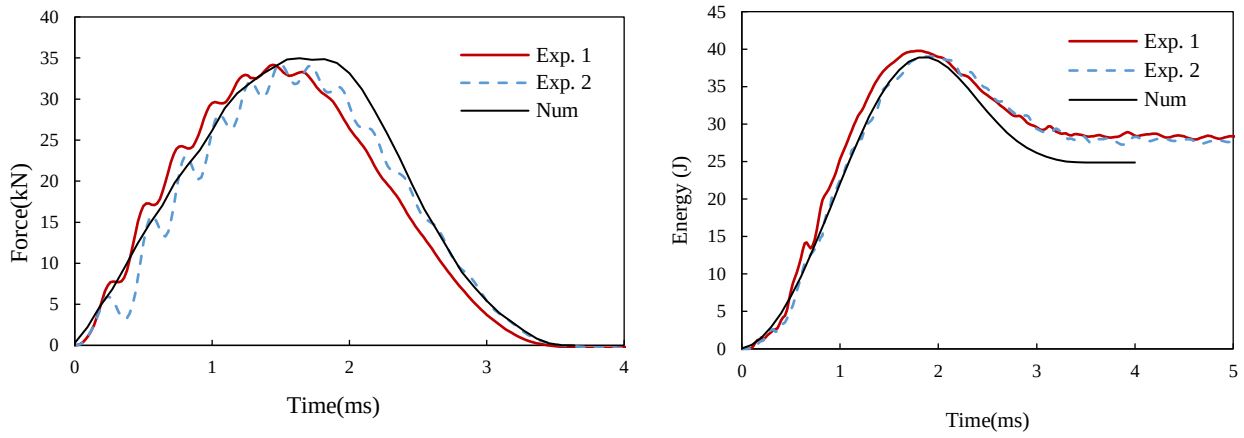

Figure 4.12: Impact response of an ATH/epoxy specimen at an impact energy of 40 J

Moreover, with respect to impact energy, the numerical results show that as much as 25 J of the impact energy applied to the sandwich panel is primarily absorbed through plastic deformations and matrix damage in the ATH/epoxy. The numerical model tends to underestimate the value of absorbed energy, as shown in Figure 4.12b. The difference between the numerical predictions and experimental data appears to be due to the underestimation of the plastic deformation that the ATH/epoxy material suffered during the test.

The comparison of the experimental and predicted damage area at an impact energy of 40 J is shown in Figure 4.13. The red zone reported herein represents the damage area caused by the high-intensity compressive stress in the localized contact area. The numerical model is able to capture the shape (circular) and size of the damage area. The internal damage depth was also measured after destructive cross- sectioning of the impacted specimen, as shown in Figure 4.13a. The light area with a maximum depth of 6 mm represents the internal damage zone. Experimental observations confirm the predicted damage depth under the impact point (Figure 4.13b) and reveal the suitability of the proposed material model for simulating the damage pattern in the ATH/epoxy specimen.

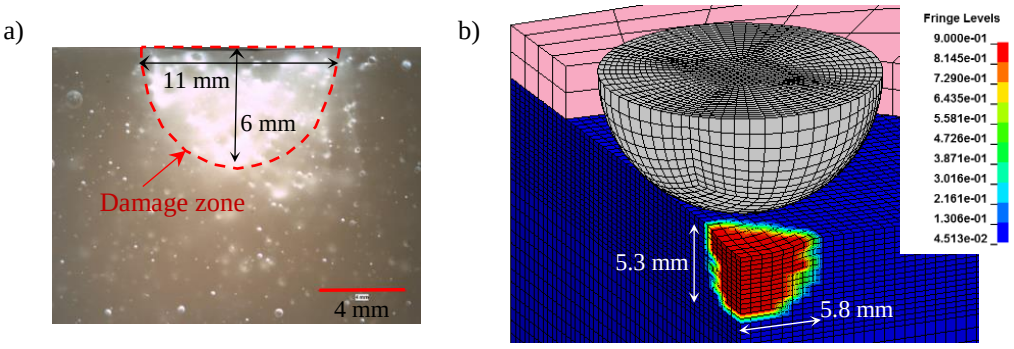

Figure 4.13: Damage zone in an ATH/epoxy specimen at an impact energy of 40 J: a) experimental observation and b) numerical result

Moreover, the numerical analysis indicates the presence of an irreversible plastic deformation in the ATH/epoxy specimen at the impact zone. This numerical finding corresponds well with a permanent indentation of 0.28 mm in depth detected in the impacted specimens.

4.5.2 Impact response of the sandwich panels

4.5.2.1 Impact force and energy history

The contact force-time curves and energy-time curves of the sandwich panels subjected to impact loading at energy levels of 20, 30, 40 and 60 J are plotted in Figure 4.14 and Figure 4.15, including the numerical predictions and experimental data. The force history curves show a nonlinear response as the contact area between the projectile and sandwich panel increases. Once reaches the maximum value, the contact force undergoes a slight rapid decrease as the impactor rebounds.

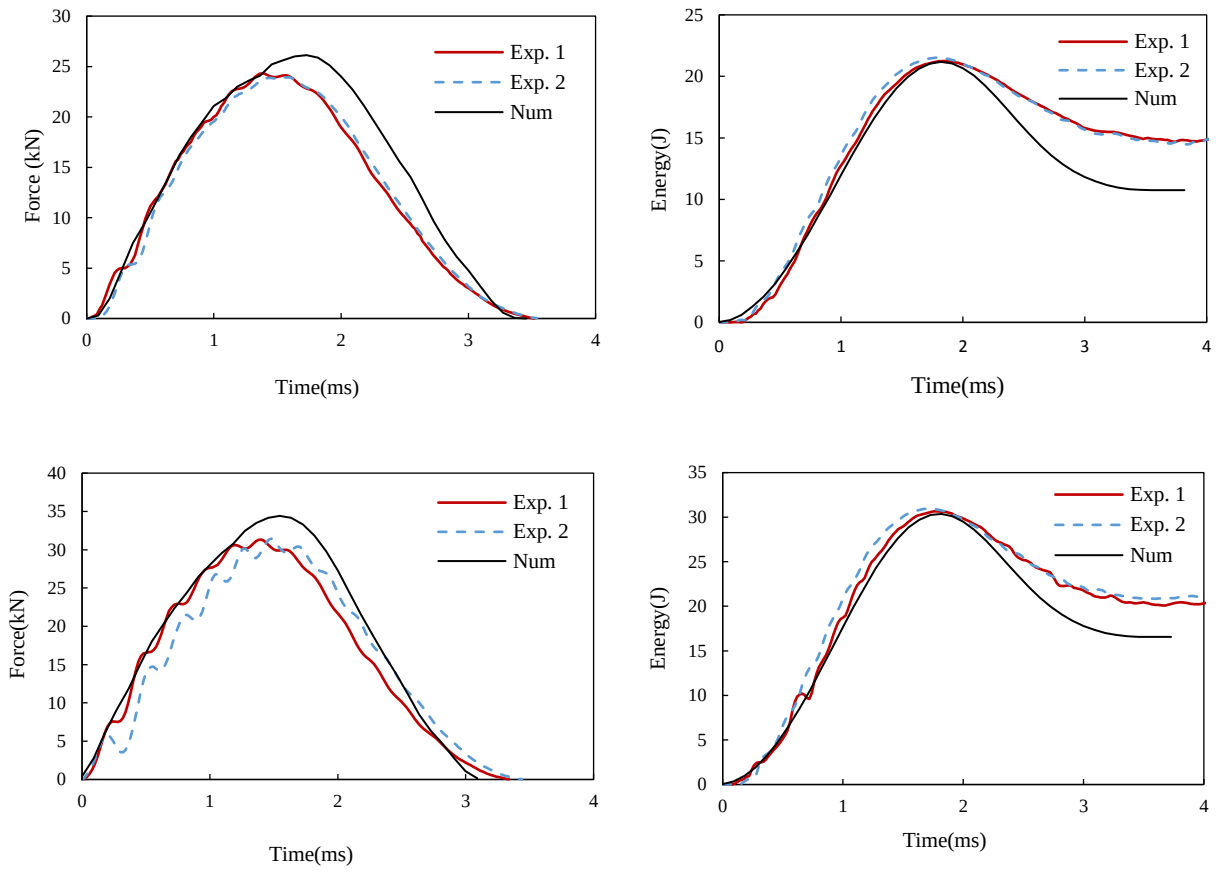

Figure 4.14: Impact response of a sandwich panel for impact energies of a) 20 J and b) 30 J

The comparisons in Figure 4.14 and 15 illustrate that reasonable correlation is achieved among the numerical predictions and experimental data for both force-time and energy-time curves. However, the numerical model slightly overestimates the peak contact force of the sandwich panels. The peak contact force increases linearly with increasing impact energy. A similar increasing trend in the energy absorption with increasing impact energy is observed in the energy-time curves. In addition, analysis of the experimental and numerical results indicates no load drop in the force-time curves of all investigated impact energies. Singh et al. (2015) reported that the appearance of critical failure modes (such as fiber breakage or unstable delamination growth) generates a sudden load drop in the force-time curve. Thus, there is no evidence of critical impact damage in the impacted sandwich panels.

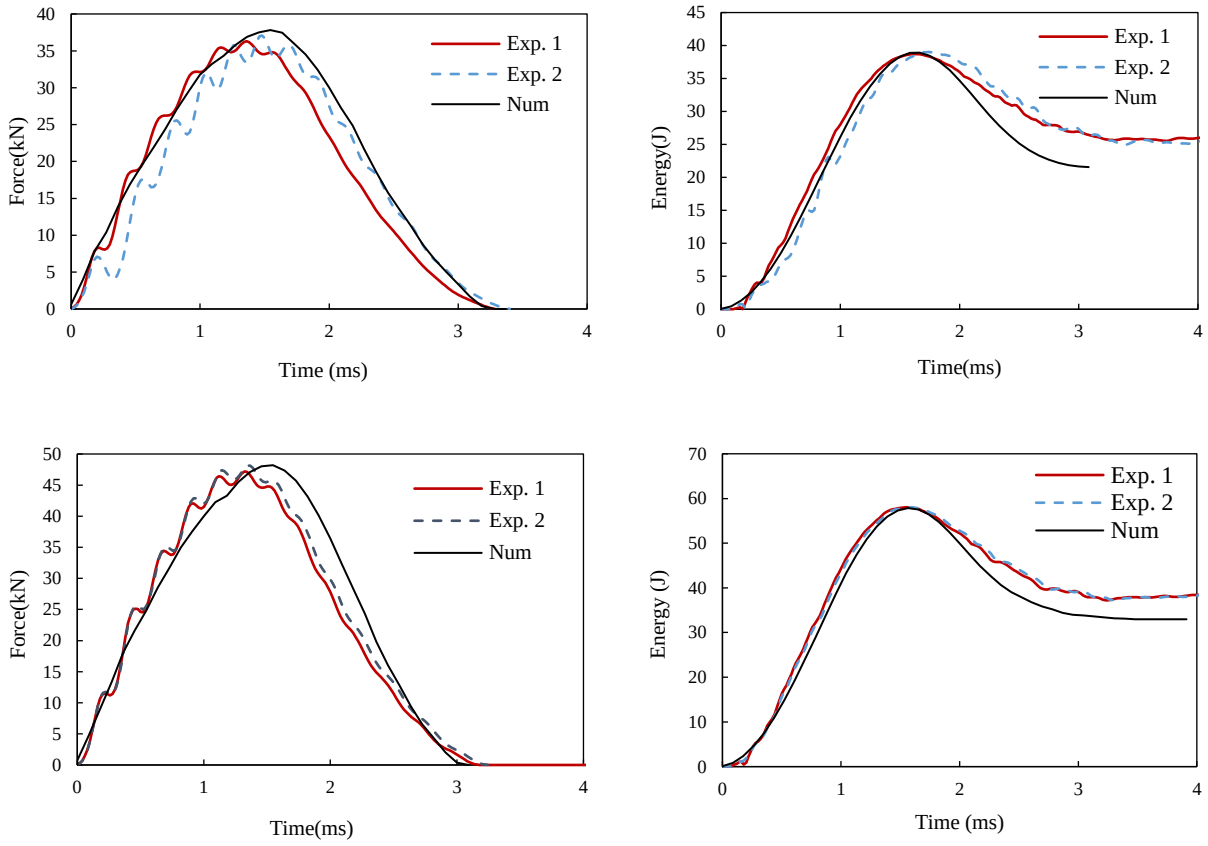

Figure 4.15: Impact response of a sandwich panel for impact energies of a) 40 J and b) 60 J

The peak contact force value at an impact energy of 20 J is approximately 24 kN, which is highly similar to that achieved for the ATH/epoxy specimen (22 kN). A similar trend is observed for all levels of impact energies. As expected, the sandwich panel is slightly stiffer than the ATH/epoxy specimens and has a higher peak force value. The experimental and numerical results reveal that the core material played main role in the impact response of sandwich panels.

The analysis of the energy absorption shows that, the predicted absorbed energy is slightly underestimated compared to the experimental data in the majority of cases, as shown in Figure 4.14b and Figure 4.15b. The observed difference could be attributed to the irreversible plastic deformation in the core material. As shown in Figure 4.16, the numerical model predicts less permanent deformation than that measured experimentally. The permanent deformation (presented in this figure) was measured at the time of the loss of contact between the specimen and impactor. However, the permanent deformation after a few days of relaxation did not exceed the barely

visible damage (0.3 mm (Alderliesten, 2009)) for the range of impact energy levels under investigation.

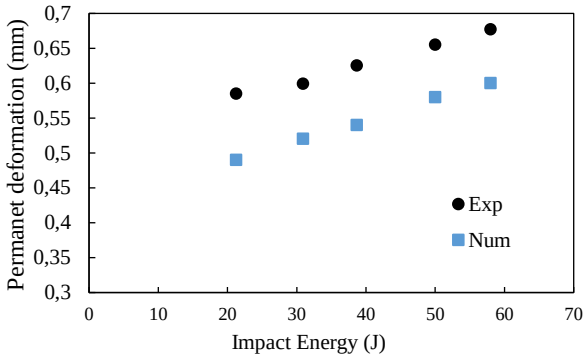

Figure 4.16: Permanent deformation versus the impact energy

4.5.2.2 Force-displacement curves of sandwich panels

The force-displacement curves are shown in Figure 4.17 for all investigated impact energies. The experimental results show that flexural stiffness of sandwich panels slightly increases with increasing impact energy. This could be attributed to the effects of strain rate on the behavior of ATH/epoxy core. The mechanical response of sandwich panels also includes an oscillatory phenomena visible in the force-displacement curves. The harmonic oscillations that are fluctuating around a mean value are caused by the flexural wave propagation within the sandwich panel and impactor (Feraboli, 2006). The amplitude of oscillations increases as the impact energy increases, while frequency of oscillations decreases. Wang et al.(2016) also reported similar oscillations in the impact response of sandwich panels with Balsa HD core and PS foam core.

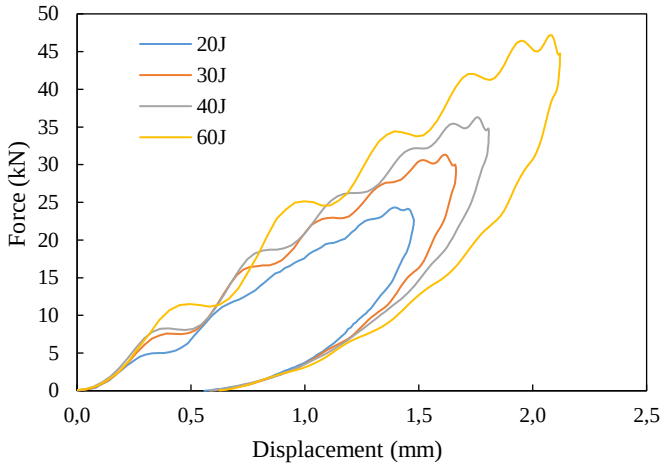

Figure 4.17: Force-displacement curves at various impact energies

The numerical analysis of the displacement field shows that the impact-induced deformation includes the global flexural deformation and local indentation components at the impact point, as shown in Figure 4.18. The obtained results indicate that the local indentation of the sandwich panel is significantly greater than the global flexural deformation. For instance, the local indentation at the impact point is approximately 2 mm under an impact energy of 60 J, whereas the global deformation is approximately 0.19 mm. Indeed, the flexural deformation in the face sheets decreased considerably due to the core stiffness, and hence, the amount of matrix cracking in the tension side of the sandwich is insignificant. In contrast, the indentation deformation that causes the shear cracks in the top face sheet and the core crushing is more pronounced in this sandwich panel.

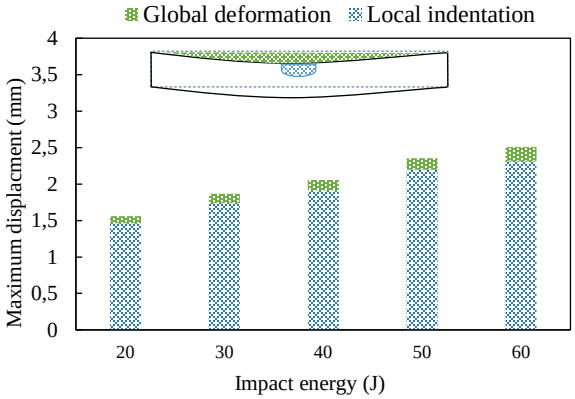

Figure 4.18: Global deformation and local indentation of sandwich panels

4.5.2.3 Damage propagation

Damage area is an important criterion for evaluating the damage resistance of composite materials. The visual damage areas in the top face sheet of sandwich specimens that occurred as a result of low-velocity impact tests are illustrated in Figure 4.19. The area of impact-induced damage increases slightly with increasing impact energy. Overall, the size of the damage area is relatively small even for high-impact energy, such as 60 J.

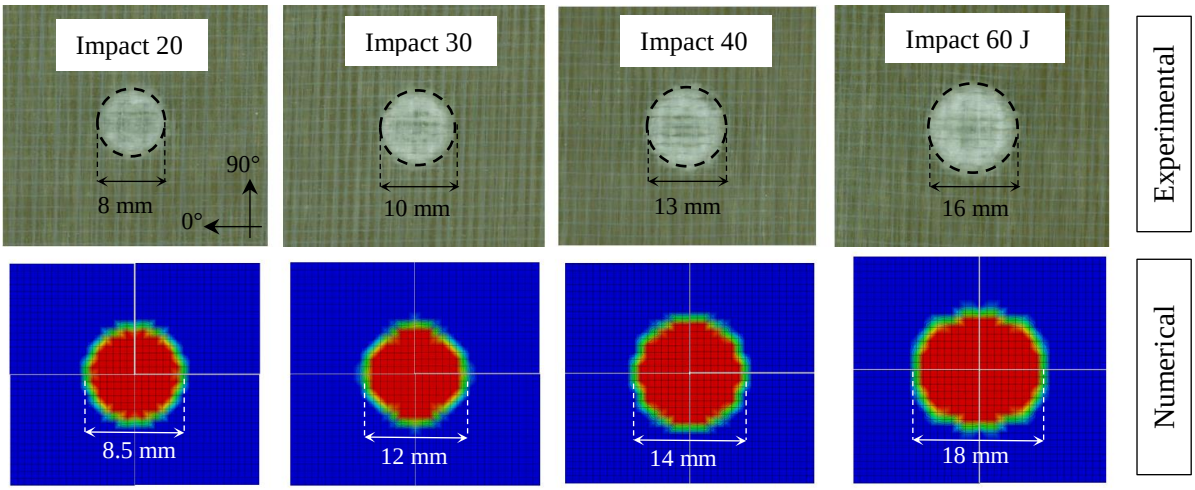

Figure 4.19: Comparison between the experimental and numerical damage on the top face sheet at various impact energies

Further details regarding the damage zone in both the upper face sheet and core were obtained using a destructive observation method. The impact-damage area after sectioning of the sandwich panel impacted at 40 J is shown in Figure 4.20 as an example. The light conical area in the top face sheet indicates the matrix damage in the NCF laminated face sheet. The microscopic observation reveals that critical damage modes, such as fiber breakage and delamination, did not occur in the damage zone. The compressive stress and the shear stress between ply interfaces appear to not be sufficiently high to initiate fiber failure and interface delamination, respectively. Moreover, the presence of polyester yarn through-thickness reinforces the delamination resistance (Tan et al., 2012). Therefore, although matrix crushing and matrix-fiber debonding are observed in the damage zone, they did not extend as interface delamination.

As shown in Figure 4.20, the light semi-spherical region near the top face in the ATH/epoxy core represents the core crushing. The maximum damage depth measured in the experimental samples

is approximately 5 mm for an impact loading of 40 J. Moreover, the microscopic examinations indicate that debonding failure at the face/core interface and top face wrinkling did not occur near the impact point (Figure 4.20). ATH/epoxy appears to develop good bonding with NCF glass-laminated face sheets during the infusion process. In general, the sliding mode is the main cause of the face sheet/core debonding. In this case, the shear strength of the face/core interface is not exceeded due to the high elastic modulus of the ATH/epoxy material. A previous study reported that the critical energy release rate is affected by the core properties (Guédra-Degeorges, 2006). Goswami et al. (2001) also concluded that the core's elastic modulus has a considerable effect on the interface debonding resistance. All these results reveal that the ATH/epoxy core enhances the impact damage resistance of the face sheet.

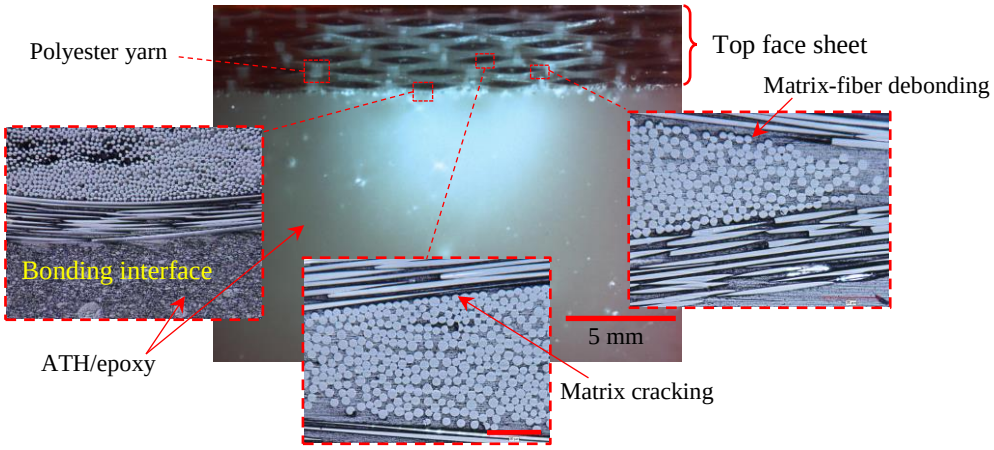

Figure 4.20: Damage observed after cross-sectioning in a sandwich specimen at 40 J

Figure 4.21b presents the predicted damage area (marked with the color red) in the top face sheet and the ATH/epoxy core at an impact energy of 40 J. The numerical results reveal the capacity of the model to predict the damage initiation and propagation during the impact event. The damage pattern in the top face sheet is also accurately predicted in terms of shape and size. The numerical analysis indicates that the matrix shear cracks is a dominant damage mode occurring in the impacted face sheet because the orientation of fracture plane $|\theta|$ varies between 30° and 70° (Richardson et al., 1996b). This damage mode was provoked by the high transverse shear force in the impact zone. The localized damage zone in the ATH/epoxy core is also shown in Figure 4.21c. The predicted damage depth is approx. 4.7 mm, which is highly similar to the damage depth obtained experimentally (5 mm).

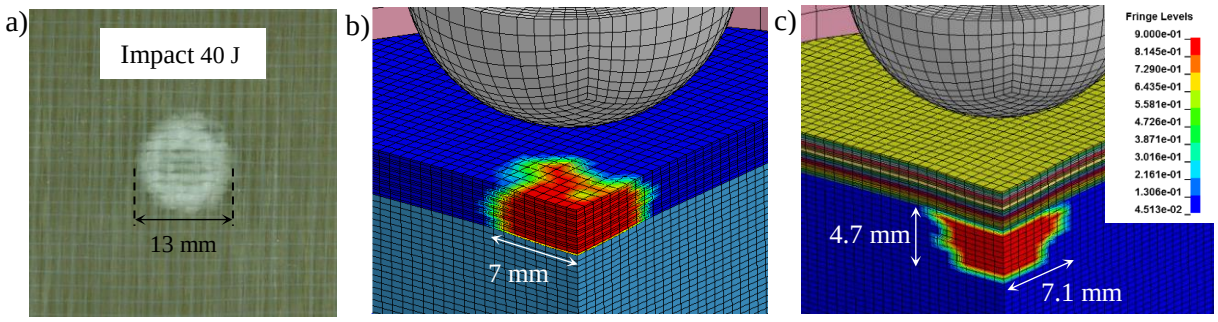

Figure 4.21: Damage zone in a sandwich panel under an impact energy of 40 J: a) experimental face sheet damage, b) matrix shear cracks of the face sheet and c) core crushing

Furthermore, perforation of the top face sheet did not occur under all investigated impact energies up to 60 J. Unlike the sandwich panels with lightweight cores, such as foam cores or honeycomb cores (Hoo Fatt et al., 2000; Zhou et al., 2012), the perforation of the ATH/epoxy sandwich occurs at high impact energies due to the high compressive strength of the ATH/epoxy core (150 MPa). Because the shear and tensile strengths of the ATH/epoxy core (30 and 50 MPa, respectively) are significantly lower than the compressive strength (due to the presence of ATH particles in the epoxy resin), other failure modes, such as core shear failure and face/core debonding, are more likely to occur before perforation. Thus, additional work is required to investigate the other failure modes of this sandwich panel.

4.5.2.4 Energy absorption

The energy dissipation in each component of the sandwich panel was tracked to highlight the role of the ATH/epoxy core on the energy dissipation process under impact loads. Figure 4.22 displays the energy dissipated in the core and face sheets of sandwich panels for all investigated impact energies. The results illustrate that the total energy dissipation increases linearly with increasing impact energy. The energy dissipation in the top face sheet increases slightly, whereas the increase in energy dissipation in the core is more noticeable. The slight increase in energy dissipation in the face sheet corresponds well with the experimental observation of a small change in the size of the damage zone (Figure 4.19). Damage extension is the main source of energy dissipation in the top face sheet.

According to this histogram, the energy dissipated in the ATH/epoxy core is as much as five times higher than that dissipated in the face sheets under an impact energy of 40 J. In fact, more than 45% of the initial kinetic energy is absorbed through core crushing (which is approximately 70% of the overall absorbed energy). However, less than 12% of the initial kinetic energy is absorbed in the upper face sheet. The numerical results indicate that the ATH/epoxy core increases the energy absorption capacity of the sandwich panel. These numerical findings are consistent with the previous results that the ATH/epoxy has a good ability to locally deform, and hence absorb a considerable amount of the energy dissipated in the entire structure.

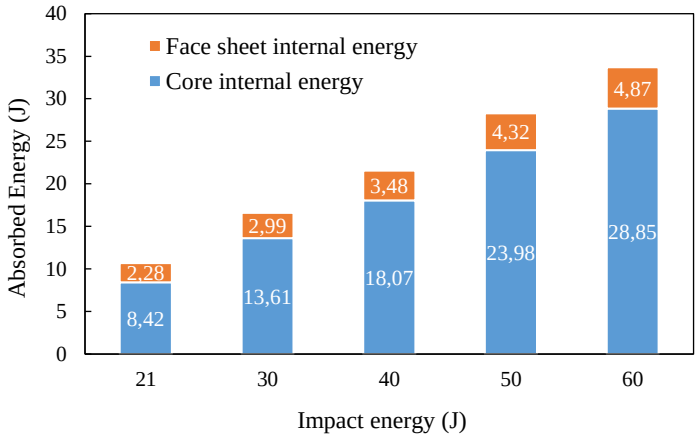

Figure 4.22: Energy dissipation mechanism for all investigated impact energies

4.6 Conclusions

The impact resistance of an innovative sandwich panels with a core made of epoxy resin filled with alumina trihydrate particles was investigated via experimental and numerical analyses. A 3D finite element model was implemented in the FEM software LS-DYNA/Explicit to predict damage propagation in the face sheets and core of the sandwich panel. This FEM model includes a physically-based continuum damage model used to describe the behavior and failure of the NCF glass/epoxy composite face sheets, accounting for matrix damage, delamination, and fiber failure. In addition, a viscoplastic-damage model was employed to simulate the ATH/epoxy behavior, which includes a nonlinear plastic response and matrix damage propagation.

Low-velocity impact tests under impact energies up to 60 J were conducted to validate the numerical model. The damage model used to simulate damage propagation in the face sheet accurately reflected the experimental damage in the face sheet, and the viscoplastic-damage model

of ATH/epoxy precisely predicted the damage propagation and absorbed energy in the ATH/epoxy specimens.

The numerical and experimental results illustrated that the peak contact force and energy dissipation increase linearly with increasing impact energy. The numerical results indicated that up to 50% of the initial impact energy was absorbed by the core material, whereas a small amount of energy was dissipated in the top face sheet through matrix damage. Detailed analysis of damage in the impacted zone revealed no evidence of fiber breakage, delamination or face sheet/core debonding. The primary failure mode was local indentation in the face sheet and core. Furthermore, a barely visible indentation of less than 0.3 mm in depth was measured under an impact loading of 60 J. Therefore, the sandwich panel demonstrates a considerable performance in term of damage resistance. The main reason for the high damage resistance is that the core of the sandwich panel can undergo considerable plastic deformation before failure. The irreversible plastic deformation allows the core material to absorb a large amount of impact energy as internal energy. The ability of the ATH/epoxy material to deform locally and absorb a large amount of impact energy makes it a suitable choice for the sandwich core when impact damage resistance is the main design issue.

Further investigations are needed to demonstrate the capability and the limitation of sandwich panels with ATH/epoxy core under various loading condition. The other failure modes of sandwich panels such as core shear failure, face sheet failure and face/core debonding must be studied, particularly under large deformation which was not a focus of this study.

CHAPTER 5 ARTICLE 3: FAILURE MECHANISMS OF SANDWICH BEAM WITH AN ATH/EPOXY CORE UNDER STATIC AND DYNAMIC THREE-POINT BENDING

G. Morada, A. Vadean, R. Boukhili (2017). Journal of Composite Structures, 176, pp. 281-293.

5.1 Abstract

In this work, mechanical response of a new sandwich beam with a hybrid core composed of epoxy resin and Alumina trihydrate (ATH) was investigated. Interactions between the indentation mode and the core shear failure mode, as well as the role of core/face debonding were evaluated as part of the failure mechanism. A digital image correlation technique (DIC) was used to capture the sequence of failure and the strain field during quasi-static loading. In addition, an explicit nonlinear finite element model was developed to predict the evolution of damage in the sandwich face sheet and core. The model includes a viscoplastic-damage model to simulate the strain rate-dependent behavior of the core material. The numerical results were compared with the impact data to demonstrate the ability of the model to follow the evolution of damage from onset to catastrophic failure. It was found that shear failure in the core plays the main role in the final failure of sandwich beams. For an impact energy below 60 J, indentation is the dominant failure mode, and its effect on the flexural response of the beam was demonstrated.

5.2 Introduction

Hydroelectric power plants have always been a valuable source of green energy. Rehabilitating hydraulic turbines and improving their performance has been an issue of concern to numerous investigators in recent decades. Recently, an innovative solution using a composite extension structure was proposed to modify the stay vane profile and, consequently, to improve the performance of an existing hydraulic turbine (Bornard et al., 2014). The proposed composite sandwich is made of a glass/epoxy reinforcement shell filled with casting epoxy. A preliminary study showed that the hydrostatic pressure on the structure is negligible. However, the sandwich structure is exposed to impacts from debris flowing in the river water. The mechanical performance

of the sandwich structure may degrade significantly after impact-induced damage. Therefore, a damage tolerance evaluation of the sandwich structure is required to ensure that the structure can withstand the impact loads without failure or large structural deformation.

Damage in sandwich structures subjected to low-velocity impacts can be categorized into four major modes of failure (Steeves et al., 2004; Yu et al., 2008): face sheet failure, face/core debonding, core shear failure and indentation. Many researchers have performed three-point bending tests to study the collapse modes of sandwich beams (Crupi et al., 2012; Dey et al., 2015; Thorsson et al., 2016) and have shown that different failure modes can occur in three-point bending tests depending on the geometry of the beam and the support span distance (Crupi et al., 2015). Furthermore, damage initiation and propagation depend upon the material properties of the core and the face sheets, as well as the interaction between them. Styles et al. (2007) reported that thick sandwich panels fail due to core indentation, whereas thin sandwich panels collapse due to the face wrinkling and core crushing. Davies et al. (2004) showed that understanding face/core debonding is essential to interpret the behavior of sandwich structures. Additionally, debonding fracture toughness was also found to increase with the core density (Majumdar et al., 2003). Some researchers have also used three point bending tests to demonstrate the interface debonding resistance (Crupi et al., 2012; Yan et al., 2014). Yu et al. (2008) constructed a failure mechanism map for sandwich beams with an aluminum foam-filled corrugated core subjected to static three-point bending. They showed that the low-velocity impact bending failure modes are similar to those for quasi-static loading when the impact velocity is less than 5 m/s.

This study investigates sandwich composites made with an ATH/epoxy core and non-crimp fabric (NCF) glass/epoxy laminate for the face sheets, as shown in Figure 5.1. In the authors' previous research, the impact response of sandwich panels with an ATH/epoxy core was analyzed following ASTM D3763 (2006) for various impact energies up to 60 J. The obtained experimental and numerical results showed that the localized indentation in the top face sheet and the core was more pronounced than the global bending deformation of the sandwich panels due to its high bending resistance. However, the actual structure of the extension may undergo global bending deformation due to its geometry and the boundary conditions. Thus, it is necessary to conduct dynamic three-point bending tests. Furthermore, a study of the relevant literature indicates that only a limited number of composite sandwich structures can withstand high- energy impacts, which is required for this application.

Experimental results on the bending response and the failure mechanisms of sandwich composite beams with an ATH/epoxy core under static and dynamic three-point bending are presented in this article. The goal of this study is to understand the initiation and propagation of the failure modes of the sandwich beams under three-point loading. This also includes an estimation of the minimum impact energy that triggers the collapse of the sandwich beam, and finally, the loss of structural integrity. Digital image correlation technique was used to observe the initiation and propagation sequence of the failure modes. Furthermore, a progressive damage model was implemented in LS-DYNA/explicit software to simulate the propagation of damage in the face sheets. Likewise, a viscoplastic-damage model is proposed to simulate the behavior and failure of the core. The numerical results were compared with experimental data that were previously obtained from three-point bending tests on ATH/epoxy core sandwich beams.

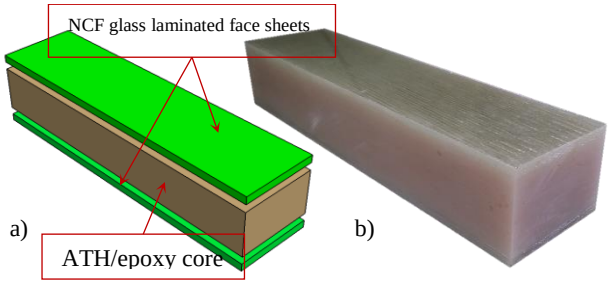

Figure 5.1: a) Schematic of the sandwich beam and b) beam test sample

5.3 Specimens and test configurations

The face sheets of the sandwich composite beam were made from NCF E-glass/epoxy reinforced composite laminates. The face sheets were stacked in a $[\{90°/0°/90°\}]_{3s}$ lamination sequence, resulting in a face sheet nominal thickness of 3.66 mm. Each NCF fabric layer consists of three plies of {90°/0°/90°} stitched together using polyester yarn. The face sheets were manufactured using a vacuum infusion (VI) process. The sandwich core was prepared by mixing the resin epoxy (Araldite® LY 8601) with 60% wt. ATH particles and a hardener (Aradur® 8602). The polymerization mixture was poured into a wood mould in which the face sheets had been previously positioned on both sides. The mould was clamped to ensure sufficient pressure on the sandwich panel so that the total thickness of the sandwich did not exceed approximately 34 mm. After the casting process, the curing of the ATH/epoxy core was performed at room temperature for 24 h. Following the curing process, the sandwich panels were cut into test specimens. At least

three specimens were used to perform three-point bending tests. The density of the ATH/epoxy core was found to be approximately 1.76 g/cm^3.

5.3.1 Quasi-static three-point bending test

Three point bending tests were conducted on an ATH/epoxy core sandwich beam using an MTS testing machine following the ASTM C393 standard, as shown in Figure 5.2a. The dimensions of the test specimens are presented in Table 5.1. The load was applied at a displacement rate of 2 mm/min with a preload of 5 N. The diameter of the loading head was 25.4 mm. The sandwich beam was supported by two 5-mm-diameter rods. The tests were performed at two different support span distances. According to the ASTM standard, to determine the core shear strength or the core/face bonding strength, the support span must be sufficiently short so that the core shear failure or the core/face debonding occurs prior to the face sheet failure. Therefore, the support span length of the short beam was calculated and set at 60 mm. Moreover, the support span length of the long beam was set at 150 mm to determine the sandwich flexure behavior.

Table 5.1: Dimension of sandwich beam specimens

Analyse type	specimen	L(mm)	b(mm)	t(mm)	Span length
quasi-static	short beam	100	50	34	60
quasi-static	long beam	200	50	34	150
dynamic	long beam	200	50	34	150

5.3.2 Flexural impact test

Dynamic three-point bending tests were also conducted on the ATH/epoxy core sandwich beams using a drop tower, as shown in Figure 5.2b. The impactor had a mass of 22.8 kg with a hemispheric head diameter of 25.4 mm. The radius of the two steel supports was 5 mm. The support span length was set to 150 mm. The impact tests were performed at various impact energies. Additionally, the impact energy was gradually increased to determine the impact energy needed to collapse the sandwich beam.

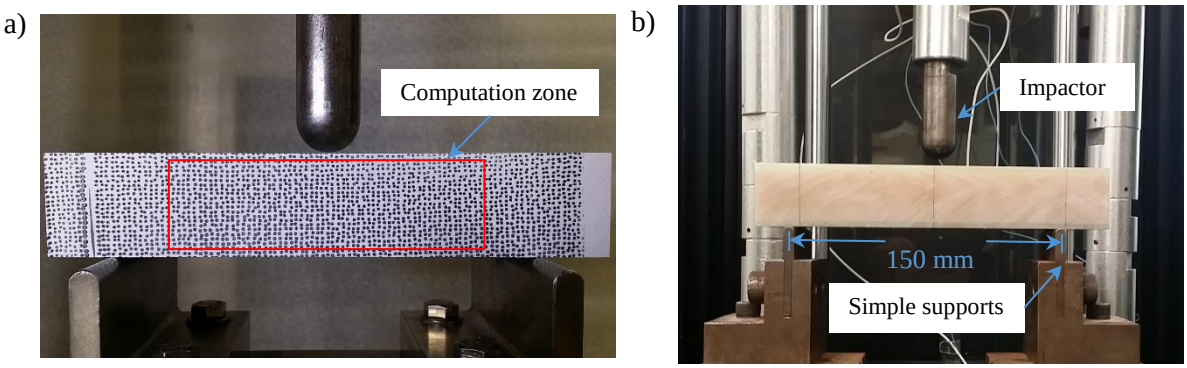

Figure 5.2: a) Three-point bending test setup and b) low-velocity impact test configuration

5.3.3 Digital image correlation (DIC)

Three-dimensional DIC can be used to obtain the displacement and strain fields and to capture the sequence of failure initiation and propagation during a quasi-static loading event. The images were recorded using a high-speed camera. The displacement field was computed by dividing the reference image into pixel subsets and then tracking the distortion of the image pattern, which was assumed to be due to mechanical deformation. The vertical displacement (which represents the global bending deformation) was calculated at the center of the sandwich beam.

5.4 Numerical models

Numerical simulations of the response of the sandwich beams under the quasi-static and dynamic bending loading conditions were carried out using three-dimensional finite element models. Two representative sandwich beams with different span supports were selected for numerical investigation, as illustrated in Figure 5.3.

The laminated face sheets were meshed using 8-node linear solid elements with reduced integration for each ply. The face sheet behavior was defined using a UMAT subroutine implemented in LS-DYNA software. The core was also discretized using reduced integration solid elements. The behavior of the ATH/epoxy core was simulated using a viscoplastic-damage model that was integrated into the simulation via a second UMAT subroutine.

Zero-thickness cohesive elements were used for the ply interfaces to simulate delamination between plies with different fiber orientations. The hemispherical impactor and support rods were defined as perfectly rigid bodies. ERODING_SINGLE_SURFACE was adopted to define the

contact between the impactor, sandwich beam and supports and between the individual face sheet plies. Moreover, cohesive elements were inserted at the face sheets and core interface to account for the face/core debonding failure mode. Material model type 138, MAT_COHESIVE_MIXED_MODE, was used to define the cohesive elements.

To decrease the computation time, symmetric boundary conditions were employed so that only a quarter of the sandwich had to be modeled. After performing a mesh convergence analysis, the in-plane size of the sandwich beam mesh was determined to be 1 mm×1 mm. Quasi-static loading was performed by applying a displacement controlled load at the top of the impactor with a loading rate of 2 mm/min. The dynamic loading was setup by assigning an initial velocity to the impactor.

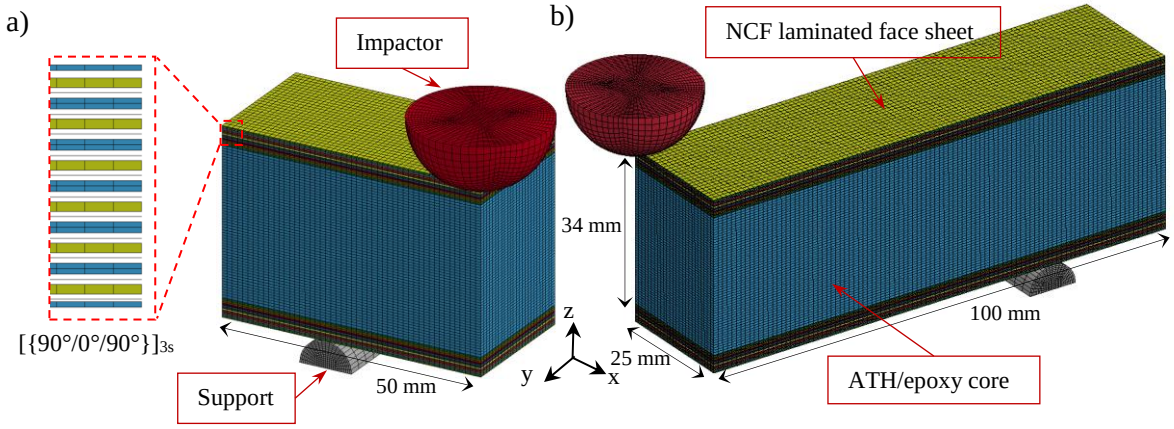

Figure 5.3: Numerical model of three-point bending: (a) short sandwich beam and (b) long sandwich beam

5.4.1 Progressive damage model of face sheet

The constitutive behavior of the face sheet was defined using individual material constitutive laws for each ply. The NCF glass/epoxy fabric layer {90°/0°/90°} was discretized into three plies with different orientations and jointed by the cohesive elements. Each ply was modeled as a homogeneous orthotropic material in collaboration with a physically-based continuum damage mechanics approach to account for matrix damage propagation. Furthermore, irreversible plastic deformation was considered for the shear-strain behavior to capture the nonlinear behavior of the ply. The strain-softening associated with the continuum damage mechanics was defined by inserting a matrix damage variable d_m in the material constitutive laws. Indeed, the stress components are first rotated into the potential fracture plane following the onset of matrix damage.

The rotated stress components are then degraded using the matrix damage variable d_m and eventually transformed back into the original plane. Because no evidence of fiber breakage was detected under tension or compression in the face sheets, the longitudinal stress was assumed to be intact.

5.4.1.1 Matrix damage initiation

Matrix cracking and matrix crushing are the first damage modes that appear in the impacted composite structures. If σ_{nn}, τ_{nt} and τ_{nl} are assumed as stress components acting on the potential fracture plane, then the matrix cracking criteria proposed by Catalanotti et al.(2013) and the matrix crushing criteria proposed by Puck (1998) can be expressed as follows:

$$F_{22}^{C} = \left(\frac{\tau_{\mathrm{nl}}}{S_{\mathrm{l}}^{is} - \mu_{\mathrm{nl}}\sigma_{\mathrm{nn}}}\right)^2 + \left(\frac{\tau_{\mathrm{nt}}}{S_{\mathrm{t}}^{is} - \mu_{\mathrm{nt}}\sigma_{\mathrm{nn}}}\right)^2 - 1 \geq 0 \tag{5-1}$$

$$F_{22}^{T} = \left(\frac{\sigma_{\mathrm{nn}}}{S_{\mathrm{t}}^{is}}\right)^2 + \left(\frac{\tau_{\mathrm{nl}}}{S_{\mathrm{l}}^{is}}\right)^2 + \left(\frac{\tau_{\mathrm{nt}}}{S_{\mathrm{t}}^{is}}\right)^2 + \lambda\left(\frac{\sigma_{\mathrm{nn}}}{S_{\mathrm{t}}^{is}}\right)^2\left(\frac{\tau_{\mathrm{nl}}}{S_{\mathrm{l}}^{is}}\right)^2 + \kappa\left(\frac{\sigma_{\mathrm{nn}}}{S_{\mathrm{t}}^{is}}\right)^2 - 1 \geq 0$$

where κ and λ are computed by $\kappa = \left(S_l^{in^2} - Y_t^{is}\right)/S_t^{is}\,Y_t^{is}$ and $\lambda = 2\mu_{nl}S_t^{is}/S_l^{is} - \kappa$. Additionally, Y_t^{is} is the in-situ matrix tensile strength and S_t^{is} and S_l^{is} are the shear strengths in the transverse and longitudinal directions, respectively. According to the Mohr-Coulomb theory, the friction coefficients are calculated from $\mu_{nt} = -1/\tan(2\theta_f)$ and $\mu_{nl} = \mu_{nt}S_l^{is}/S_{\mathrm{t}}^{is}$, where $S_{\mathrm{t}}^{is} = Y_{\mathrm{c}}^{is}/2\tan(\theta_f)$ and Y_{c}^{is} is the in-situ matrix compressive strength. In this case, the maximum ply thickness in the simulation is 0.29 mm, which is < 0.8 mm. Therefore, the in-situ strength values were obtained from the thin embedded ply assumption given by Camanho et al. (2006). The angle of the fracture plane θ_f is approximately 53° for a unidirectional laminate under pure compressive loading. The stresses acting on the potential fracture plane are calculated using the standard transformation matrix $T(\theta)$:

$$\sigma_{nlt} = [T(\theta)]\sigma_{123}[T(\theta)]^T \tag{5-2}$$

The potential fracture plane makes an angle of θ with the vertical axis, as shown in Figure 5.4. The fracture plane orientation for each element is obtained by incrementally changing the value of θ to determine the angle that maximizes the matrix failure criteria.

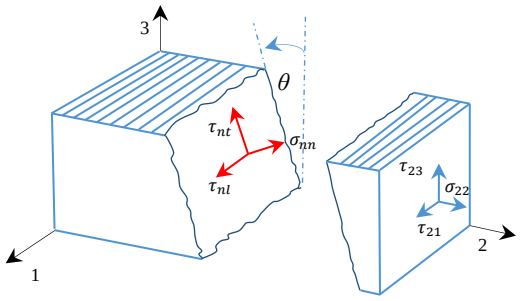

Figure 5.4: Potential fracture plane under compression loading

5.4.1.2 Matrix damage propagation

Once matrix failure is detected under the combined normal and shear stress loading, the resultant stress σ_r and corresponding strain ε_r acting on the potential fracture plane are recorded.

$$\sigma_r = \sqrt{\langle\sigma_{nn}\rangle^2 + (\tau_{nt})^2 + (\tau_{nl})^2} \tag{5-3}$$

$$\varepsilon_r = \sqrt{\langle\varepsilon_{nn}\rangle^2 + (\gamma_{nt})^2 + (\gamma_{nl})^2}$$

$$\varepsilon^0_{\mathrm{r,in}} = \sqrt{(\gamma^{in}_{nt})^2 + (\gamma^{in}_{nl})^2}$$

where $\varepsilon^0_{\mathrm{r,in}}$ represents the inelastic component of strain at the onset of failure and $\langle\ \ \rangle$ is the Macaulay bracket. The total strain energies G_r, at the onset of matrix failure must also be recorded. A quadratic combination of the volumetric strain energies corresponding to each stress acting on the fracture plane is used to define the total strain energy as follows:

$$G_r = G_{nn}\left(\frac{\langle\sigma_{nn}\rangle}{\sigma_r}\right)^2 + G_{nt}\left(\frac{\tau_{nt}}{\sigma_r}\right)^2 + G_{nl}\left(\frac{\tau_{nl}}{\sigma_r}\right)^2 \tag{5-4}$$

The volumetric strain energy of each stress component on the fracture plane is computed from:

$$G_i = \int_0^{\varepsilon_r} \sigma_i d\varepsilon_i \qquad i = nn, nt, nl \tag{5-5}$$

The mixed-mode matrix damage variable d_m is then described by using the following expression, which originates from the linear softening of the stress components:

$$d_m = \frac{\varepsilon_{\mathrm{r}}^f - \varepsilon_{\mathrm{r,in}}^0}{\varepsilon_{\mathrm{r}}^f - \varepsilon_{\mathrm{r}}^o}\left(\frac{\varepsilon_{\mathrm{r}}^0 - \varepsilon_r}{\varepsilon_r - \varepsilon_{\mathrm{r,in}}^0}\right) \tag{5-6}$$

where $\varepsilon_{\mathrm{r}}^f$ represents the resultant failure strain obtained from the matrix fracture energy and the characteristic length, which is defined as:

$$\varepsilon_r^f - \varepsilon_r = \frac{2G_m}{\sigma_r l_m} - \frac{2G_r}{\sigma_r} \tag{5-7}$$

The fracture energy of the matrix under the combined stresses is calculated as follows:

$$G_m = G_{IC}\left(\frac{\langle\sigma_{nn}\rangle}{\sigma_r}\right)^2 + G_{IIc}\left(\frac{\tau_{nt}}{\sigma_r}\right)^2 + G_{IIC}\left(\frac{\tau_{nl}}{\sigma_r}\right)^2 \tag{5-8}$$

where G_{IC} and G_{IIC} represent the critical strain energy release rates for modes I and II, respectively. Finally, the shear and tensile stress on the fracture plane are reduced using the following relations, and the updated stresses are transformed back into the original plane.

$$\sigma_{nl} = (1 - d_m)\sigma_{nl} \tag{5-9}$$

$$\sigma_{nt} = (1 - d_m)\sigma_{nt}$$

$$\sigma_{nn} = \sigma_{nn} - d_m\langle\,\sigma_{nn}\rangle$$

Details on the computation of characteristic element length l_m can be found in (Donadon et al., 2008; Falzon et al., 2011).

5.4.2 Viscoplastic-damage model of ATH/epoxy

The ATH/epoxy polymer exhibits highly nonlinear, strain rate-dependent behavior during loading. The unloading behavior of the polymer is generally accompanied by substantial irreversible deformation. It is assumed that the nonlinear response of the polymer is due to inelastic strains that are inherently present in all components of the strain. Therefore, the behavior of ATH/epoxy under compression and tensile loading was defined using a viscoplastic-damage model. The behavior of the polymer in compression is shown in Figure 5.5a. The compression behavior is characterized by a linear elastic response up to the yield point σ_{cy}. Beyond the yield point, the polymer exhibits an inelastic response until reaching the ultimate stress σ_{cu}, and then follows strain-softening behavior.

Finally, it terminates with residual stress in the polymer. If the polymer undergoes unloading, which is common for impact events, the polymer response will follow the linear-elastic unloading path. Once the stress returns to zero at the end of unloading, a residual irreversible strain will remain in the polymer.

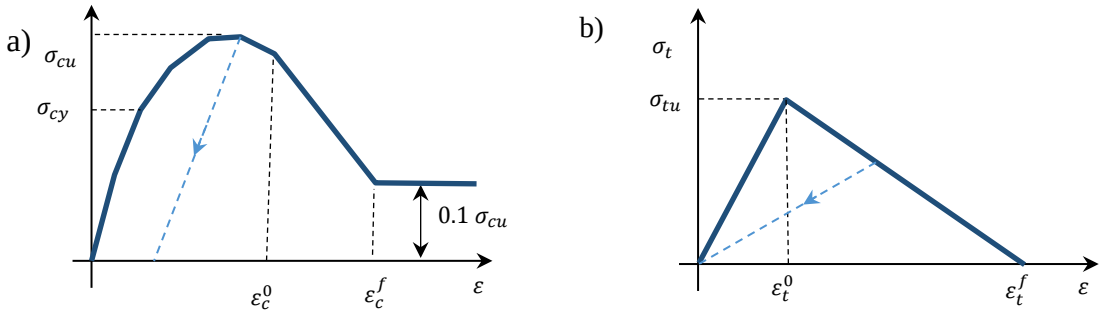

Figure 5.5: Stress-strain response of the ATH/epoxy core: a) compression and b) tension

The tensile behavior of the polymer is described by a linear-elastic response up to the ultimate tensile stress σ_{tu}, beyond which the material stiffness degrades linearly due to the formation of micro-cracks, which result in strain localization and failure in the polymer (Figure 5.5b).

If E_0 is assumed to be the undamaged elastic modulus of the polymer, the stress-strain relations can be expressed as:

$$\Delta\sigma_{ij} = (1 - d_c)E_0\left(\Delta\varepsilon_{ij} - \Delta\varepsilon_{ij}^I\right) \tag{5-10}$$

$$\sigma_{ij}^{n+1} = \sigma_{ij}^n + \Delta\sigma_{ij}$$

where d_c is a damage variable that takes a value between zero and one. The variable $\Delta\varepsilon_{ij}^I$ represents the inelastic strain increments, which are estimated in the subsequent section.

Furthermore, it has been shown that the elastic moduli of polymers increase with the strain rate. The effect of strain rate on the elastic modulus is taken into account using the following expression:

$$E = E_0\left(1 + C \times ln\frac{\dot{\varepsilon}}{\dot{\varepsilon}_0}\right) \tag{5-11}$$

where C represents the strain rate sensitivity, and $\dot{\varepsilon}_0$ and $\dot{\varepsilon}$ are the reference and applied effective strain rates, respectively. The effective strain rate can be defined as:

$$\dot{\varepsilon} = \sqrt{2/3\left[(\dot{\varepsilon}_{11} - \dot{\varepsilon}_m)^2 + (\dot{\varepsilon}_{11} - \dot{\varepsilon}_m)^2 + (\dot{\varepsilon}_{11} - \dot{\varepsilon}_m)^2 + 2\dot{\varepsilon}_{12}^2 + 2\dot{\varepsilon}_{23}^2 + 2\dot{\varepsilon}_{13}^2\right]} \quad (5\text{-}12)$$

$$\dot{\varepsilon}_m = 1/3(\dot{\varepsilon}_{11} + \dot{\varepsilon}_{22} + \dot{\varepsilon}_{33})$$

5.4.2.1 Polymer plasticity

A viscoplastic model was developed by Goldberg et al. (1999) to define the behavior of pure polymers. The Goldberg model is used here to estimate the inelastic strain in the ATH/epoxy polymer. The inelastic strain rate tensor ($\dot{\varepsilon}_{ij}^I$) is assumed to be proportional to the components of the deviatoric stress (S_{ij}). Thus, the inelastic strain rate is defined as follows:

$$\dot{\varepsilon}_{ij}^I = 2D_0 exp\left[-\frac{1}{2}\left(\frac{Z}{\sigma_e}\right)^{2n}\right]\frac{S_{ij}}{2\sqrt{J}} \quad (5\text{-}13)$$

where D_0 and n are both material constants. The value of n controls the material rate dependence. The effective stress σ_e can be defined as

$$\sigma_e = \sqrt{3J} \quad (5\text{-}14)$$

where J indicates the second invariant of the deviatoric stress tensor. The following relation defines the evolution rate of the internal stress variable Z:

$$\dot{Z} = q(Z_1 - Z)\dot{e}_e^I \quad (5\text{-}15)$$

where q is a material constant related to the hardening rate of the material, and Z_1 represents the maximum value of Z. The maximum value of Z (Z_1) controls the maximum stress. The initial value of Z is defined by the material constant Z_0, which effects the onset of nonlinearity. Finally, the effective deviatoric inelastic strain rate (the term $\dot{e}_e^I$ in Eq. 15) is computed from:

$$\dot{e}_e^I = \sqrt{2/3\dot{e}_{ij}^I\dot{e}_{ij}^I} \quad (5\text{-}16)$$

$$\dot{e}_{ij}^I = \dot{\varepsilon}_{ij}^I - \frac{\dot{\varepsilon}_{kk}^I}{3}\delta_{ij}$$

The material constants of n, Z_0, Z_1 and q can be obtained from shear tests. The procedure to determine these material constants is well explained in the work of Goldberg et al. (1999). The

parameter D_0 represents the maximum inelastic strain rate, which is assumed to 10^4 times the maximum applied strain rate.

5.4.3 Material properties

The mechanical properties of the face sheet were determined form characterisation tests conducted by our group. Tensile tests on $[\{90°/0°/90°\}]_{3s}$ and $[\{-45°/+45°/-45°\}]_{3s}$ specimens were performed following the guidelines given by the ASTM D3039M (2003), while compressive tests on $[\{90°/0°/90°\}]_{3s}$ specimens were executed according to the modified ASTM D695 standard with a gauge length of 4.8 mm. The material properties of the NCF laminate are listed in Table 5.2. Because of the lack of experimental results for NCF laminates, the critical strain energy release rates (G_{IC} and G_{IIC}) obtained from experimental tests of unidirectional E-glass/epoxy (Compston et al., 1998) were used as input parameters to the model. The initial stiffness values of the cohesive interface were estimated as k_N=50E_{33}/t and k_S=50G_{12}/t (2007), while the normal and shear strengths of cohesive element are chosen to be $N=Y_t$ and $S=S_{12}$ because the interface properties can be considered as matrix dominated. The selected material properties were verified by comparing numerical results of the tensile, compressive and shear tests with the experiments.

Table 5.2: Material properties of an E-glass fiber/epoxy NCF laminate

Property	Values
Elastic properties	E_{11} = 34.4 GPa; E_{22} = E_{33} = 6.98 GPa; ν_{12} = ν_{13} = 0.28; ν_{23} =0.5
Strength	Y_t = 45 MPa; Y_c = 120 MPa; S_{12}=30 ;
fracture toughness	G_{Ic} = 800 J/m²; G_{IIc} = G_{IIIc} = 1200 J/m²;
Interface properties	k_N = 120 GPa/mm; k_s = 48 GPa/mm; N = 45 MPa; S = 30 MPa; η = 1.4;

The constitutive properties of ATH/epoxy used in the model were determined from flatwise compression and three-point flexural tests. The compression tests were conducted according to the ASTM D1621-10, with loading rates of 2.5, 50, 100 and 500 mm/min applied on a specimens of 51×51×25 mm^3. The measured force-displacement curves under compressive loading at various strain rates are shown in Figure 5.6a. The three-point bending tests were also performed on ATH/epoxy specimens with dimensions in accordance with the ASTM D790, and a span distance of 60 mm. The flexural behavior of neat epoxy and ATH/epoxy are illustrated in Figure 5.6b. It should be noted that, the material constants of n, Z_0, Z_1 and q were calculated using the procedure described by Goldberg et al. (1999). The values of all the parameters are presented in Table 5.3.

Table 5.3: Material constants of ATH/epoxy polymer

Modulus(GPa)	C	Poisson's ratio	n	Z_0 (MPa)	Z_1(MPa)	q	$D_0(s^{-1})$	$\dot{\varepsilon}_0(s^{-1})$
3.24	0.195	0.3	0.92	321	712	265.1	10^6	10^{-3}

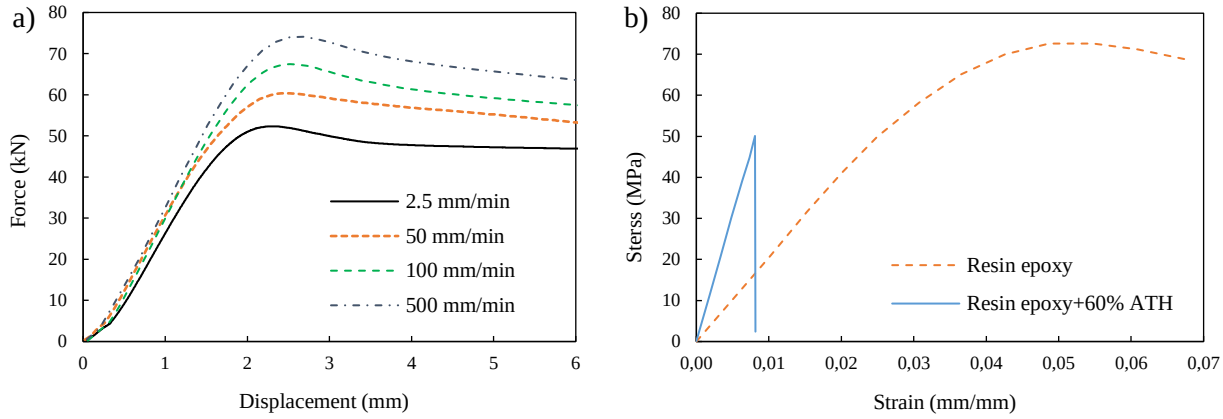

Figure 5.6: a) Force-displacement curves of ATH/epoxy under compressive loading at various strain rates and b) Flexural behavior of ATH/epoxy and neat epoxy.

5.5 Results and discussion

5.5.1 Static three-point bending tests

5.5.1.1 Response of short beam bending

The typical load-deflection curves obtained from bending tests carried on the ATH/epoxy sandwich specimens are plotted in Figure 5.7. The force-deflection curve for the sandwich beam exhibits approximate linear elastic behavior. The force-deflection curve for the sandwich beam exhibits approximately linear elastic behavior up to a large loading of 60 kN. From there on, a slight deviation form linearity is observed before rupture occurs. It seems that the deviation from linearity is caused by significant localized indentation damage in the sandwich beam.

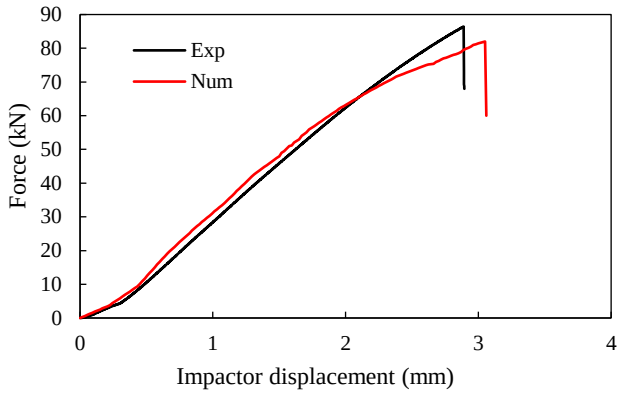

Figure 5.7: Load-deflection curves for the short beam sandwich subjected to quasi-static loading

According to the ASTM C393 standard, core shear failure and face/core debonding are two acceptable failure modes for short sandwich beams. In our case, the sandwich beams collapse due to shear failure of the sandwich core. Indeed, core crushing first occurs immediately below the top face sheet of the sandwich due to high compressive stresses. Then, the core material undergoes shear deformation due to face/core interface bonding. Finally, the shear crack in the core abruptly propagates from the top face sheet toward the bottom face sheet interface. This sequence of failure event is also well reflected in the numerical finding. As shown in Figure 5.8, a long crack through the core thickness between the impactor and one of the supports was found after unloading. This crack propagation behavior leads to asymmetric collapse with an angle of 45°.

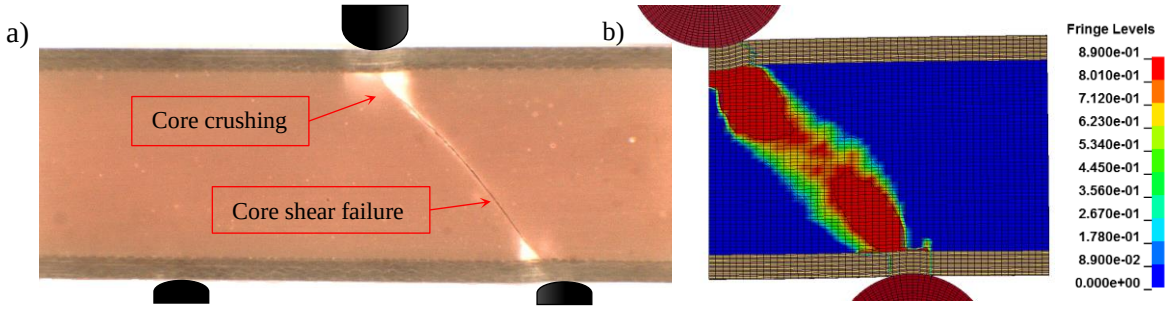

Figure 5.8: Collapse mode for the three-point bending tests: a) experimental and b) numerical

Although the face sheets bear all of the compressive and tensile stresses in bending, the two glass laminated face sheets are thick and too strong to fail during quasi-static loading. Moreover, the visual observations made on the damaged specimens indicate no visible evidence of interface debonding between the face sheet and ATH/epoxy core. This is indicative of good interfacial

bonding between the face sheets and the core during the infusion process. The resistance of the face/core debonding appears to be higher than the core shear strength. The core shear strength can be predicted by ASTM C393:

$$\tau_s^{ult} = \frac{P_{max}}{(d+c)b} \tag{5-17}$$

where P_{max} is the maximum force at failure, d and c are the thickness of the sandwich and the core, respectively, and b is the sandwich width. The average core shear strength is approximately 28 MPa. The amount of the energy absorbed during static loading was calculated by integrating the load-deflection curve. The average energy absorbed through the final failure is approximately 120 J.

5.5.2 Response of long beam bending

The long sandwich beam has a support span length of 150 mm. Increasing the support span length is generally accompanied by a change in the failure mechanism (Crupi et al., 2015). Typical force-deflection curves for the long sandwich beam are presented in Figure 5.9. The force-deflection curve shows an elastic linear response for static loading up to the first load drop. After that, the beam continues to support the load, until the second load drop and final failure of the sandwich beam.

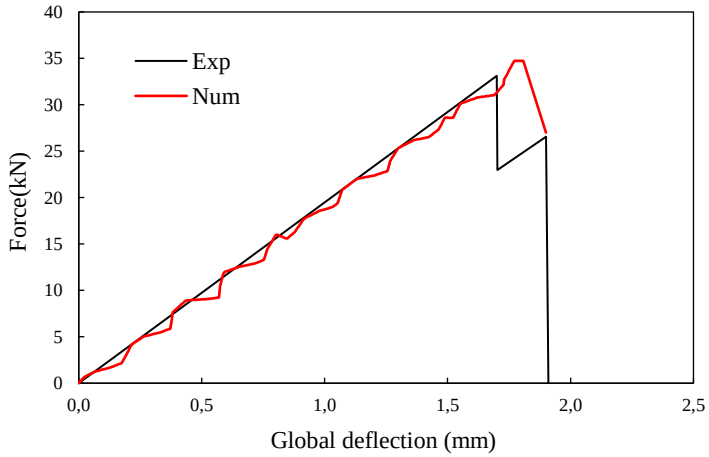

Figure 5.9: Load-deflection curves for long beam sandwich under quasi-static loading

A detailed analysis of the failure mechanism for static loading shows that matrix cracks first occur in the top face sheet and core directly under the impactor and are due to a large compressive stress.

The compressive stress is caused by the localized indentation in the face sheet and core. However, the indentation failure mode does not lead to the final failure of the sandwich beam. The core material experiences the flexural and shear stresses during the static loading (see Figure 5.10a and b). It appears that the combination of these stresses originates the brittle failure of the sandwich beams. An analysis of the DIC results demonstrates that the core crack initiates from the bottom face sheet (near the middle of sandwich beam) and propagates through the core thickness up to the top face sheet (Figure 5.10c). This crack formation causes the first load drop in the force-deflection curve. Finally, the face/core interface debonding occurs at the bottom face sheet and is followed by face/core debonding at the top face sheet, as shown in Figure 5.10d. The crack propagation nearly divides the core into two separated parts.

It is worth noting that the face/core interface debonding does not occur due to a sliding mode, which is generally a dominate mode in face/core debonding (Goswami et al., 2001). The numerical results, as well as the DIC, reveal that the interface debonding occurs as a consequence of the large crack formation in the core. It appears that the crack edge pushes the bottom face sheet downward and initiates the face/core debonding. Therefore, the face/core debonding is mainly caused by the opening mode. This observation agrees with the previous findings that the interface resistance is higher than the core shear resistance and that the face/core interface debonding did not occur in a sliding mode. It has been proved that increasing the elastic modulus of the core and the density of the core improves the interface debonding resistance (Majumdar et al., 2003). The ATH/epoxy core has a significant elastic modulus and density properties, which result in good interface bonding. The use of the same epoxy resin for the glass/epoxy face sheet and the ATH/epoxy core also contributes to improve the interface debonding resistance.

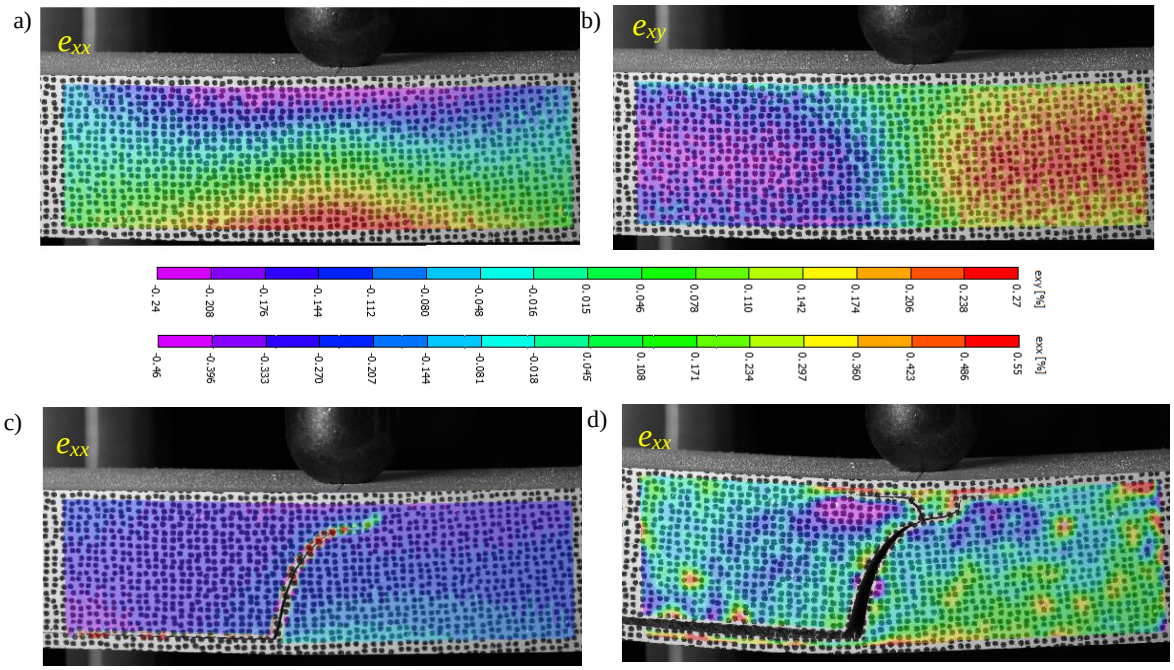

Figure 5.10: (a) Longitudinal strain field before failure, (b) shear strain field prior to failure, (c) failure mode corresponding to the first load drop and (d) failure mode corresponding to final failure

5.5.3 Dynamic three-point bending tests

5.5.3.1 Experimental results

The experimental contact force-time and energy-time histories of the sandwich beams at various impact energies of 20, 40, 60 and 80 J are presented in Figure 5.11. For low impact energies, the force-time curves are characterized by an increasing section of the force as the contact area increases between impactor and specimen; and a decreasing section of the force as the impactor rebounds.

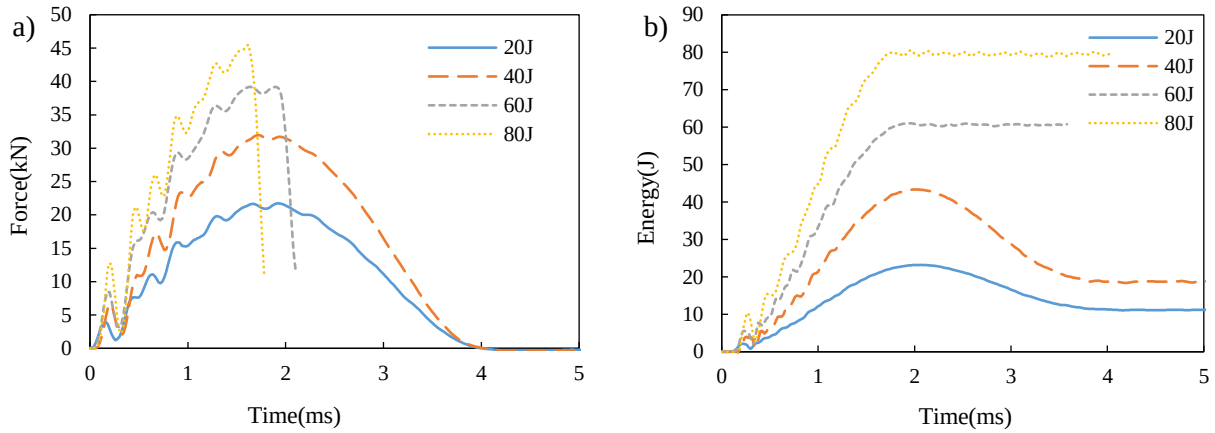

Figure 5.11: Flexural impact response of the sandwich composite beams: a) force-time and b) energy-time curves

For an impact energy of 60 J, the contact force increases gradually to the maximum impact force, in a similar result to the test with an impact energy of 40 J. After reaching the maximum contact force, the force abruptly drops to zero. The impactor does not rebound from the specimen, and the structure is faced with a collapse in the core, resulting in a loss of its integrity. A similar response is also observed for impact energies above 60 J. Experimental data show that the minimum impact energy needed to collapse the sandwich beam is approximately 60 J. Furthermore, detailed analyses of the force-time curve indicate that there is no evidence of the final failure initiation in the curve prior to reaching the peak force. This signifies that the initiation and propagation of the final failure occur almost simultaneously. Thus, the core material in sandwich beams exhibits a brittle nature.

The impact-induced damage in the sandwich beam for impact energies of 60 J and 80 J is illustrated in Figure 5.12. In addition to the minor matrix damage under the impact point, the face sheets are nearly intact. In contrast, a large diagonal crack appears in the middle of the sandwich core immediately under the impact point. The orientation angles of the core cracks vary from 70° to 80° accordingly.

The failure mechanism of the sandwich beam is characterized by the appearance of matrix shear cracks in the face sheet and core crushing due to the high compressive stress near the impact point. Because the compressive core strength is significantly higher than the tensile and shear strengths, the sandwich core does not fail under the compressive stress. However, as the bending deformation increases, a tensile crack appears in the core near the bottom face sheet (due to the high bending moment) and propagates through the core thickness to the top face sheet. Similar to the static

loading results, the propagation of this crack plays a major role in the final collapse of the sandwich beam. Eventually, face/core debonding occurs partially at the bottom and the top of the sandwich core. Meanwhile, as explained in the previous section, the interface debonding process is a result of the formation of a large diagonal core crack.

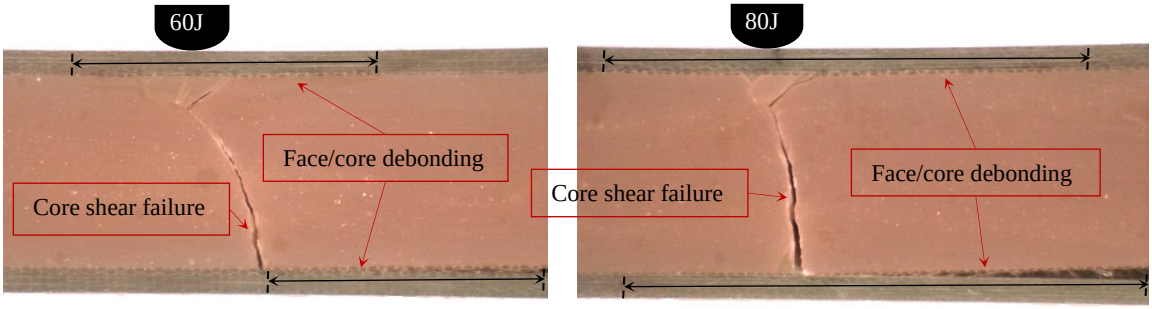

Figure 5.12: Crack propagation of the sandwich beams for impact energies of 60 J and 80 J

The variation of peak impact force as a function of the initial impact energy is plotted in Figure 5.13 for the sandwich beams studied in this work. The peak force increases linearly with the impact energy up to approximately 60 J before becoming almost constant for the higher impact energies. The transition point corresponds to the collapse of the sandwich beam during the impact loading. For the impact energies less than 60 J, the localized indentation is merely observed in the top face and core. Nevertheless, for impact energies of more than 60 J, core shear failure and face/core debonding are observed in the sandwich beams, in addition to the localized indentation.

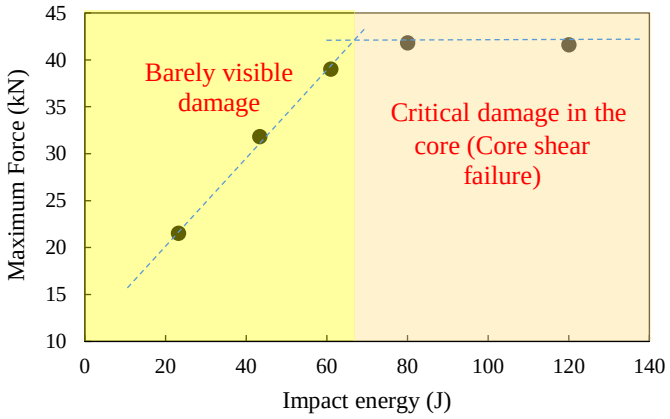

Figure 5.13: Maximum impact force versus the impact energy

Experimental force-displacement curves for impact energies of 60 J and 80 J are shown in Figure 5.14 together with the curve obtained from the quasi-static loading. The impactor displacement which includes the global deformation of sandwich beam and local indentation under the impact

point is used in this figure. The force-displacement curves show approximately linear behavior until failure of the sandwich beam. The two impact loading curves show similar behavior with slight differences in the maximum impact force and oscillation frequency. The low-frequency oscillation observed in the force-time curves is caused by the flexural wave propagation in the sandwich beam. However, according to Feraboli (2006) the first force fluctuation of the force-time curves corresponds to the inertial loading of the tup.

A comparison between the quasi-static and impact loading cases shows that the flexural stiffness associated with dynamic loading is comparatively higher than the static flexural stiffness of the sandwich beams. As the strain rate increases, the apparent impact loading flexural strength also tends to increase. The reason for this is that the sandwich core is an epoxy-based material, which is very sensitive to the strain rate. It has been revealed that increasing the strain rate results in an escalation of the stiffness and the strength of the resin epoxy (Goldberg, 1999). This finding also confirms the application of the viscoplastic-damage model in the simulated behavior of the ATH/epoxy core. The strain rate for the three-point flexural tests can be obtained via a method presented in Ref. (Land, 1979). The strain rate is calculated using the following equation:

$$\dot{\varepsilon} = \frac{6hv}{L^2} \tag{5-18}$$

where v is the velocity of the specimen, and h and L represent the thickness of the specimen and the specimen span, respectively. Therefore, the strain rate is approximately 19.5 s^{-1} for an impact energy of 60 J. It is worth noticing that even though the strain rate affects the stiffness and strength of sandwich beam, the amount of energy required to collapse the sandwich beam under static loading (58 J) is approximately the same as that of dynamic loading. This means that the fracture toughness of sandwich beam is nearly independent of strain rate.

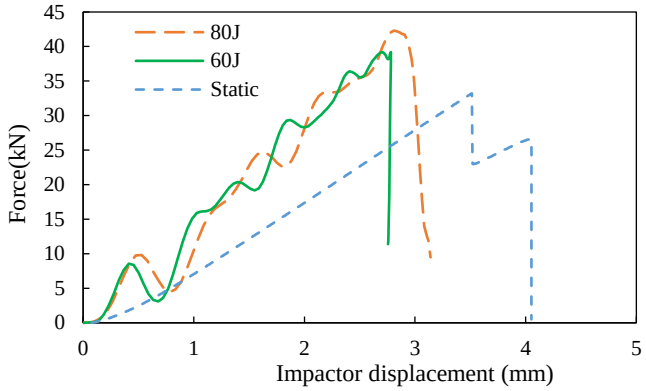

Figure 5.14: Force-deflection response for the sandwich beams under static and flexural impact loading

A comparison between the quasi-static and impact loading conditions in terms of the damage developing in the sandwich beam (matrix cracks in the top face sheet and core crushing) is illustrated in Figure 5.15. The damage zone under static loading is larger than the damage area induced by impact loading. Furthermore, two drop load steps are identified during static loading compare to impact loading. This indicates that impact failure appears to be more brittle than static failure.

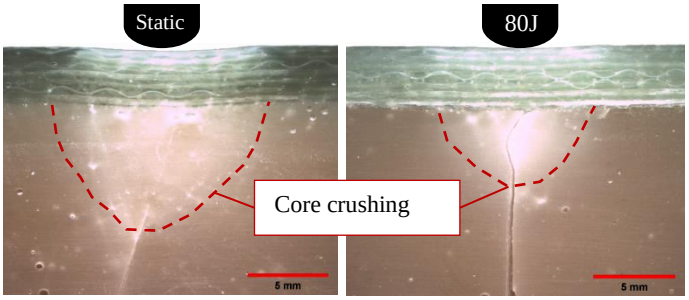

Figure 5.15: Comparison of static and impact induced damage (after longitudinal cross sectioning)

5.5.3.2 Numerical results

A comparison between the numerical and experimental results for the force-time, energy-time and force-displacement curves for impact energies of 20 J and 40 J is shown in Figure 5.16. The predicted force-time curves correlate well with the curves obtained experimentally. The energy absorbed during an impact event is reasonably predicted by the numerical model. As shown, a considerable amount of the initial impact energy (approximately 50%) is dissipated in the sandwich

beam. The numerical results show that the impact energy dissipates mainly via the irreversible plastic deformation and core crushing.

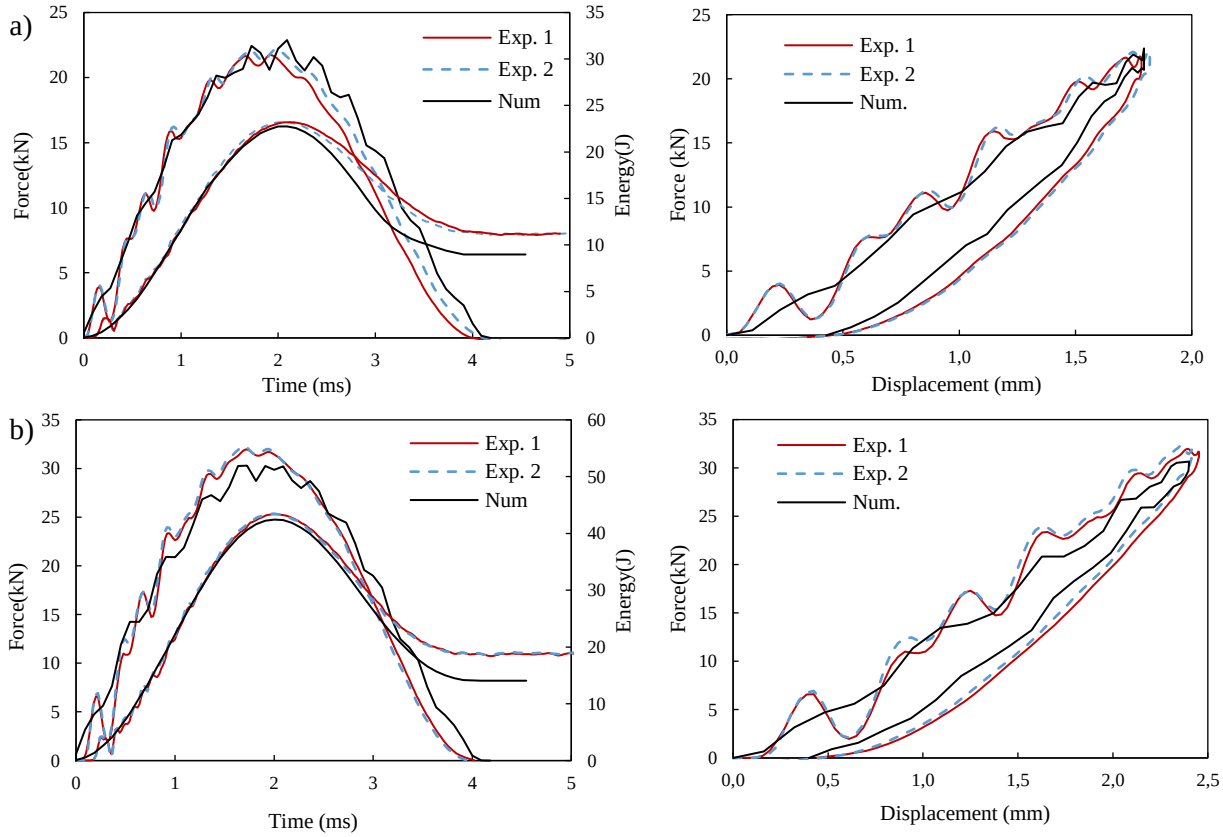

Figure 5.16: Comparison of experimental and numerical results for impact energies of: a) 20 J and b) 40 J

The force-time, energy-time and force-displacement curves are compared with the experimental data at impact energies of 60 J and 80 J in Figure 5.17. An excellent correlation is found between the predicted failure force and the energy obtained experimentally. For an impact energy of 80 J, the numerical results show that the absorbed energy is underestimated compared to the test data. The observed difference may be attributed to the formation of more significant interface debonding, which caused more energy dissipation in the experimental specimens. The force-displacement curves are also well predicted by the numerical model in the loading section; however, slight differences were observed in the unloading section.

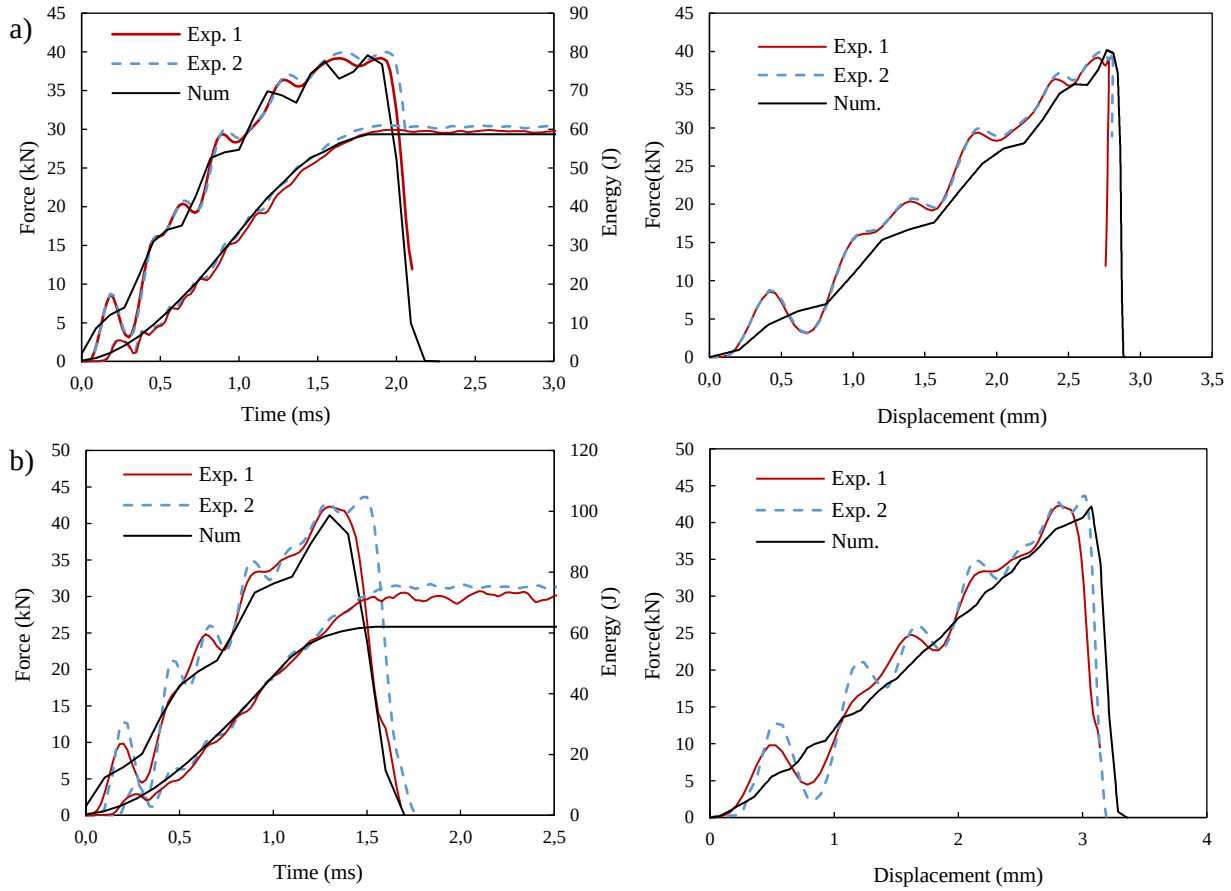

Figure 5.17: Comparison of experimental and numerical results for impact energies of: a) 60 J and b) 80 J

Additional details regarding the damage zone were obtained by longitudinal sectioning of the impacted specimen in the middle of the impact zone. The damage zones in the face sheet and in the core were evaluated and compared with the simulated results, as illustrated in Figure 5.18. The bright area in the top face sheet (Figure 5.18a) shows the damage zone induced by the impact of 80 J. The numerical results reveal that the damage zone is caused by the concentrated compressive and shear stresses. The angle of fracture plan $|\theta|$ in the damage zone varies between 30° and 70° indicating the occurrence of matrix shear cracks in the face sheet (Richardson et al., 1996b). The progressive damage model of the face sheet precisely predicted the size and the shape of the damaged area in the top face sheet. The small damage zone under the top face sheet (Figure 5.18b) represents crushing in the core region which propagates gradually as the contact force increases. Finally the crack formation in the core region due to high tensile and shear stresses is illustrated in Figure 5.18c. The viscoplastic-damage model of the ATH/epoxy also accurately captured the damage size and failure sequence in the core.

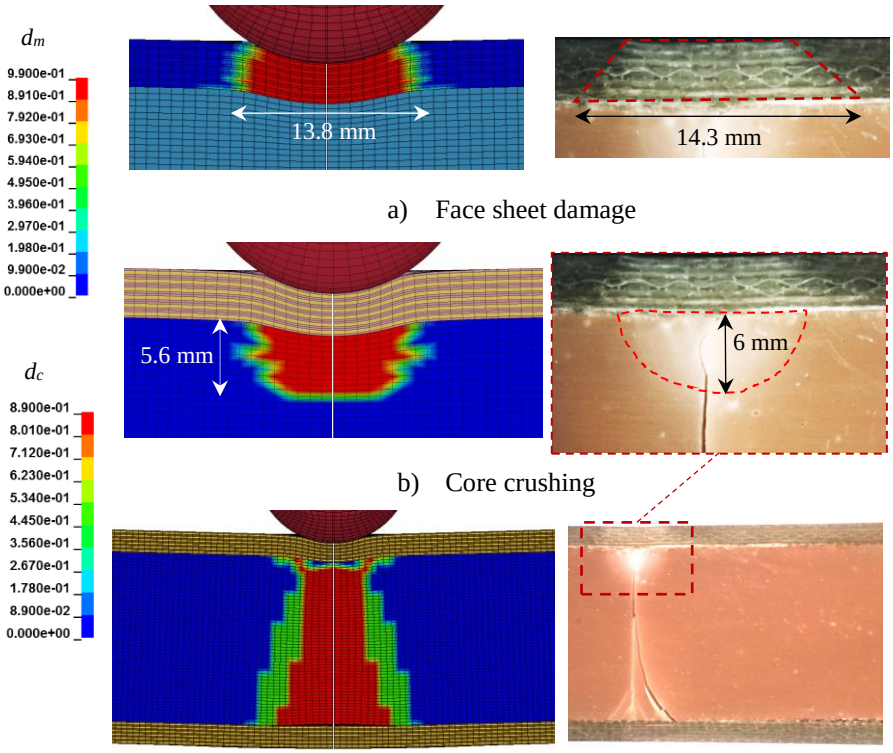

Figure 5.18: Comparison of the predicted damage and experimental damage zones

Numerical analysis of the deformation induced by impact loading is shown in Figure 5.19, which includes the global flexural deformation and local indentation under the impact point. The numerical results shows that the local indentation is the main component of deformation in sandwich beams. The localization of deformation could be attributed to the high Young's modulus of the core material. This feature results in enhancing the energy dissipation capacity of sandwich beams.

In the framework of structural optimization and improving the impact damage tolerance of the structure, the critical parameters are the shear and tensile strength properties of the core material. Using a more ductile material with greater shear and tensile failure strains can enhance the damage tolerance of the sandwich beam and alter the failure mechanism. Decreasing the amount of ATH fill in the epoxy resin and/or adding E-glass Chopped Stand Mat can increase the shear and tensile failure strains of the core (Petersen et al., 2015).

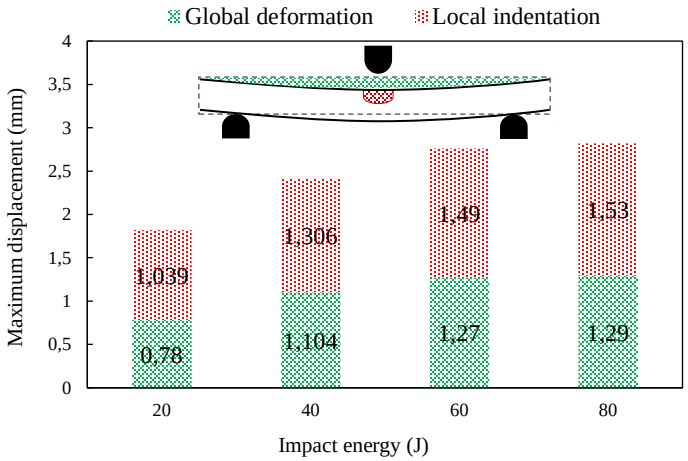

Figure 5.19: Global deformation and local indentation of the sandwich beams

5.5.4 Effect of impact-induced damage on the flexural response of beam

As demonstrated in the previous section, the sandwich specimens subjected to impact energies for 20 J and 40 J have only minor matrix damage in the top face sheet (Figure 5.20) and a small hemispherical crush zone in the core. To study the effects of impact-induced damage on the flexural response of the sandwich beams, quasi-static three-point bending tests were conducted on the impacted sandwich beams.

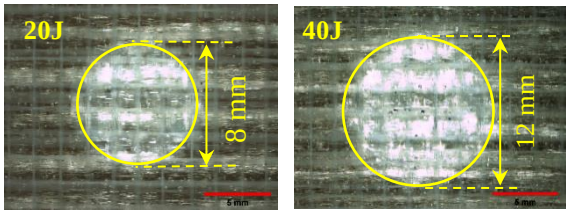

Figure 5.20: Visual damage zone in the impacted sandwich beams

The flexural behavior of the undamaged and damaged sandwich beams under quasi-static loading is compared in Figure 5.21. The undamaged and damaged sandwich beams exhibit the same flexural stiffness, and their flexural strengths are approximately the same. These findings indicate that the localized indentation damage due to high compressive stress has a negligible effect on the collapse of the sandwich beams (due to tensile and shear stresses). In fact, the localized damage in the top face sheet and core did not affect the capacity of the sandwich beam to withstand the flexural

stress. It can therefore be concluded that there is no interaction among the indentation failure and the core shear failure modes.

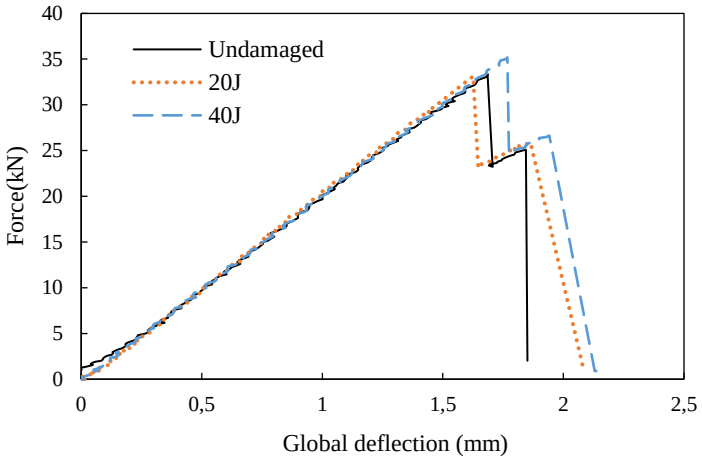

Figure 5.21: Load-deflection curves for the long beam sandwich subjected to quasi-static loading

5.6 Conclusions

The behavior of an NCF glass/epoxy laminated sandwich beam with an ATH/epoxy core was investigated under quasi-static and dynamic three-point bending. The flexural behavior of the sandwich beams was evaluated under low-velocity impact energies ranging from 20 J to 120 J. Additionally, a finite element model was implemented using the FEM software LS-DYNA/Explicit to predict damage initiation and propagation in the sandwich beams. The main conclusions are outlined as follows:

(1) The proposed model accurately reflects the experimental damage in the face sheet and the ATH/epoxy core during static and dynamic loading. Additionally, the sequence of damage propagation observed in the experiments is predicted with highly accurate results by the numerical model.

(2) Based on the results obtained from the short beam bending tests, the core/face debonding resistance is higher than the core shear resistance. As a result, the shear failure of the sandwich core occurred prior to debonding.

(3) The effect of strain rate on the flexural stiffness and strength of sandwich beam structures was demonstrated for a long sandwich beam. For a strain rate of 20 s^{-1}, the flexural stiffness can be up to 37% higher than the static flexural stiffness, and the dynamic flexural strength increases by 22% relative to the static flexural strength.

(4) The minimum energy needed to produce failure under static loading is nearly the same as the impact energy to fail the sandwich beam. Nevertheless, the static load-induced damage zone is larger than the impact load-induced damage area.

(5) It has been noted that matrix cracking in the top face sheet and core crushing occur early during the impact loading period due to localized indentation. For impact energies greater than 60 J, the failure mechanism is followed by core shear failure due to the global deformation of the sandwich beam, resulting in a sudden load drop and the loss of structural integrity.

(6) The effect of the localized indentation damage on the flexural response of the sandwich beams was also investigated. According to the experimental findings, the impact-induced damage has negligible effects on the flexural response of the beam. Thus, the interaction between the indentation mode and the core shear failure mode is insignificant.

The unique characteristics of this sandwich construction include localized impact damage, absorption of a large amount of impact energy, improving the face/core bonding and, consequently, increasing the damage tolerance of the sandwich structure. The sandwich structure with an ATH/epoxy core is therefore an excellent material choice for applications in which damage tolerance is a major concern. The sandwich construction can also be optimized by increasing the bending and shear resistance of the core material.

CHAPTER 6 GENERAL DISCUSSION

The aim of this thesis was to investigate the performance of sandwich panels with ATH/epoxy core in terms of mechanical behavior and impact resistance. The results of this investigation are presented in the three articles. This section provides a prolonged discussion on the different aspect presented in the thesis.

6.1 Modeling aspects

A finite element model based on the continuum damage mechanics approach was developed and validated in the numerical phase of this study. Initiation and propagation of damage modes occurring in the face sheets, such as matrix cracking and fiber failure, were simulated using 3D damage models. The nonlinear response of the ATH/epoxy core was simulated by a viscoplastic model. Interface delamination between plies and face sheet/core were modeled using cohesive elements. The functionality of face sheet and core models was separately assessed under dynamic loading. The model was then used to predict the impact response of composite sandwich structures as well as the damage propagation. The study showed the potential of numerical models to evaluate the damage progression under low-velocity impacts.

6.2 Damage resistance of sandwich structure

6.2.1 Effects of core material

The experimental and numerical investigations of low-velocity impact tests revealed that the core material properties significantly affect the mechanical behavior of sandwich structures. In order to clearly assess the effects of sandwich core material on the mechanical behavior and damage progression, the impact response of NCF glass/epoxy laminate and sandwich panel with ATH/epoxy core are compared in Figure 6.1. The results show that the maximum contact force and energy dissipation of sandwich panels are significantly higher than those of NCF laminates, and the contact duration and damage zone are relatively less. For an impact energy above 35 J, critical damage (fiber failure) has appeared in the impacted zone of NCF laminates. While the sandwich panels can withstand an impact energy of 60 J without critical damage in the face sheets. Both experimental and numerical results showed that the reduction in the size of damage zone and change in the failure mode is due to the capability of the sandwich core to absorb a large amount

of the initial impact energy. The sandwich core material dissipates approximately 50% of the initial impact energy.

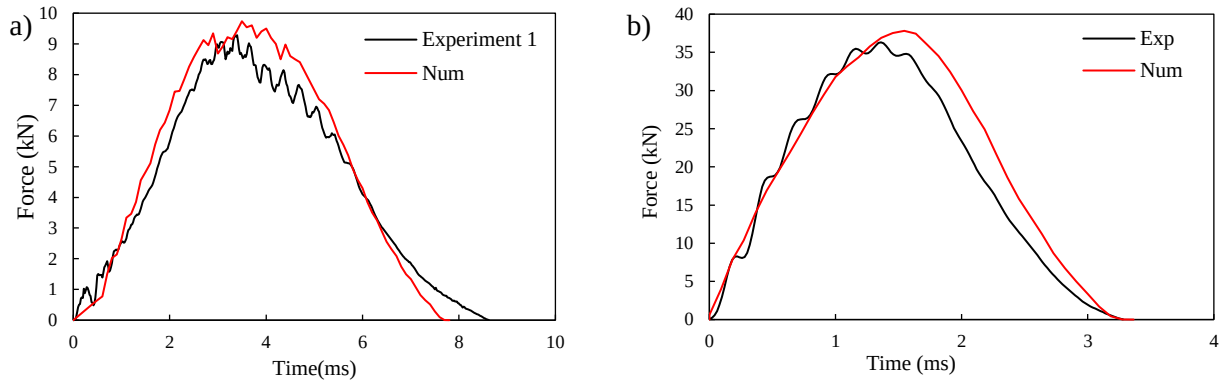

Figure 6.1: Impact response of: a) NCF laminate at impact energy of 45 J and b) sandwich panel at impact energy of 40 J

6.2.2 Effects of strain rate

The different performed tests showed that the mechanical behavior of glass/epoxy composite structures is greatly affected by varying strain rate. Strain rate dependent behavior was expected in the composite material during the preliminary phase of the study. For that reason, strain rate sensitivity was thus considered in the numerical models. In the experimental phase of the study, quasi-static and dynamic tests were performed on the sandwich panels with an ATH/epoxy core. The experimental and numerical results showed that the increase in strain rate was accompanied by increasing the flexural stiffness and strength of sandwich structures. Damage propagation in the sandwich structures was also affected by strain rate loading. The damaged zone considerably decreases with increasing strain rate loading.

6.2.3 Effects of global deformation

The three-point bending tests provided useful information on the effects of global deformation on the failure mechanism of sandwich structures. The impact response of sandwich panel clamped between two rigid supports with a hole of diameter 75 mm at the impact energy of 60 J is shown in Figure 6.2a. The mechanical response of sandwich beams under three-point impact loading is also shown in Figure 6.2b at the impact energy of 60 J. A comparison between the impact responses of two loading cases shows that the maximum contact forces have approximately the same value in both cases, while the failure modes are significantly different. In the first case, the indentation

failure which causes the shear cracks in the face sheet and the core crushing is the dominant failure mode. However, the core shear failure and face/core debonding appear under flexural impact loading in addition to the indentation failure. The numerical results demonstrate that the sandwich beam undergoes a large global deformation under flexural impact loading, which leads to the initiation of core shear failure. Decreasing the global deformation of the sandwich beam can restrict the failure modes to the indentation failure mode.

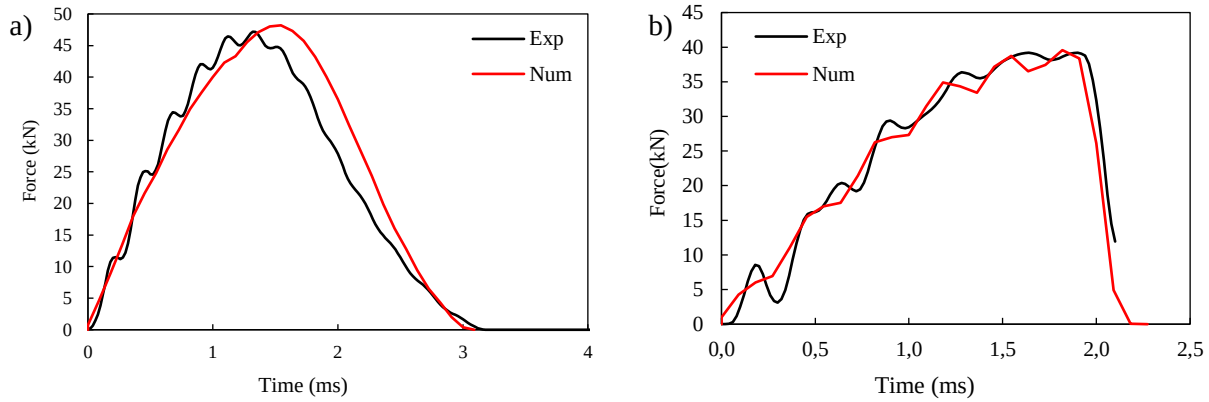

Figure 6.2: Impact response of: a) sandwich panel clamped between two rigid supports and b) sandwich beam under three-point bending at impact energy of 60 J

CHAPTER 7 CONCLUSION AND RECOMMENDATIONS

In this thesis, the mechanical response of sandwich panels with ATH/epoxy core subjected to low-velocity impact was investigated experimentally as well as numerically. Impact resistance of sandwich face sheet made with NCF glass/epoxy laminates was primarily studied.

The first step was to develop a numerical framework to predict damage growth in NCF glass/epoxy laminates subjected to low-velocity impact events. This framework takes into account the initiation and propagation of intra-laminar and inter-laminar damage. It also includes a nonlinear shear-strain behavior in combination with the strain rate effects and symmetric reversal loading. Tensile tests results of $[\{-45°/+45°/-45°\}]_{3s}$ specimens showed that the shear modulus and strength increase with strain rate. The numerical model reflected well the increase in shear properties due to strain rate. NCF glass/epoxy laminates were then analyzed under impact loadings, both experimentally and numerically, at various impact energies up to 73 J. The numerical results correlate well with the experimental data and microscopy observations. The experimental data showed that fiber breakage occurs at impact energies beyond 35 J, and the larger fiber bundle in NCF textile are more susceptible to rupture due to tensile stress. Furthermore, the experimental and numerical results revealed that the mechanical behavior of glass laminates at large displacement is affected by the strain rate under quasi-static loading, while it is insignificant under impact loading.

The second step was to investigate the impact resistance of sandwich panels with an ATH/epoxy core. To achieve this goal, a series of low-velocity impact tests on sandwich panels was performed following by destructive observations of impacted samples, to characterize damage progression with increasing the initial impact energy. In addition, a 3D progressive damage model was developed in order to predict damage growth in the face sheet and core of sandwich panels. The study revealed that critical damage such as interface delamination and fiber breakage was not occurred in the impacted face sheet for all investigated impact energies up to 60 J. No interface debonding was also observed in the impacted specimens, which demonstrates a good face/core interface bonding. The numerical results show that the sandwich core dissipated more than 50% of the initial impact energy through plastic deformation and matrix damage. Using the ATH/epoxy as sandwich core increases core crushing resistance and localizes deformation in the sandwich structure and consequently improves the damage resistance of the sandwich structure.

The final step consisted in the study of the failure mechanisms of sandwich beams with an ATH/epoxy core under quasi-static and dynamic three-point bending. The failure modes and interaction between them were evaluated by establishing different span distances in three-point bending tests. The short sandwich beams failed because of the shear failure of the core, while a combination of failure modes encompassing of flexural, core shear and face/core debonding were observed in the failure of long sandwich beams. The experimental results showed that the flexural stiffness and strength of sandwich beam increase as the strain rate increases. However, the average energy required to fail the sandwich beam under quasi-static loading was the same as that under impact loading. Furthermore, the viscoplastic model of ATH/epoxy captured the effect of strain rate on the flexural response of the sandwich beams accurately. The damage propagation in the sandwich core was also well predicted by the viscoplastic model. The experimental results showed that the core crushing is the major damage mode for an impact energy below 60 J, while the core shear failure leads to collapse of sandwich beams under an impact energy above 60 J. It was also found that interaction between the core crushing and the shear failure of the core is insignificant, while the core shear failure initiates the face/core interface debonding in the sandwich beams.

The study showed that the ATH/epoxy core enhances the impact resistance of the sandwich structure by localizing deformation and absorbing a large amount of impact energy through plastification. Construction of the sandwich structure made with NCF laminated composite face sheet and an ATH/epoxy core is therefore a promising choice for the extension of stay vanes.

Recommendations for future work

- **Investigation of adhesively-bonded joint between the composite extension and stay vane:** The research on the development of adhesively-bonded joint between the glass fiber reinforced composites and steel structures are still ongoing. Mechanical behavior and failure modes of adhesively bonded joints need to be investigated by using various adhesive materials and considering different surface pretreatment approaches on surfaces of laminated composite and steel supports. A finite element analysis or a closed form analytical model can be used to perform stress analysis on the adhesively-bonded joints. The bonded joints can go under the pure or mixed normal and shear loading which should be considered in the investigation.

- **Modeling environmental aging effects on impact response of sandwich panels:** The extension stay vane structure is exposed to sever environmental conditions. The effects of long-term water immersion aging on the impact response of sandwich structures need to be studied. In the relative literature, only a limited numerical models exist which can take into account the influence of moisture absorption on composite materials. The first step would be to perform accelerated aging tests. Matrix and fiber/matrix interface degradation must be evaluated experimentally. The second step would be to define the material constitutive law by considering the mechanical properties degradation due to moisture absorption.
- **Investigation of low velocity repeated impacts on the sandwich panels:** The composite structure of extension is subjected to low velocity repeated impacts induced by the flowing debris. Mechanical properties of sandwich structure may be considerably reduced due to damage accumulation. Energy absorption, maximum force and the permanent deformation of sandwich panels after multiple impact loads can be determined using a drop weight impact test machine. Performance of ATH/epoxy sandwich panels under repeated impact load can be evaluated in terms of mechanical properties and damage resistance.
- **Improvement of the mechanical properties of sandwich core**: This study established that the tensile and shear strengths of the core material are the weak point of sandwich structures. The mechanical performance of sandwich structure can be improved by increasing the shear and bending resistance of core material.

BIBLIOGRAPHY

Abdi, B., Azwan, S., Abdullah, M. R., Ayob, A., Yahya, Y., & Xin, L. (2014). Flatwise compression and flexural behavior of foam core and polymer pin-reinforced foam core composite sandwich panels. *International Journal of Mechanical Sciences, 88*, 138-144. doi: http://dx.doi.org/10.1016/j.ijmecsci.2014.08.004

Abrate, S. (1991). Impact on laminated composite materials. *Applied mechanics reviews, 44*(4), 155-190.

Abrate, S. (2005). *Impact on composite structures*: Cambridge university press.

Aktay, L., Johnson, A. F., & Holzapfel, M. (2005). Prediction of impact damage on sandwich composite panels. *Computational Materials Science, 32*(3), 252-260.

Alderliesten, R. (2009). Damage tolerance of bonded aircraft structures. *International Journal of Fatigue, 31*(6), 1024-1030.

Andersons, J., Tarasovs, S., & Spārniņš, E. (2010). Finite fracture mechanics analysis of crack onset at a stress concentration in a UD glass/epoxy composite in off-axis tension. *Composites Science and Technology, 70*(9), 1380-1385. doi: http://dx.doi.org/10.1016/j.compscitech.2010.04.017

ASTM. (2006). ASTM D3763–2006. Standard test method for high speed puncture properties of plastics using load and displacement sensor *USA Standards Association International, USA*.

ASTM. (2010). Standard Test Method for Compressive Properties of Rigid Plastics: ASTM International.

ASTM C393/C393M-16 Standard Test Method for Core Shear Properties of Sandwich Constructions by Beam Flexure, A. I., West Conshohocken, PA, 2016,.

ASTM D3039. (2003). *Standard test method for tensile properties of polymer matrix composite materials.* Paper presented at the American Society for Testing Materials.

Aymerich, F., Dore, F., & Priolo, P. (2008). Prediction of impact-induced delamination in cross-ply composite laminates using cohesive interface elements. *Composites Science and Technology, 68*(12), 2383-2390. doi: http://dx.doi.org/10.1016/j.compscitech.2007.06.015

Azzi, V., & Tsai, S. (1965). Anisotropic strength of composites. *Experimental mechanics, 5*(9), 283-288.

Bažant, Z. P., & Oh, B. H. (1983). Crack band theory for fracture of concrete. *Matériaux et construction, 16*(3), 155-177.

Benzeggagh, M. L., & Kenane, M. (1996). Measurement of mixed-mode delamination fracture toughness of unidirectional glass/epoxy composites with mixed-mode bending apparatus. *Composites Science and Technology, 56*(4), 439-449. doi: http://dx.doi.org/10.1016/0266-3538(96)00005-X

Berthelot, J.-M. (1999). Matériaux composites–Comportement mécanique et analyse des structures.

Besant, T., Davies, G. A. O., & Hitchings, D. (2001). Finite element modelling of low velocity impact of composite sandwich panels. *Composites Part A: Applied Science and Manufacturing, 32*(9), 1189-1196. doi: http://dx.doi.org/10.1016/S1359-835X(01)00084-7

Bodner, S. R. (2001). *Unified plasticity for engineering applications* (Vol. 47): Springer Science & Business Media.

Bornard, L., Debeissat, F., Labrecque, Y., Sabourin, M., & Tomas, L. (2014). *Turbine hydraulic assessment and optimization in rehabilitation projects.* Paper presented at the IOP Conference Series: Earth and Environmental Science.

Bouvet, C., Rivallant, S., & Barrau, J.-J. (2012). Low velocity impact modeling in composite laminates capturing permanent indentation. *Composites Science and Technology, 72*(16), 1977-1988.

Camanho, P. P., & Dávila, C. G. (2002). Mixed-mode decohesion finite elements for the simulation of delamination in composite materials.

Camanho, P. P., Dávila, C. G., Pinho, S. T., Iannucci, L., & Robinson, P. (2006). Prediction of in situ strengths and matrix cracking in composites under transverse tension and in-plane shear. *Composites Part A: Applied Science and Manufacturing, 37*(2), 165-176. doi: http://dx.doi.org/10.1016/j.compositesa.2005.04.023

Catalanotti, G., Camanho, P. P., & Marques, A. T. (2013). Three-dimensional failure criteria for fiber-reinforced laminates. *Composite Structures, 95*, 63-79. doi: http://dx.doi.org/10.1016/j.compstruct.2012.07.016

Chai, G. B., & Zhu, S. (2011a). A review of low-velocity impact on sandwich structures. *Proceedings of the Institution of Mechanical Engineers, Part L: Journal of Materials Design and Applications, 225*(4), 207-230.

Chai, G. B., & Zhu, S. (2011b). A review of low-velocity impact on sandwich structures. *Proceedings of the Institution of Mechanical Engineers, Part L: Journal of Materials: Design and Applications, 225*(4), 207-230. doi: 10.1177/1464420711409985

Chiu, L. N. S., Falzon, B. G., Boman, R., Chen, B., & Yan, W. (2015). Finite element modelling of composite structures under crushing load. *Composite Structures, 131*, 215-228. doi: http://dx.doi.org/10.1016/j.compstruct.2015.05.008

Compston, P., Jar, P. Y. B., & Davies, P. (1998). Matrix effect on the static and dynamic interlaminar fracture toughness of glass-fibre marine composites. *Composites Part B: Engineering, 29*(4), 505-516. doi: http://dx.doi.org/10.1016/S1359-8368(98)00004-3

Crupi, V., Epasto, G., & Guglielmino, E. (2012). Collapse modes in aluminium honeycomb sandwich panels under bending and impact loading. *International Journal of Impact Engineering, 43*, 6-15.

Crupi, V., Kara, E., Epasto, G., Guglielmino, E., & Aykul, H. (2015). Prediction model for the impact response of glass fibre reinforced aluminium foam sandwiches. *International Journal of Impact Engineering, 77*, 97-107. doi: http://dx.doi.org/10.1016/j.ijimpeng.2014.11.012

Daniel, I. M., Abot, J. L., Schubel, P. M., & Luo, J.-J. (2012). Response and Damage Tolerance of Composite Sandwich Structures under Low Velocity Impact. *Experimental mechanics, 52*(1), 37-47. doi: 10.1007/s11340-011-9479-y

Davies, G. A. O., Hitchings, D., Besant, T., Clarke, A., & Morgan, C. (2004). Compression after impact strength of composite sandwich panels. *Composite Structures, 63*(1), 1-9. doi: http://dx.doi.org/10.1016/S0263-8223(03)00119-3

Davies, G. A. O., & Olsson, R. (2004). Impact on composite structures. *The Aeronautical Journal, 108*(1089), 541-563. doi: 10.1017/S0001924000000385

Davies, G. A. O., & Zhang, X. (1995). Impact damage prediction in carbon composite structures. *International Journal of Impact Engineering, 16*(1), 149-170. doi: http://dx.doi.org/10.1016/0734-743X(94)00039-Y

Dey, V., Zani, G., Colombo, M., Di Prisco, M., & Mobasher, B. (2015). Flexural impact response of textile-reinforced aerated concrete sandwich panels. *Materials & Design, 86*, 187-197. doi: http://dx.doi.org/10.1016/j.matdes.2015.07.004

Donadon, M. V., De Almeida, S. F. M., Arbelo, M. A., & de Faria, A. R. (2009). A three-dimensional ply failure model for composite structures. *International Journal of Aerospace Engineering, 2009*.

Donadon, M. V., Iannucci, L., Falzon, B. G., Hodgkinson, J. M., & de Almeida, S. F. M. (2008). A progressive failure model for composite laminates subjected to low velocity impact damage. *Computers & Structures, 86*(11-12), 1232-1252. doi: 10.1016/j.compstruc.2007.11.004

Drapier, S., & Wisnom, M. R. (1999). Finite-element investigation of the compressive strength of non-crimp-fabric-based composites. *Composites Science and Technology, 59*(8), 1287-1297.

Edgren, F., & Asp, L. E. (2005). Approximate analytical constitutive model for non-crimp fabric composites. *Composites Part A: Applied Science and Manufacturing, 36*(2), 173-181.

Edgren, F., Asp, L. E., & Joffe, R. (2006). Failure of NCF composites subjected to combined compression and shear loading. *Composites Science and Technology, 66*(15), 2865-2877.

Edgren, F., Soutis, C., & Asp, L. E. (2008). Damage tolerance analysis of NCF composite sandwich panels. *Composites Science and Technology, 68*(13), 2635-2645. doi: http://dx.doi.org/10.1016/j.compscitech.2008.04.041

Egan, B., McCarthy, M. A., Frizzell, R. M., Gray, P. J., & McCarthy, C. T. (2014). Modelling bearing failure in countersunk composite joints under quasi-static loading using 3D explicit finite element analysis. *Composite Structures, 108*, 963-977. doi: http://dx.doi.org/10.1016/j.compstruct.2013.10.033

Evans, A. G., He, M., Deshpande, V. S., Hutchinson, J. W., Jacobsen, A. J., & Carter, W. B. (2010). Concepts for enhanced energy absorption using hollow micro-lattices. *International Journal of Impact Engineering, 37*(9), 947-959.

Faggiani, A., & Falzon, B. G. (2010). Predicting low-velocity impact damage on a stiffened composite panel. *Composites Part A: Applied Science and Manufacturing, 41*(6), 737-749. doi: 10.1016/j.compositesa.2010.02.005

Falzon, B. G., & Apruzzese, P. (2011). Numerical analysis of intralaminar failure mechanisms in composite structures. Part I: FE implementation. *Composite Structures, 93*(2), 1039-1046. doi: 10.1016/j.compstruct.2010.06.028

Feng, D., & Aymerich, F. (2013). Damage prediction in composite sandwich panels subjected to low-velocity impact. *Composites Part A: Applied Science and Manufacturing, 52*, 12-22.

Feng, D., & Aymerich, F. (2014). Finite element modelling of damage induced by low-velocity impact on composite laminates. *Composite Structures, 108*(0), 161-171. doi: http://dx.doi.org/10.1016/j.compstruct.2013.09.004

Feraboli, P. (2006). Some recommendations for characterization of composite panels by means of drop tower impact testing. *Journal of aircraft, 43*(6), 1710-1718.

Foo, C. C., Chai, G. B., & Seah, L. K. (2008). A model to predict low-velocity impact response and damage in sandwich composites. *Composites Science and Technology, 68*(6), 1348-1356. doi: http://dx.doi.org/10.1016/j.compscitech.2007.12.007

Goldberg, R. K. (1999). Strain Rate Dependent Deformation and Strength Modeling of a Polymer Matrix Composite Utilizing a Micromechanics Approach. Degree awarded by Cincinnati Univ.

Goldberg, R. K., Roberts, G. D., & Gilat, A. (2005). Implementation of an Associative Flow Rule Including Hydrostatic Stress Effects into the High Strain Rate Deformation Analysis of Polymer Matrix Composites. *Journal of Aerospace Engineering, 18*(1), 18-27. doi: doi:10.1061/(ASCE)0893-1321(2005)18:1(18)

Goswami, S., & Becker, W. (2001). The effect of facesheet/core delamination in sandwich structures under transverse loading. *Composite Structures, 54*(4), 515-521. doi: http://dx.doi.org/10.1016/S0263-8223(01)00124-6

Greve, L., & Pickett, A. K. (2006). Modelling damage and failure in carbon/epoxy non-crimp fabric composites including effects of fabric pre-shear. *Composites Part A: Applied Science and Manufacturing, 37*(11), 1983-2001.

Guédra-Degeorges, D. (2006). Recent advances to assess mono- and multi-delaminations behaviour of aerospace composites. *Composites Science and Technology, 66*(6), 796-806. doi: http://dx.doi.org/10.1016/j.compscitech.2004.12.041

Hashin, Z. (1980). Failure criteria for unidirectional fiber composites. *Journal of applied mechanics, 47*(2), 329-334.

Hassan, M., & Cantwell, W. (2012). The influence of core properties on the perforation resistance of sandwich structures–An experimental study. *Composites Part B: Engineering, 43*(8), 3231-3238.

Hodgkinson, J. M. (2000). *Mechanical testing of advanced fibre composites*: Elsevier.

Hoo Fatt, M. S., & Park, K. S. (2000). Perforation of honeycomb sandwich plates by projectiles. *Composites Part A: Applied Science and Manufacturing, 31*(8), 889-899. doi: http://dx.doi.org/10.1016/S1359-835X(00)00021-X

Hsiao, H., Daniel, I., & Cordes, R. (1999). Strain rate effects on the transverse compressive and shear behavior of unidirectional composites. *Journal of Composite Materials, 33*(17), 1620-1642.

Iannucci, L., & Ankersen, J. (2006). An energy based damage model for thin laminated composites. *Composites Science and Technology, 66*(7-8), 934-951. doi: 10.1016/j.compscitech.2005.07.033

Iannucci, L., Dechaene, R., Willows, M., & Degrieck, J. (2001). A failure model for the analysis of thin woven glass composite structures under impact loadings. *Computers & Structures, 79*(8), 785-799. doi: http://dx.doi.org/10.1016/S0045-7949(00)00190-5

Icardi, U., & Ferrero, L. (2009). Impact analysis of sandwich composites based on a refined plate element with strain energy updating. *Composite Structures, 89*(1), 35-51. doi: http://dx.doi.org/10.1016/j.compstruct.2008.06.018

Imielińska, K., Guillaumat, L., Wojtyra, R., & Castaings, M. (2008). Effects of manufacturing and face/core bonding on impact damage in glass/polyester–PVC foam core sandwich panels. *Composites Part B: Engineering, 39*(6), 1034-1041. doi: http://dx.doi.org/10.1016/j.compositesb.2007.11.007

Ivañez, I., Moure, M. M., Garcia-Castillo, S. K., & Sanchez-Saez, S. (2015). The oblique impact response of composite sandwich plates. *Composite Structures, 133*, 1127-1136. doi: http://dx.doi.org/10.1016/j.compstruct.2015.08.035

Ivañez, I., Santiuste, C., & Sanchez-Saez, S. (2010). FEM analysis of dynamic flexural behaviour of composite sandwich beams with foam core. *Composite Structures, 92*(9), 2285-2291. doi: http://dx.doi.org/10.1016/j.compstruct.2009.07.018

Ji, G., Ouyang, Z., & Li, G. (2013). Debonding and impact tolerant sandwich panel with hybrid foam core. *Composite Structures, 103*, 143-150. doi: http://dx.doi.org/10.1016/j.compstruct.2013.04.006

Jin, F., Chen, H., Zhao, L., Fan, H., Cai, C., & Kuang, N. (2013). Failure mechanisms of sandwich composites with orthotropic integrated woven corrugated cores: experiments. *Composite Structures, 98*, 53-58.

Joffe, R., Mattsson, D., Modniks, J., & Varna, J. (2005). Compressive failure analysis of non-crimp fabric composites with large out-of-plane misalignment of fiber bundles. *Composites Part A: Applied Science and Manufacturing, 36*(8), 1030-1046.

Joki, R., Grytten, F., & Hayman, B. (2015). Nonlinear response in glass fibre non-crimp fabric reinforced vinylester composites. *Composites Part B: Engineering, 77*, 105-111.

Kachanov, L. M. (1958). Rupture time under creep conditions. *International Journal of Fracture, 97*(1-4), 11-18.

Klaus, M., Reimerdes, H. G., & Gupta, N. K. (2012). Experimental and numerical investigations of residual strength after impact of sandwich panels. *International Journal of Impact Engineering, 44*, 50-58. doi: http://dx.doi.org/10.1016/j.ijimpeng.2012.01.001

Land, P. L. (1979). Strain rates for three-and four-point flexure tests. *Journal of Materials Science, 14*(11), 2760-2761.

Liu, D. (1988). Impact-induced delamination—a view of bending stiffness mismatching. *Journal of Composite Materials*, *22*(7), 674-692.

Lopes, C. S., Sádaba, S., González, C., Llorca, J., & Camanho, P. P. (2016). Physically-sound simulation of low-velocity impact on fiber reinforced laminates. *International Journal of Impact Engineering*, *92*, 3-17. doi: https://doi.org/10.1016/j.ijimpeng.2015.05.014

Maio, L., Monaco, E., Ricci, F., & Lecce, L. (2013). Simulation of low velocity impact on composite laminates with progressive failure analysis. *Composite Structures, 103*, 75-85. doi: https://doi.org/10.1016/j.compstruct.2013.02.027

Majumdar, P., Srinivasagupta, D., Mahfuz, H., Joseph, B., Thomas, M. M., & Christensen, S. (2003). Effect of processing conditions and material properties on the debond fracture toughness of foam-core sandwich composites: experimental optimization. *Composites Part A: Applied Science and Manufacturing*, *34*(11), 1097-1104. doi: http://dx.doi.org/10.1016/S1359-835X(03)00207-0

Mallick, P. K. (2007). *Fiber-reinforced composites: materials, manufacturing, and design*: CRC press.

Mines, R., Worrall, C., & Gibson, A. (1998a). Low velocity perforation behaviour of polymer composite sandwich panels. *International Journal of Impact Engineering*, *21*(10), 855-879.

Mines, R. A. W., Worrall, C. M., & Gibson, A. G. (1998b). LOW VELOCITY PERFORATION BEHAVIOUR OF POLYMER COMPOSITE SANDWICH PANELS. *International Journal of Impact Engineering*, *21*(10), 855-879. doi: http://dx.doi.org/10.1016/S0734-743X(98)00037-2

Othman, A. R., & Barton, D. C. (2008). Failure initiation and propagation characteristics of honeycomb sandwich composites. *Composite Structures*, *85*(2), 126-138. doi: http://dx.doi.org/10.1016/j.compstruct.2007.10.034

Ouadday, R. (2013). ÉTUDE DES STRUCTURES SANDWICHS VERRE/ÉPOXY DE GRANDES ÉPAISSEURS UTILISÉES COMME EXTENSION D'AVANT DIRECTRICES DE TURBINES HYDROÉLECTRIQUES. *Département de Génie Mécanique, École Polytechnique de Montréal*.

Papadakis, N., Reynolds, N., Pharaoh, M. W., Wood, P. K. C., & Smith, G. F. (2004). Strain rate effects on the shear mechanical properties of a highly oriented thermoplastic composite material using a contacting displacement measurement methodology–Part A: elasticity and shear strength. *Composites Science and Technology, 64*(5), 729-738. doi: http://dx.doi.org/10.1016/j.compscitech.2003.08.001

Petersen, M. R., Chen, A., Roll, M., Jung, S. J., & Yossef, M. (2015). Mechanical properties of fire-retardant glass fiber-reinforced polymer materials with alumina tri-hydrate filler. *Composites Part B: Engineering, 78*, 109-121. doi: http://dx.doi.org/10.1016/j.compositesb.2015.03.071

Phipps, M., Pritchard, G., & Abou-Torabi, A. (1995). The role of particle strength and filler volume fraction in the fracture of alumina trihydrate filled epoxy resins. *Polymers & polymer composites, 3*(2), 71-77.

Pinho, S., Darvizeh, R., Robinson, P., Schuecker, C., & Camanho, P. (2012). Material and structural response of polymer-matrix fibre-reinforced composites. *Journal of Composite Materials, 46*(19-20), 2313-2341.

Pinho, S. T., Iannucci, L., & Robinson, P. (2006). Physically-based failure models and criteria for laminated fibre-reinforced composites with emphasis on fibre kinking: Part I: Development. *Composites Part A: Applied Science and Manufacturing, 37*(1), 63-73. doi: 10.1016/j.compositesa.2005.04.016

Puck, A., & Schürmann, H. (1998). FAILURE ANALYSIS OF FRP LAMINATES BY MEANS OF PHYSICALLY BASED PHENOMENOLOGICAL MODELS. *Composites Science and Technology, 58*(7), 1045-1067. doi: http://dx.doi.org/10.1016/S0266-3538(96)00140-6

Richardson, M., & Wisheart, M. (1996a). Review of low-velocity impact properties of composite materials. *Composites Part A: Applied Science and Manufacturing, 27*(12), 1123-1131.

Richardson, M. O. W., & Wisheart, M. J. (1996b). Review of low-velocity impact properties of composite materials. *Composites Part A: Applied Science and Manufacturing, 27*(12), 1123-1131. doi: http://dx.doi.org/10.1016/1359-835X(96)00074-7

Roy, R., Sarkar, B. K., & Bose, N. R. (2001). Impact fatigue of glass fibre–vinylester resin composites. *Composites Part A: Applied Science and Manufacturing, 32*(6), 871-876. doi: http://dx.doi.org/10.1016/S1359-835X(00)00151-2

Sankar, B. V., & Kwon, Y. S. (1993). Indentation-flexure and low-velocity impact damage in graphite epoxy laminates. *Journal of Composites, Technology and Research, 15*(2), 101-111.

Satyanarayana, A., Bogert, P. B., Aitharaju, V., Aashat, S., & Kia, H. (2014). Damage Simulation in Non-Crimp Fabric Composite Plates Subjected to Impact Loads. *29th American Society for Composites Technical Conference in La Jolla, USA, September 8*

Schubel, P. M., Luo, J.-J., & Daniel, I. M. (2005). Low velocity impact behavior of composite sandwich panels. *Composites Part A: Applied Science and Manufacturing, 36*(10), 1389-1396. doi: http://dx.doi.org/10.1016/j.compositesa.2004.11.014

Singh, H., & Mahajan, P. (2015). Modeling damage induced plasticity for low velocity impact simulation of three dimensional fiber reinforced composite. *Composite Structures, 131*, 290-303. doi: http://dx.doi.org/10.1016/j.compstruct.2015.04.070

Soutis, C., & Curtis, P. T. (1996). Prediction of the post-impact compressive strength of cfrp laminated composites. *Composites Science and Technology, 56*(6), 677-684. doi: http://dx.doi.org/10.1016/0266-3538(96)00050-4

Standard, A. (2005). D7136/D7136M–05, Standard test method for measuring the damage resistance of a fiberreinforced polymer matrix composite to a drop-weight impact event. *West Conshohocken (PA): ASTM International*.

Standard, A. (2011). D3171, Standard Test Methods for Constituent Content of Composite Materials: West Conshohocken.

Steeves, C. A., & Fleck, N. A. (2004). Collapse mechanisms of sandwich beams with composite faces and a foam core, loaded in three-point bending. Part II: experimental investigation and numerical modelling. *International Journal of Mechanical Sciences, 46*(4), 585-608. doi: http://dx.doi.org/10.1016/j.ijmecsci.2004.04.004

Styles, M., Compston, P., & Kalyanasundaram, S. (2007). The effect of core thickness on the flexural behaviour of aluminium foam sandwich structures. *Composite Structures, 80*(4), 532-538. doi: http://dx.doi.org/10.1016/j.compstruct.2006.07.002

Talreja, R. (1985). *A continuum mechanics characterization of damage in composite materials.* Paper presented at the Proceedings of the Royal Society of London A: Mathematical, Physical and Engineering Sciences.

Tan, K. T., Watanabe, N., Iwahori, Y., & Ishikawa, T. (2012). Understanding effectiveness of stitching in suppression of impact damage: An empirical delamination reduction trend for stitched composites. *Composites Part A: Applied Science and Manufacturing, 43*(6), 823-832. doi: http://dx.doi.org/10.1016/j.compositesa.2011.12.022

Thorsson, S. I., Xie, J., Marek, J., & Waas, A. M. (2016). Matrix crack interacting with a delamination in an impacted sandwich composite beam. *Engineering Fracture Mechanics, 163*, 476-486.

Topac, O. T., Gozluklu, B., Gurses, E., & Coker, D. (2016). Experimental and computational study of the damage process in CFRP composite beams under low-velocity impact. *Composites Part A: Applied Science and Manufacturing*. doi: http://dx.doi.org/10.1016/j.compositesa.2016.06.023

Torre, L., & Kenny, J. (2000a). Impact testing and simulation of composite sandwich structures for civil transportation. *Composite structures, 50*(3), 257-267.

Torre, L., & Kenny, J. M. (2000b). Impact testing and simulation of composite sandwich structures for civil transportation. *Composite Structures, 50*(3), 257-267. doi: http://dx.doi.org/10.1016/S0263-8223(00)00101-X

Truong, T. C., Vettori, M., Lomov, S., & Verpoest, I. (2005). Carbon composites based on multi-axial multi-ply stitched preforms. Part 4. Mechanical properties of composites and damage observation. *Composites Part A: Applied Science and Manufacturing, 36*(9), 1207-1221.

Tsai, G.-C., & Chen, J.-W. (2005). Effect of stitching on Mode I strain energy release rate. *Composite Structures, 69*(1), 1-9. doi: http://dx.doi.org/10.1016/j.compstruct.2004.02.009

Tsai, S. W., & Wu, E. M. (1971). A General Theory of Strength for Anisotropic Materials. *Journal of Composite Materials, 5*(1), 58-80. doi: 10.1177/002199837100500106

Turon, A., Davila, C. G., Camanho, P. P., & Costa, J. (2007). An engineering solution for mesh size effects in the simulation of delamination using cohesive zone models. *Engineering Fracture Mechanics, 74*(10), 1665-1682.

Vaidya, A. S., Vaidya, U. K., & Uddin, N. (2008). Impact response of three-dimensional multifunctional sandwich composite. *Materials Science and Engineering: A, 472*(1–2), 52-58. doi: http://dx.doi.org/10.1016/j.msea.2007.03.064

Vallons, K., Behaeghe, A., Lomov, S. V., & Verpoest, I. (2010). Impact and post-impact properties of a carbon fibre non-crimp fabric and a twill weave composite. *Composites Part A: Applied Science and Manufacturing, 41*(8), 1019-1026. doi: http://dx.doi.org/10.1016/j.compositesa.2010.04.008

Veedu, V. P., & Carlsson, L. A. (2005). Finite-element buckling analysis of sandwich columns containing a face/core debond. *Composite Structures, 69*(2), 143-148. doi: http://dx.doi.org/10.1016/j.compstruct.2004.06.005

W. J. Cantwell, C. D. a. P. D. (1994). Comparative study of the mechanical properties of sandwich materials

for nautical construction. . *SAMPE J., 30*(4), 45—51.

Wang, H., Ramakrishnan, K. R., & Shankar, K. (2016). Experimental study of the medium velocity impact response of sandwich panels with different cores. *Materials & Design, 99*, 68-82. doi: http://dx.doi.org/10.1016/j.matdes.2016.03.048

Wang, Y., Zhang, L., & Cheng, L. (2009). Effects of carbon yarn size on the mechanical properties of plain woven C/SiC composites. *International Journal of Applied Ceramic Technology, 6*(4).

Wei, X., de Vaucorbeil, A., Tran, P., & Espinosa, H. D. (2013). A new rate-dependent unidirectional composite model – Application to panels subjected to underwater blast. *Journal of the Mechanics and Physics of Solids, 61*(6), 1305-1318. doi: http://dx.doi.org/10.1016/j.jmps.2013.02.006

Williams, K. V., & Vaziri, R. (2001). Application of a damage mechanics model for predicting the impact response of composite materials. *Computers & Structures, 79*(10), 997-1011. doi: http://dx.doi.org/10.1016/S0045-7949(00)00200-5

Yan, L. L., Han, B., Yu, B., Chen, C. Q., Zhang, Q. C., & Lu, T. J. (2014). Three-point bending of sandwich beams with aluminum foam-filled corrugated cores. *Materials & Design, 60*, 510-519. doi: http://dx.doi.org/10.1016/j.matdes.2014.04.014

Yu, J., Wang, E., Li, J., & Zheng, Z. (2008). Static and low-velocity impact behavior of sandwich beams with closed-cell aluminum-foam core in three-point bending. *International Journal of Impact Engineering, 35*(8), 885-894. doi: http://dx.doi.org/10.1016/j.ijimpeng.2008.01.006

Zhou, J., Guan, Z. W., & Cantwell, W. J. (2013). The impact response of graded foam sandwich structures. *Composite Structures, 97*, 370-377. doi: http://dx.doi.org/10.1016/j.compstruct.2012.10.037

Zhou, J., Hassan, M. Z., Guan, Z., & Cantwell, W. J. (2012). The low velocity impact response of foam-based sandwich panels. *Composites Science and Technology, 72*(14), 1781-1790. doi: http://dx.doi.org/10.1016/j.compscitech.2012.07.006

Zhou, Y., Nezhad, H. Y., Hou, C., Wan, X., McCarthy, C., & McCarthy, M. (2015). A three dimensional implicit finite element damage model and its application to single-lap multi-bolt composite joints with variable clearance. *Composite Structures, 131*, 1060-1072.